

**STIMULI-RESPONSIVE CONJUGATED POLYMER NANOPARTICLES AS SIMPLE
THERANOSTIC PLATFORMS**

A THESIS

SUBMITTED TO THE DEPARTMENT OF MATERIALS SCIENCE AND
NANOTECHNOLOGY

AND THE GRADUATE SCHOOL OF ENGINEERING AND SCIENCE

OF BILKENT UNIVERSITY

IN PARTIAL FULFILLMENT OF THE REQUIREMENTS

FOR THE DEGREE OF

MASTER OF SCIENCE

By

ALP ÖZGÜN

July, 2014

I certify that I have read this thesis and that in my opinion it is fully adequate, in scope and in quality, as a thesis for the degree of Master of Science.

.....
Assoc. Prof. Dr. Dönüş TUNCEL (Advisor)

I certify that I have read this thesis and that in my opinion it is fully adequate, in scope and in quality, as a thesis for the degree of Master of Science.

.....
Assoc. Prof. Dr. Mustafa Özgür Güler

I certify that I have read this thesis and that in my opinion it is fully adequate, in scope and in quality, as a thesis for the degree of Master of Science.

.....
Assist Prof. Dr. Emrah Özensoy

Approved for the Graduate School of Engineering and Science:

.....

Prof. Dr. Levent ONURAL

Director of the Graduate School

ABSTRACT

STIMULI-RESPONSIVE CONJUGATED POLYMER NANOPARTICLES AS SIMPLE THERANOSTIC PLATFORMS

Alp Özgün

M.Sc. in Materials Science and Nanotechnology

Supervisor: Assoc. Prof. Dr. Dönüş TUNCEL

July, 2013

In this study, green and near-infrared emitting stimuli responsive conjugated polymer nanoparticles that can be utilized simultaneously for chemotherapeutic drug delivery and bioimaging were synthesized. The nanoparticles are sensitive to low pH values of tumor microenvironment or elevated redox potential of some tumor types. These theranostic platforms could be used for in-vivo imaging and perform controlled-drug release triggered by an appropriate stimulus.

For this purpose, green emitting polymer with fluorene and benzothiadiazole alternating units in the backbone and a conjugated polymer emitting in the red-NIR region based on thiophene and benzothiadiazole alternating units in the backbone were synthesized and characterized. Nanoparticles of these polymers (CPNs) were prepared by a simple method called nanoprecipitation where hydrophobic polymer chains collapse onto each other in aqueous media, trapping any other hydrophobic drug molecules (anticancer agent camptothecin in our case) in the environment inside the polymer matrix. Nanoprecipitation process was optimized for each polymer to obtain maximum drug encapsulation rate and a narrow nanoparticle size distribution under 100 nm. Resulting CPNs were stable for a long time in PBS buffer, water, bovine serum albumin and human plasma. SEM images showed spherical particles with a narrow diameter distribution. In vitro drug release studies, pH responsive CPNs showed faster drug release in more acidic media. Redox sensitive red polymer on the other hand showed a cleavage of disulfide bond in its structure in the presence of stimulus.

To evaluate the cytotoxicity of drug loaded and blank CPNs RT-CES (real-time cell electronic sensing) assays with HuH-7 cell line have been carried out. While blank CPNs show an insignificant temporary cytotoxicity, camptothecin loaded nanoparticles match or outperform the growth inhibition effect of free camptothecin. Fluorescence microscopy images of HuH-7 cells incubated with CPNs clearly show CPNs that are internalized by cells.

In conclusion, it was demonstrated that conjugated polymers could be used to fabricate theranostic platforms without the need for an additional imaging agent and their structures can be engineered to obtain stimuli responsive smart drug delivery systems. These results promise simple and easily fabricated smart systems that can selectively carry anticancer agents to tumors while enabling monitoring of drug distribution and inexpensive tumor imaging without using any harmful rays on the highly energetic side of the electromagnetic spectrum.

Keywords: Conjugated polymer nanoparticles, cross-linking, pH sensitive, redox sensitive, theranostics.

ÖZET

BASİT TERANOSTİK PLATFORMLAR OLARAK UYARANLARA HASSAS KONJUGE POLİMER NANOPARÇACIKLAR

Alp Özgün

Malzeme Bilimi ve Nanoteknoloji Yüksek Lisans Tezi

Tez Yöneticisi : Doç. Dr. Dönüş TUNCEL

Temmuz, 2014

Bu çalışmada yeşil ve yakın-kızılötesi bölgede ışıyan, uyarılara hassas, aynı anda hem biyolojik görüntüleme hem de kemoterapi ilaçlarının taşınması için kullanılabilir konjuge polimer nanoparçacıklar sentezlenmiştir. Nanoparçacıklar tümör bölgelerinin düşük pH değerlerine ya da bazı tümör tiplerindeki yüksek indirgeme potansiyeline hassastır. Bu teranostik platformlar in-vivo görüntüleme için kullanılırken aynı zamanda uyarılarla tetiklenen kontrollü ilaç salınımı gerçekleştirebilirler.

Ana zincirinde değişimli fluoren ve benzothiadiazole birimleri taşıyan ve yeşil bölgede ışıyan bir polimer sentezlenmiştir. Ana zincirinde değişimli tiyofen ve benzothiadiazole birimleri taşıyan bir başka polimer sentezlenmiş ve kırmızı ile yakın-kızılötesi bölgede ışığı görülmüştür. Bu polimerlerin nanoparçacıkları nanoçöktürme denilen ve hidrofobik polimer zincirlerinin sulu ortamda büzüşüp ortamda bulunan diğer hidrofobik ajanları da hapsederek nanoparçacıklar oluşturmaya dayanan bir yöntemle hazırlanmıştır. Nanoçöktürme işleminin parametreleri, maksimum ilaç miktarını hapsedecek ve 100 nm altında iyi bir çap dağılımına sahip nanoparçacıklar elde edecek şekilde optimize edilmiştir. Elde edilen konjuge polimer nanoparçacıklar suda ve diğer protein ortamlarında uzun bir süre kararlı bir şekilde kalabildiler. Elektron mikroskobu görüntülerinde küresel ve boyutları birbirine yakın nanoparçacıklar gözlemlenmiştir. In-vitro ilaç salınım deneylerinde, asidik pH değerlerine hassas nanoparçacıklar asidik ortamda daha hızlı ilaç salınımını sağladılar. İndirgeme potansiyeline hassas nanoparçacıklar da bünyelerinde bulunan disülfid çapraz bağların uyarı varlığında kırıldığını gösterdi.

İlaç ile yüklenmiş ve boş nanoparçacıkların hücreler üzerindeki toksik etkisini gözlemlemek amacı ile Huh7 hücre hattı ile RT-CES (gerçek zamanlı elektronik hücre algılama) denemeleri yapılmıştır. Boş nanoparçacıklar önemsiz ve geçici bir toksik etki gösterirken, kamptotesin ile yüklenmiş nanoparçacıklar serbest kamptotesinin gösterdiği büyümeyi durdurma etkisini

gösterdiler. Nanoparçacıklar ile beraber inkübe edilmiş Huh7 hücrelerinin floresan mikroskop görüntüleri açıkça nanoparçacıkların hücreler tarafından alındığını gösteriyor.

Sonuç olarak konjuge polimerlerin fazladan bir görüntüleme ajanına gerek kalmadan teranostik platformların üretiminde kullanılabilmesi ve yapılarının uyarılara hassas akıllı sistemler elde edilecek şekilde tasarlanabileceği gösterilmiştir. Bu sonuçlar basit ve kolayca üretilen, antikanser ajanlarını seçici olarak tümörlere taşıırken aynı zamanda ilaç dağılımını izlemeye ve yüksek enerjili zararlı ışınlar kullanmadan tümör görüntülemesi yapmaya olanak sağlayabilecek akıllı sistemler vaat ediyor.

Keywords: Konjuge polimer nanoparçacıklar, çapraz bağlama, pH hassasiyeti, indirgenme hassasiyeti, teranostik.

ACKNOWLEDGEMENT

I would like to thank Assoc. Prof. Dr. Dönüş Tuncel for her guidance, supervision and patience during my research.

I am thankful to Assoc. Prof. Dr. Mustafa Özgür Güler and Assist. Prof. Dr. Emrah Özensoy for reading my thesis and their invaluable feedbacks.

We acknowledge TÜBİTAK 112T704.

I would like to express my sincere appreciation to my lab mates Jousheed Pennakalathil, Özlem Ünal, Rehan Khan, Sinem Gürbüz, Muazzam İdris, Esra Deniz Soner and Hamidou Keita for their friendship and support.

I can't overstate my appreciation to my family for their moral support, patience, respect and love.

I am dedicating my thesis to my mother who devoted her life to raising her sons as honest people.

ABBREVIATIONS

FT-IR	Fourier Transform-Infrared
¹H-NMR	Proton-Nuclear Magnetic Resonance
UV-Vis	Ultraviolet- visible spectroscopy
PL	Fluorescence spectroscopy
DLS	Dynamic Light Scattering
SEM	Scanning Electron Microscopy
CDCl₃	Deuterated chloroform
DMSO	Dimethyl sulfoxide
CPNs	Conjugated Polymer Nanoparticles
HOMO	Highest Occupied Molecular Orbital
LUMO	Lowest Unoccupied Molecular Orbital
CPT	Camptothecin
THF	Tetrahydrofuran
PBT-(Ac)	Poly [2-(2,5-dibromo-thiophen-3-yl)-ethyl acetate)- <i>co</i> -4,7-(2,1,3-Benzothiadiazole)]
PBF	poly {3-[9-(3-tert-Butoxycarbonylamino-propyl)-3-methyl-6-(7-methyl-4,7-dihydro-benzo[1,2,5]thiadiazol-4-yl)-9H-fluoren-9-yl]-propyl}-carbamic acid tert-butyl ester
PBT-LA	(R)-2-(2-(benzo[c][1,2,5]thiadiazol-4-yl)thiophen-3-yl)ethyl 5-(1,2-dithiolan-3-yl)pentanoate

TABLE OF CONTENTS

ABSTRACT	4
ÖZET	6
ABBREVIATIONS	8
LIST OF FIGURES	11
LIST OF SCHEMES	14
CHAPTER 1. INTRODUCTION	15
1.1. Theranostics.....	15
1.1.1. Drug Delivery Systems.....	15
1.1.2. Biomedical Imaging Agents.....	17
1.1.3. Smart Theranostic Platforms.....	19
1.2. Stimuli-Responsive Systems for Drug Delivery.....	20
1.3. Conjugated Polymers.....	24
1.4. Nanoparticle Preparation from Conjugated Polymers.....	26
1.5. Applications of Conjugated Polymer Nanoparticles.....	29
1.6. Aim of Thesis.....	31
CHAPTER 2. RESULTS AND DISCUSSION	33
2.1. Introduction.....	33
2.2. Synthesis and Characterization of pH Responsive Conjugated Polymer Nanoparticles.....	33
2.2.1. Synthesis and Characterization of Red Emitting pH Sensitive Conjugated Polymer Nanoparticles.....	33
2.2.1.1. PBT-(Ac) Synthesis and Characterization.....	34
2.2.1.2. Nanoparticle Preparation, Characterization and In Vitro Tests.....	40
2.2.2. Synthesis and Characterization of Green Emitting pH Sensitive Conjugated Polymer Nanoparticles.....	48
2.2.2.1. PBF Synthesis and Characterization.....	48
2.2.2.2. Nanoparticle Preparation, Characterization and In Vitro Tests.....	52

2.3. Synthesis and Characterization of Red Emitting Redox Sensitive Conjugated Polymer Nanoparticles.....	61
2.3.1. PBT-LA Synthesis and Characterization.....	62
2.3.2. Nanoparticle Preparation, Characterization and In Vitro Tests..	67
CHAPTER 3. CONCLUSION	78
CHATER 4. EXPERIMENTAL DETAILS	80
4.1 Synthesis of 2-(2,5-dibromothiophen-3-yl)ethanol (M1).....	80
4.2 Synthesis of 2-(2,5-dibromothiophen-3-yl)ethyl acetate (M2).....	80
4.3 Syntnthesis of Poly [2-(2,5-dibromo-thiophen-3-yl)-ethyl acetate)- <i>co</i> -4,7-(2,1,3-Benzothiadiazole)] (PBT-(Ac)).....	81
4.4 Synthesis of poly{3-[9-(3-tert-Butoxycarbonylamino-propyl)-3-methyl-6-(7-methyl-4,7-dihydro-benzo[1,2,5]thiadiazol-4-yl)-9H-fluoren-9-yl]-propyl}-carbamic acid tert-butyl ester (PBF).....	82
4.5 Synthesis of (R)-2-(2-(benzo[c][1,2,5]thiadiazol-4-yl)thiophen-3-yl)ethyl 5-(1,2-dithiolan-3-yl)pentanoate (PBT-LA).....	82
4.6 Preparation of Nanoparticles.....	83
4.7 Drug Release Studies.....	83
REFERENCES	85

LIST OF FIGURES

Figure 4: Chemical structures of some amine functionalized acid sensitive polymers.....	22
Figure 5: Structure of glutathione	22
Figure 6: Synthetic steps and illustration of redox sensitive PEG coated camptothecin carriers.	23
Figure 7: Structure of alpha-lipoic acid.....	24
Figure 8: Structure of the first synthesized conjugated polymer polyacetylene.....	24
Figure 9: Band gap representations of insulators, semi-conductors and conductors.	25
Figure 10: Jablonski diagram showing fluorescence and phosphorescence events.....	26
Figure 11: Schematic representation of nanoprecipitation method.....	27
Figure 12: Biomedical applications of CPNs.....	29
Figure 13: Schematic representation of pH sensitive tracking of CPNs by using FRET between doxorubicin and conjugated polymer BTTPF.....	30
Figure 14: Schematic illustration of a stimuli-sensitive theranostic platform designed in this work.	31
Figure 15: ¹ H-NMR (400 MHz, 25 °C, CDCl ₃) spectrum of M1.....	35
Figure 16: ¹ H-NMR (400 MHz, 25 °C, CDCl ₃) spectrum of M2.....	36
Figure 17: ¹ H-NMR (400 MHz, 25 °C, CDCl ₃) spectrum of PBT-(Ac).	37
Figure 18: FTIR (KBr pellet) spectrum of PBT-(Ac).	37
Figure 19: DSC graph of PBT-(Ac).	38
Figure 20: TGA graph of PBT-(Ac).....	39
Figure 21: UV-Vis absorbance and PL emission spectra of PBT-(Ac) solution in THF.	39
Figure 22: SEM Micrographs of Blank and CPT Loaded PBT-(Ac) Nanoparticles.....	40
Figure 23: Stability of PBT-(Ac) nanoparticles in water over time.	41
Figure 24: Uv-Vis absorbance and PL emission of PBT-(Ac) solutions and aqueous nanoparticles.	41
Figure 25: DLS and zeta-potential measurements of CPNs at different pH values.	42
Figure 26: Drug loading and entrapment efficiency values determined for different drug:polymer ratios.	43
Figure 27: Time- dependent release profile of PBT-(Ac).	44
Figure 28: RT-CES results of blank and CPT loaded CPNs with different drug loading rates.....	45
Figure 29: Fluorescent microscopy images of Huh7 cells incubated with blank and CPT loaded PBT-(Ac) nanoparticles	47
Figure 30: ¹ H-NMR (400 MHz, 25 °C, CDCl ₃) spectrum of PBF.	49
Figure 31: TGA graph of PBF.	50
Figure 32: DSC graph of PBF.....	51
Figure 33: FTIR spectra of PBF before and after acid treatment.....	51
Figure 34: UV-Vis absorption and PL emission spectra of PBF in different solvents.	52
Figure 35: UV-Vis absorption and PL emission spectra of PBF in solution and as aqueous CPNs.....	53
Figure 36: Different Z-average sizes obtained with different PBF concentrations.....	54

Figure 37: SEM micrographs of PBF nanoparticles.....	54
Figure 38: Stability of PBF nanoparticles in water over time.	55
Figure 39: Zeta potentials and sizes of PBF nanoparticles at different pH values.	56
Figure 40: Drug loading and entrapment efficiency values of PBF nanoparticles for different drug:polymer ratios.	57
Figure 41: Release profile of PBF nanoparticles at two different pH values.	58
Figure 42: RT-Ces results of CPT loaded and blank PBF nanoparticles.	59
Figure 43: Fluorescence microscopy images of Huh7 cells incubated with blank and CPT loaded PBF nanoparticles.	61
Figure 44: FTIR Spectra of PBT-(Ac) and PBT-OH.	63
Figure 45: ¹ H-NMR (400 MHz, 25 °C, CDCl ₃) spectra of PBT-LA (top) and Lipoic Acid (bottom).	64
Figure 46: ¹ H-NMR (400 MHz, 25 °C, CDCl ₃) spectrum of PBT-LA.....	65
Figure 47: FTIR spectra of PBT-LA and PBT-OH.....	66
Figure 48: Structure of Pluronic f-127.	67
Figure 49: DLS measurement of PBT-LA nanoparticles formed by dissolving surfactant in THF.....	67
Figure 50: DLS measurement of PBT-LA nanoparticles formed by dissolving surfactant in water.	68
Figure 51: Initial and cross-linked sizes of PBT-LA nanoparticles prepared with different polymer concentrations.....	69
Figure 52: SEM micrographs of aqueous (a) bare and (b) poloxamer coated PBT-LA nanoparticles. Cross-linked nanoparticles dispersed in THF (c).	70
Figure 53: Bare, poloxamer coated and cross-linked PBT-LA dispersions with added chloroform layers.	70
Figure 54: FTIR spectra of poloxamer, bare CPNs and poloxamer coated CPNs.....	71
Figure 55: PBT-LA nanoparticle size differences after being kept 1 month in different media.....	72
Figure 56: UV-Vis absorbance and PL emission spectra of bare and poloxamer coated PBT-LA nanoparticles.	72
Figure 57: Drug loading and entrapment efficiency values of PBT-LA nanoparticles for different drug:polymer ratios.	74
Figure 58: CPT release profile of PBT-LA nanoparticles in the absence and presence of GSH.	75
Figure 59: Fluorescence microscopy images of Huh7 cells incubated with blank and CPT loaded PBT-LA nanoparticles.....	76
Figure 60: RT-Ces results of CPT loaded and blank PBF nanoparticles.	77

LIST OF SCHEMES

Scheme 1: Reaction scheme for PBT-(Ac).....	34
Scheme 2: Synthetic scheme for PBF.....	48
Scheme 3: Synthetic scheme for PBT-LA.....	62

CHAPTER 1

INTRODUCTION

1.1 Theranostics

Theranostics is a portmanteau word formed by combining the words “therapy” and “diagnostics”. (1) The term was coined after rapid development of nanomedicine and refers to systems that combine therapeutic and diagnostic elements on a single platform especially in the context of cancer. Diagnostics usually refers to different biomedical imaging techniques in this context like MRI, PET, ultrasound and fluorescence. (2) Theranostic systems include imaging or image enhancement agents for these imaging modes. Therapy usually refers to release of therapeutic drug molecules (drug delivery) or elimination of diseased cells by hyperthermia or production of reactive radical species. Nanomedicine systems that combine these elements together are classified as theranostic platforms. These systems can be advantageous not only for clinical tumor management where therapy and imaging is done simultaneously but also for drug development since biodistribution of drugs are directly monitored in these systems. (3)

1.1.1 Drug Delivery Systems

Drug delivery systems involve loading of small drug molecules into nano or micro-sized drug carriers and then using them instead of free drug. This concept has a lot of benefits compared to free drugs. In drug delivery systems, drug molecules are trapped inside carriers and are unable to show any activity inside the body until they're released. Restricting distribution of drugs inside the body greatly reduces any side effects caused by drug's unwanted interactions with non-targeted tissues. This is especially a major issue in chemotherapy of tumors where drugs are designed to exterminate all the cells with high proliferation rates and end up devastating almost all endothelial linings of the body. (4)

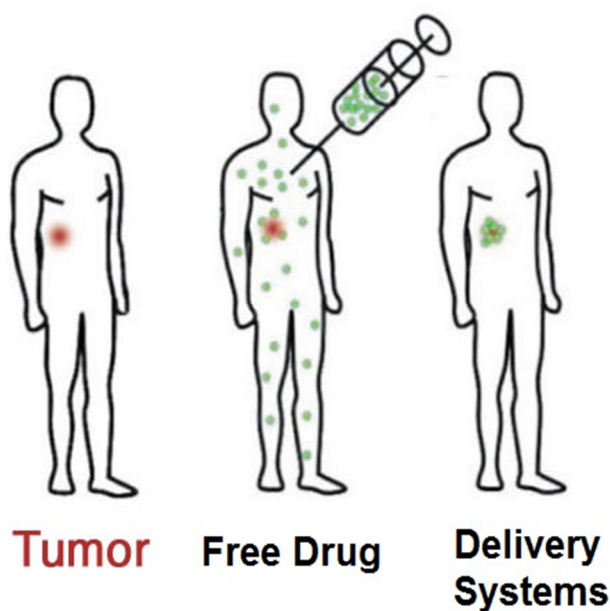


Figure 1: Biodistribution of free drugs and delivery systems.

Using drugs loaded into carriers causes them to stay in the blood circulation for a much longer time until they are released from the carrier with a mechanism or they diffuse out themselves. In the case of chemotherapy of solid tumors, this concept leads to targeting of drug molecules directly to tumors without any complicated designs due to leaky blood vessels of tumors. Over-expression of angiogenesis factors by tumor cells leads to deformed leaky blood vessels within tumors and drug carriers cannot get out of the bloodstream except from these deformities. This leads to accumulation of drug molecules inside the tumors as seen in Figure 1 and is called enhanced permeability and retention (EPR) effect. (5)

Many organic and inorganic based drug carriers are put forward like gold nanoparticles, mesoporous silica nanoparticles, peptides, liposomes and polymer nanoparticles. (6) Polymer nanoparticles stand out among these systems with their exceptional chemical and physical versatility. Polymer structures can be designed to have desirable chemical properties such as biocompatibility, bioinertness, biodegradability and they can easily be converted into nanoparticles with a number of different methods to obtain polymer nanoparticles with tunable sizes. Their structures can be designed to have suitable groups for attachment of different functionalities such as targeting moieties and cell penetrating agents. (7)

Generally, a drug/small molecule can be loaded into a polymer nano-carrier either by being encapsulated in a core with a similar hydrophobicity or by being conjugated through covalent bonds. For instance, hydrophobic drug doxorubicin can be conveniently encapsulated into the hydrophobic domain of a micelle fabricated from amphiphilic copolymers (8) or conjugated to water-soluble polymers via various bonds. Correspondingly, the loaded doxorubicin can be released from the carrier by diffusion, the erosion of the carrier, or both, or via the breakage of the linker. (9) (10)

1.1.2 Biomedical Imaging Agents

Biomedical imaging techniques almost exclusively depend on passing of electromagnetic radiation through body and detection of this radiation as a signal to be processed and converted into two dimensional signals which are basically images. These techniques can be basically classified based on the electromagnetic radiation that is used. On the highest energetic and shortest wavelength (<10 pm) side of the spectrum there are techniques like positron emission tomography (PET) and gamma camera which are based on detection of emissions from nuclear decay of radioactive elements such as technetium and indium injected into body. X-rays that originate from inner-shell electrons of metal atoms have longer wavelengths (0.01 nm-10 nm) and relatively lower energy. This type of electromagnetic radiation has different rates of penetration in different types of tissues which are exploited to differentiate between hard and soft tissues on x-ray films and computed tomography (CT) scans. Magnetic resonance imaging (MRI) on the other hand operates all the way on the other side of the spectrum where wavelengths are measured in meters. MRI uses these waves to measure relaxation time of water molecules under strong magnetic field and uses the difference between relaxation times to differentiate between different soft tissue types.

Producing, detecting and processing these wavelengths at two extremes of the spectrum require bulky, expensive equipment and highly optimized environments. Using light around visible region instead would be much less expensive to produce and detect besides causing none of the side effects produced by high energy radiation in the case of X-rays and nuclear medicine.

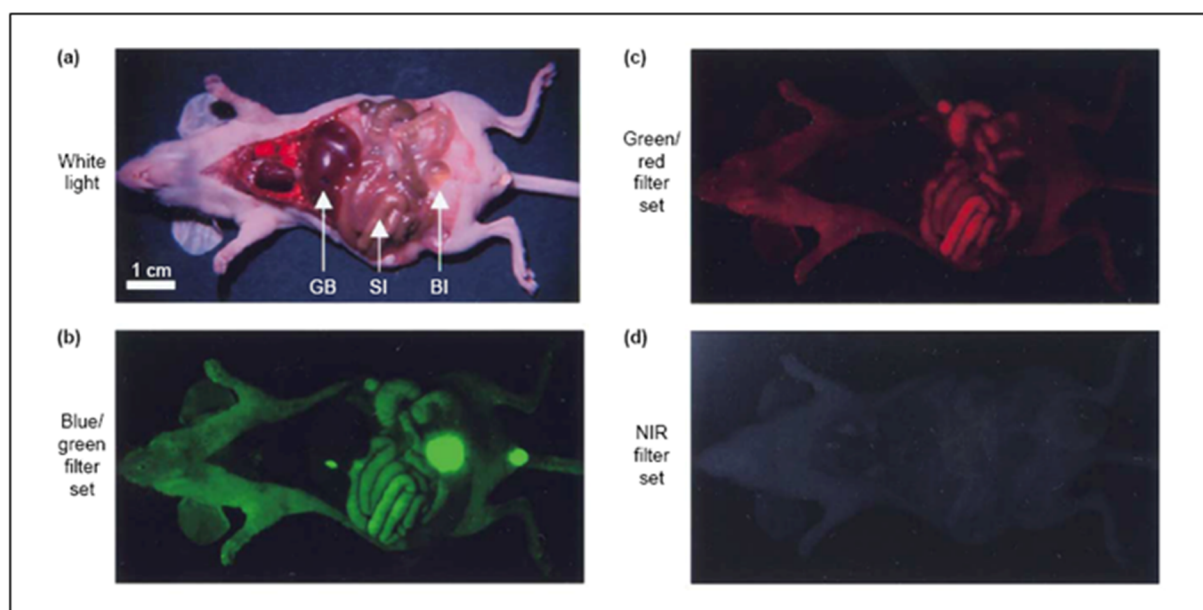


Figure 2: Wavelength dependent auto-fluorescence of different mouse tissues. Gall bladder (GB), small intestine (SI) and bladder (BI) are indicated with arrows. **Reproduced with permission from (11). Copyright 2003, Elsevier.**

The reason near-visible wavelengths are not used routinely in medicine is that biological subjects produce plenty of background radiation at these wavelengths besides absorbing and scattering photons which makes it challenging to obtain high contrast quality images. However, upon close inspection, it can be seen that native tissue absorbance and auto-fluorescence drops drastically in the near-infrared region -between 650 nm and 1100 nm- leaving behind oxy-hemoglobin and deoxy-hemoglobin as two major absorbers and a significantly low background auto-fluorescence as seen in Figure 2. (11) This potentially useful wavelength range is named “the imaging window” and constitutes the first and most important rule of fluorescence bio-imaging agents. Excitation light needs to be in the imaging window for minimal tissue absorbance and deep penetration. Fluorescence generated by the imaging agent also needs to fall in this window for high signal/noise ratio, high contrast and minimal scattering and absorbance of produced photons. (12) Furthermore, these probes need to be water soluble or dispersible to work in biological media. Water aggregation of hydrophobic agents and fluorescence quenching due to this aggregation is one of the major problems with fluorescence imaging agents. High quantum yield is another one of the desirable properties since it provides

high signal/noise ratio. Having some sort of targeting mechanism is a vital aspect of using fluorescence imaging in terms of creating contrast between tissues. (13) Attachment of targeting ligands to fluorescence probes or utilizing other passive targeting mechanisms are major goals of studies on different classes of near-infrared imaging probes.

1.1.3 Smart Theranostic Systems

While EPR effect is the most fundamental advantage of chemotherapeutic drug delivery systems, many more benefits start to emerge as these systems become much more complex than just a drug carrier as seen in Figure 3. Targeting proteins can be attached to carrier surfaces to target specific receptors of tumor cells. This is called active tumor targeting and usually involves a specific receptor-ligand interaction between targeted cells and carriers such as antibody-antigen interactions. Passive targeting strategies mentioned above can be incorporated into the carrier to mediate drug release in presence of tumor-specific stimuli. (14)

Stealthy carriers can be designed by coating them with biocompatible polymers. These polymers are usually non-charged water soluble polymers. Hydrophilicity of these coatings causes a layer of water to form around nano-carriers and prevent any recognition by leukocytes which greatly reduces the immune response against drug carriers. These coatings increase circulation time of carriers inside the blood stream by reducing opsonization. (15)

Cell penetrating agents can be used to enhance internalization of carriers inside the cells. Nano-carriers are usually known to be internalized by endocytosis and proteins on actively targeted carriers tend to act as cell penetrating agents as they are a key component in receptor-mediated endocytosis. Other than that, cell penetrating peptide sequences can also be used to enhance internalization rate of carriers. (16)

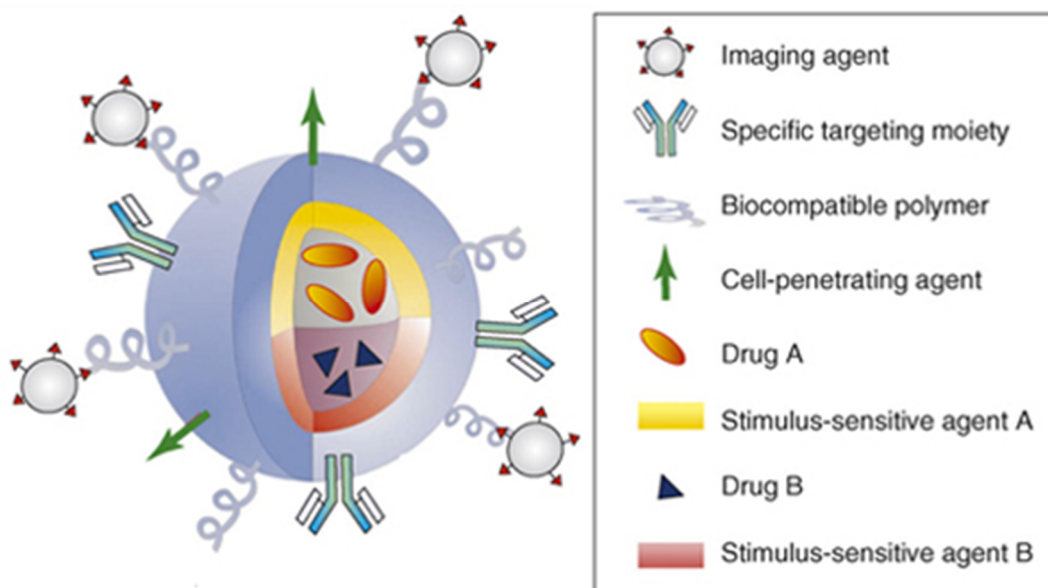


Figure 3: Schematic representation of a multifunctional drug carrier. Reproduced with permission from (14). Copyright 2008, Elsevier.

Many other different functional properties can be added to these carriers to obtain smart multifunctional systems. For example attachment of an imaging agent makes it a theranostic system but with every added different function, these systems become more and more complicated. Each added moiety changes the in-vivo behavior of carriers and too many different moieties make their working mechanisms more convoluted and unpredictable. Moreover, with each added synthetic step, cost of designing, preparing and optimizing these systems increases. (17)

1.2 Stimuli-Responsive Systems for Passive Targeting

Passive targeting methods are strategies that accumulate drugs around tumor sites without using any targeting moieties on the drug carrier. These methods usually exploit abnormal physiological and chemical properties of tumor tissues. EPR effect is the main method of passive targeting of many types of tumors. In this method, leaky vasculature of tumor tissues caused by overexpression of growth factors such as VEGF and lack of lymphatic drainage is used. Nano-sized carriers are not filtered through glomeruli of kidneys as long as they are larger than 10 nm which causes them to stay intact in the bloodstream for extended periods of time. (5) If their size distribution is carefully adjusted, these nanoparticles can leave the bloodstream through endothelial cell gaps of tumor vasculature which have a size of around 100–600 nm. Moreover, the lack of lymphatic drainage prevents them from being discharged from the extracellular fluid and leads to a large build-up of drug carriers inside tumor tissues. (18) (19)

Targeting efficacy can be further enhanced by using other certain abnormalities of tumor microenvironments. Rapidly proliferating nature of cancer cells depletes the environment from nutrients and oxygen rather quickly. This causes glucose to be broken down incompletely in the Krebs cycle to produce lactic acid. Lactic acid accumulation results in a more acidic environment compared to healthy tissues. Tumor pH values can drop down to 6,75 while healthy tissues have a mean pH value of 7,23. (20) Moreover, elevated metabolic rates of cancer cells produce more heat than healthy cells and this heat cannot be dissipated properly due to retention of liquids resulting in local hyperthermia of tumors. These cues can be used to target drug carriers to tumors without using active targeting moieties. (21) (22) (23) (24) (25)

For example acid labile hydrazone bonds are used frequently in designs that release drugs at acidic environments. For example anticancer agent doxorubicin was attached to the hydrophobic side of an amphiphilic polymer via a hydrazone bond. Resulting micelles facilitated selective accumulation of doxorubicin inside solid tumors due to cleavage of hydrazone bond at low pH and release of free doxorubicin inside the tumor. (24) (22) In addition these pH-sensitive bonds can be used in the backbone of polymers which will cause polymeric carriers to disintegrate in acidic tumor environment exposing the payload selectively. (26) (27) Another popular way of designing pH sensitive carriers is using pH sensitive ionizable polymers. For example poly acids such as poly (acrylic acid), poly (methyl acrylic acid), poly (ethyl acrylic acid) and poly (sulfonic acid) are ionized in alkaline solutions and the repulsion between charged groups changes the physical behavior of the polymers. The pH value at which the pendant acids start to ionize is determined by pKa value of the polymer which depends on polymer's composition and molecular weight. (28) Acid sensitive polymers on the other hand typically carry basic functional groups that become ionized at low pH values such as primary, secondary and tertiary amine groups. (29) (30) The most popular examples of these polymers are poly [2-(dimethylamino)ethylmethacrylate] (PDMAEMA) and poly(vinylamine) (PVAm) whose structures can be seen in Figure 4. These strategies can be used to design polymers with finely tuned pKa values to target tissues with specific pH values in the body especially acidic tumor environments. (31)

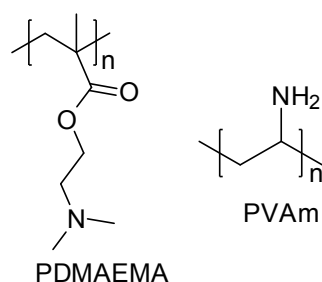


Figure 4: Chemical structures of some amine functionalized acid sensitive polymers.

While most active targeting strategies utilize over-expressed membrane receptors or other proteins in cancer cells, passive targeting can also utilize over-abundance of some molecules inside cancer cells. Glutathione (GSH) is the most abundant non-protein thiol in eukaryotic cells which consists of three amino acids whose structure is displayed in Figure 5. Thiol groups act as reducing agents to reduce disulfide bonds formed between cysteines of cytoplasmic proteins. After thiol-disulfide exchange reactions with these disulfides, GSH is converted to its oxidized form glutathione disulfide where two GSH molecules are combined by a disulfide bond (32). GSH is known to be involved in cell protection against free radicals and reduction of some internalized molecules. Deregulation of GSH synthesis is observed in many different types of human cancers. Elevated levels of GSH in tumor cells are associated with multidrug and radiation resistance of tumors and GSH depletion therapies for some cancer types are currently being investigated which is expected to make tumor cells more prone to drugs and other modes of therapy (33).

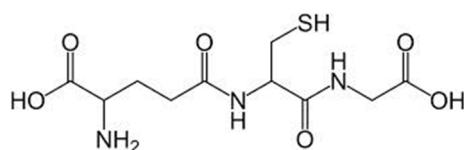


Figure 5: Structure of glutathione

GSH concentration can be as high as 10mM in malignant tumors while it doesn't exceed 5mM in healthy tissues. As a result, any disulfide groups internalized into these tumors are reduced to thiols much more rapidly than healthy tissues. This concept can be used to selectively release drug molecules inside tumor cells by designing drug carriers that contain disulfide linkages. These linkages can be used in the structure of the carrier which will cause the carriers to disintegrate in tumor cells, releasing the payload (34). On the other hand, covalently attaching

modified drug molecules to nano-carriers or cross-linking the carriers via disulfide linkages is another strategy that gives the system additional extracellular stability. Covalently attached drug molecules and cross-linked carriers prevent premature drug release by diffusion. Since GSH concentration in the extracellular environments is much lower than intracellular concentration this strategy also provides an intracellular-only drug release mechanism. (35) In an example study, disulfide bonds are used to attach both camptothecin (CPT) molecules (anti-cancer agent) and PEG chains on polymer nanoparticles. This resulted in excellently stable nano-carriers that will shed their PEG coating and start releasing drugs due to disulfide bond cleavage upon internalization as seen in figure 6. The polymer used in the study has disulfide containing pendant group on each repeating unit. Some of these pendants are left as free terminal amines while some of them were used for attaching PEG chains or CPT molecules. After nanoparticle formation, hydrophobic camptothecin molecules stayed inside the nanoparticles while hydrophilic amines and PEG chains remained on the surface. Amines on the surface are used for attachment of an active targeting agent for a specific type of breast cancer cell line. After internalization and cleavage of disulfide bridges in the pendants, PEG coating dissociates and camptothecin molecules are released inside the cells in their thiolated form. (36)

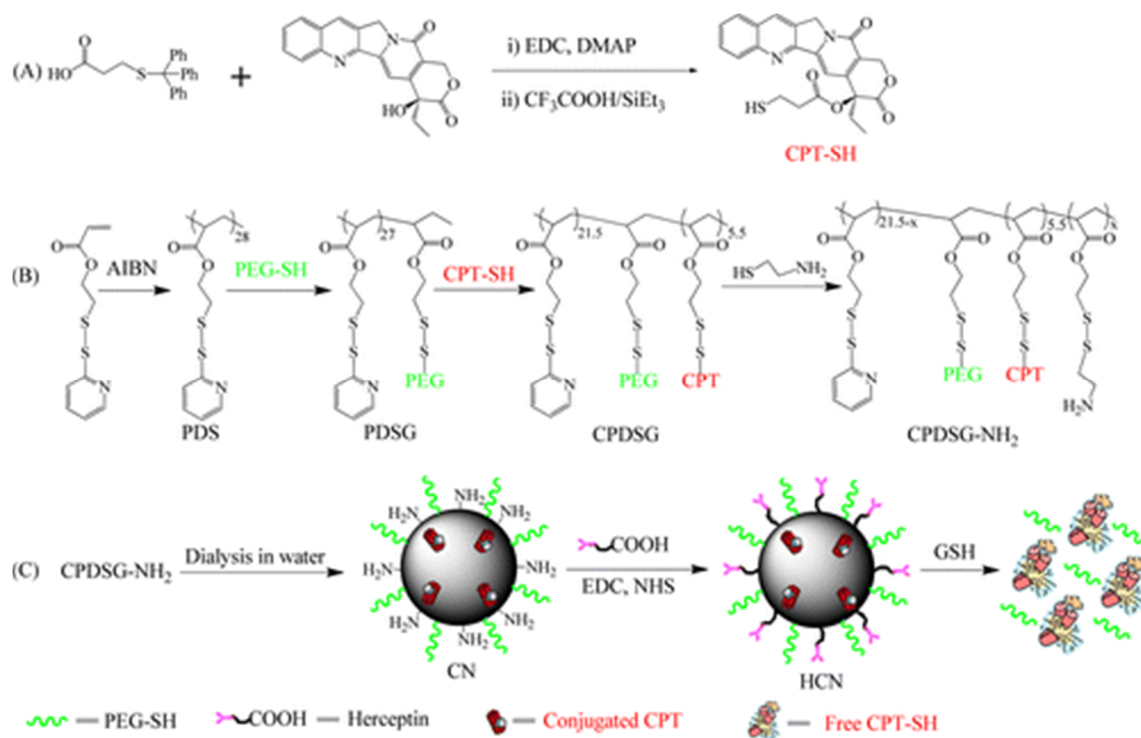


Figure 6: Synthetic steps and illustration of redox sensitive PEG coated camptothecin carriers. Reproduced with permission from (36). Copyright 2014, American Chemical Society.

Lipoic acid side chains is another elegant way of obtaining disulfide cross-linked drug carriers. Lipoic acid molecules contain disulfide bonds within themselves as seen in Figure 7 and their carboxylic acid site makes them extremely easy to attach on polymer side chains.

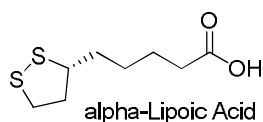


Figure 7: Structure of alpha-lipoic acid

Nanoparticles of lipoic acid functionalized polymers are able to be cross-linked with disulfide bridges by reducing 10% of lipoic acid molecules in the nanoparticle batch with a reducing agent. The free thiols exposed after reduction starts reducing other lipoic acids inside the nanoparticles and resulting chain of thiol-disulfide exchange reactions cause a lot of disulfide bridges to form between polymer chains. This makes the nanoparticles more stable and also redox sensitive. (37)

1.3 Conjugated Polymers

Conjugated polymers differ from conventional polymers with their ability to have extraordinary properties such as conductivity, semi-conductivity, photoluminescence, electroluminescence and electrochromism. These properties emerge from π -electron systems along polymer backbones. Conjugated backbones consist of adjacent unsaturated sp^2 or sp hybridized carbon atom chains whose p orbitals are aligned and overlap which creates the conjugation. This allows delocalization of π electrons across the entire backbone since conjugation continues unbrokenly throughout the polymer chain. These delocalized π electrons do not belong to a single bond or atom but the whole polymer chain. The first synthesized and simplest conjugated polymer poly acetylene is displayed in Figure 8 where conjugation can be identified by tracking alternating single and double bonds throughout the chain. (38)

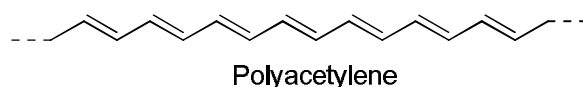


Figure 8: Structure of the first synthesized conjugated polymer polyacetylene

Overlapping of p-orbitals create valence and conduction bands within the molecule which are highest occupied molecular orbital (HOMO) and lowest unoccupied molecular orbital (LUMO) respectively. The energy difference between these orbitals is called the band gap and for conjugated polymers this value is typically between 1.5 and 4 eV. The band gap determines physical properties of a material as seen in Figure 9. Large band gaps mean insulating materials since electrons cannot jump to conduction band while overlapping HOMO and LUMO levels mean a conducting material. (39)

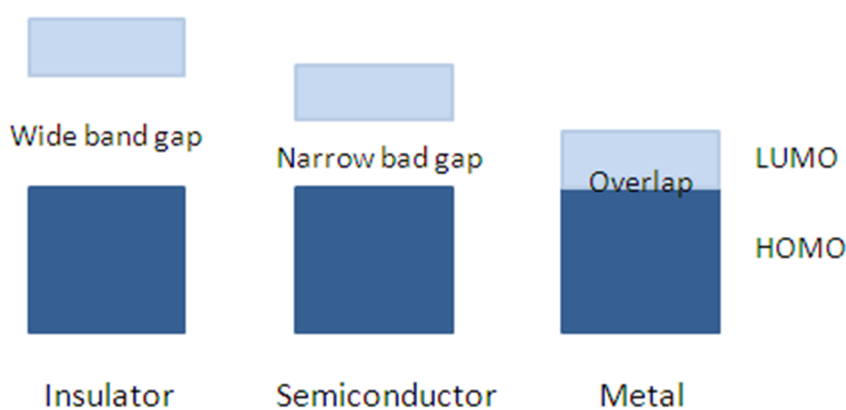


Figure 9: Band gap representations of insulators, semi-conductors and conductors.

In the case of conjugated polymers, band gap is narrow enough for electrons to absorb energy and jump to LUMO. Electrons from HOMO absorb light in the wavelength that corresponds to the band gap energy and jump to LUMO. Absorbing light in specific wavelengths creates colors of molecules. The band gap usually decreases with increased conjugation length and the molecules absorb light in wider wavelengths (less energetic light) causing the color shift towards red. Conjugations that consist of less than eight double bonds usually absorb light in the ultraviolet region and are colorless.

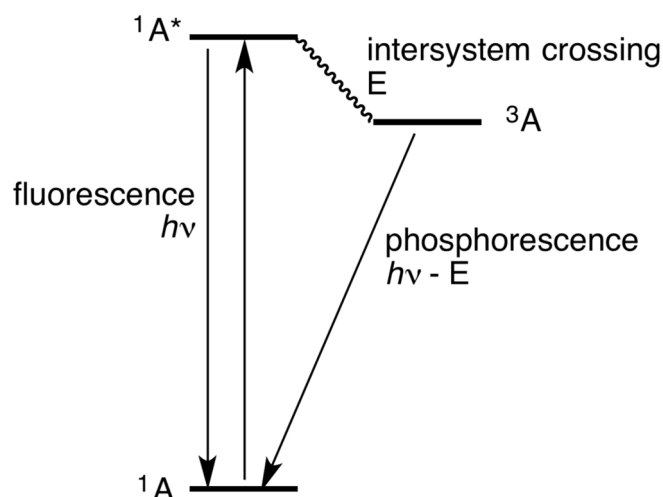


Figure 10: Jablonski diagram showing fluorescence and phosphorescence events.

Excited electrons in the LUMO level then lose their energy and return to their ground state by giving out the extra energy as photons which is called a radiative relaxation as seen in Figure 10. This event is called fluorescence and the wavelength of the emitted photon is directly determined by the band gap. If the electron in the excited state makes a non-radiative intersystem crossing to the triplet state before relaxing to ground state this is called phosphorescence.

Conjugated polymers have the fluorescence ability while having all other advantageous properties of polymers. Their band gaps depend on their structure and conjugation length which is also a function of their molecular weight. Therefore their absorbance and emission properties are tunable by changing the structure and the molecular weight. They have high molar absorptivity and quantum yield values. Moreover, they have excellent photostabilities meaning they are not prone to decomposition by photobleaching. Conjugated polymers do not contain any heavy metals and generally have good cytotoxic profiles. These properties make them excellent candidates in many different biological applications since they can easily be made into water-dispersible stable nanoparticles. Conjugated polymer nanoparticles (CPNs) can be used as drug carriers while acting as fluorescent tags simultaneously which makes them excellent candidates for many theranostic applications. (40)

1.4 Nanoparticle Preparation from Conjugated Polymers

Conjugated polymers typically show hydrophobic behavior due to their non-polar backbones unless they are decorated with suitable polar groups for water solubility. Water dispersible

conjugated polymer nanoparticle formation mainly utilizes hydrophobicity of polymers where chains favor the conformation with smallest contact surface with water. When water is added directly onto polymer solids no interaction with water is observed but nanoparticle preparation methods use solutions of these polymers. Namely there are two basic methods for preparing CPNs: nanoprecipitation and miniemulsion. (41)

Nanoprecipitation method involves dissolving the polymer in a good solvent that is miscible with water and adding this solution into excess water as represented in Figure 11. The relaxed polymer chains that float freely inside the solution suddenly collapse into small spheres upon contact with water and act as nucleation sites. Other polymer chains start accumulating on these nucleation sites to minimize their contact surface with water and become spherical nano-scale particles. However after formation of nanoparticles, interaction of polymer chains with the solvent molecules that are present in the aqueous medium continues. Evaporation of these solvent molecules causes them to solidify and become more rigid and stable. This can also be observed by the slight drop in hydrodynamic volume after solvent evaporation. This is why in addition to being a good solvent and being miscible with water, a low boiling point is also a desirable property while choosing a solvent. (42)

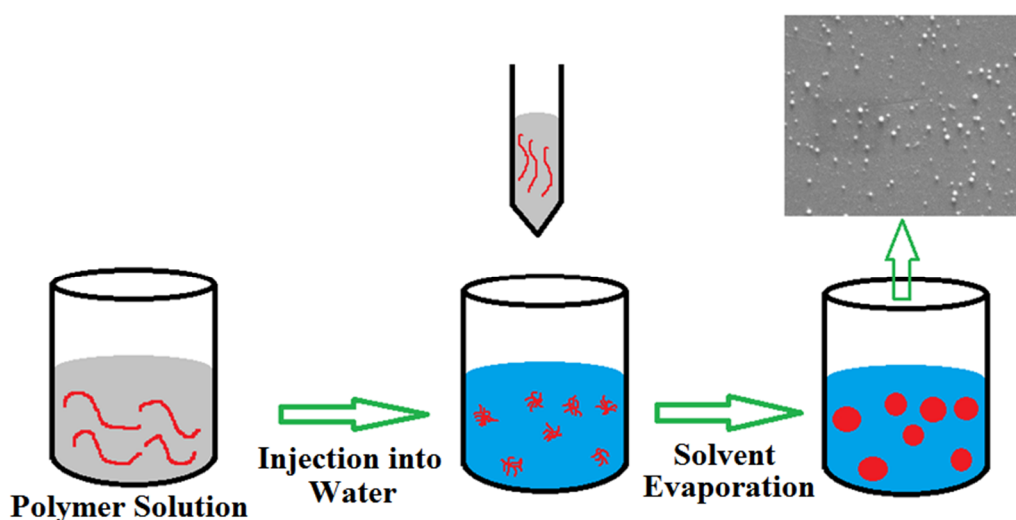


Figure 11: Schematic representation of nanoprecipitation method.

Almost every parameter in the process affects the properties of resulting nanoparticles. The concentration of the initial polymer solution is the main parameter that changes the nanoparticles size distribution. More concentrated solutions result in larger nanoparticles. Using a higher amount of polymer means more chains that are accumulated on nucleation sites and larger nanoparticles. Amount of the solvent can be increased to obtain smaller

nanoparticles but the final water-solvent mixture should not become a solvent for the polymer chains. Using more water means more nucleation sites and smaller nanoparticles. Polymers with higher molecular weights result in larger nanoparticles. Stirring or sonicating the water while adding the solution gives the polymer chains the energy and mobility to reach their final energetically favorable configurations. Sonication or stirring can affect the results differently for different polymers as it is reported to decrease polydispersity of particle size distribution for some polymers while other studies reported no difference between stirring and not stirring. All these parameters can be manipulated in a nanoprecipitation process to obtain CPNs with size and polydispersity suitable for different applications. It is possible to obtain nanoparticles as small as 5nm average diameter with nanoprecipitation. (43)

In the case of miniemulsion, the solvent used for dissolving the polymer is not miscible with water like chloroform, dichloromethane or toluene. This solution is added into an aqueous solution of a surfactant to form an emulsion where polymer solution is dispersed into water in the form of nano-sized droplets. After evaporation of the solvent, solid nanoparticles are formed. The size distribution of the nanoparticles is still dependent on the polymer concentration and can be as small as 30nm. The difference is, surfactant molecules stay inside the nanoparticle dispersion and they may not be suitable for biological applications if the surfactant type is not chosen carefully. Extra purification steps may be required to get rid of these surfactant molecules to avoid any complications. (44)

In both of these nanoparticle preparation methods, hydrophobic drug molecules that are desired to be loaded inside the nanoparticles are co-dissolved with the polymer in the initial solution. During the nanoparticle formation process, drug molecules prefer being located in the non-polar interior environment of the nanoparticles due to hydrophobic effect. Moreover, other weak interactions between drug molecules and polymer chains play an important role in loading of drugs into nanoparticles. For example, conjugated polymers with aromatic backbones can form π - π interactions with aromatic drug molecules which increases the efficiency of drug loading compared to non-aromatic polymers. This gives conjugated polymers another edge against conventional polymer drug carriers. (45)

1.5 Applications of Conjugated Polymer Nanoparticles

Conjugated polymer nanoparticles have been used in biological field as well as optoelectronic and photonic applications due to their advantages such as high brightness, excellent photostability, low cytotoxicity, high quantum yield and versatile surface chemistry. (41) Their ability to be functionalized with different specific recognition elements renders them excellent candidates for drug and gene delivery while simultaneously monitoring release process in real-time due to their self-luminescent properties. (46) Moreover they can be used for their intrinsic photosensitization properties for cell killing as seen in Figure 12.

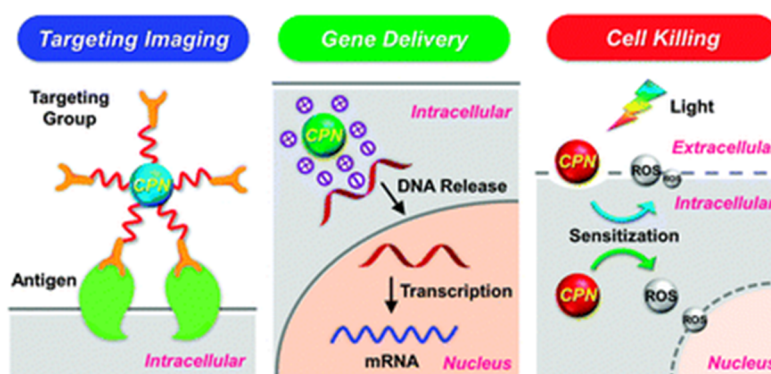


Figure 12: Biomedical applications of CPNs. Reproduced with permission from (46). Copyright 2013, Royal Society of Chemistry.

Besides simultaneous therapy and imaging of tumors, these nanoparticles are also important in understanding pharmacokinetics and biodistribution of anti-cancer agent loaded nanoparticles in living organisms. (47) CPNs can basically be loaded with anticancer agents to carry them to tumor sites via EPR effect while bioimaging is enabled by the intrinsic luminescence of nanoparticles. (45) In several studies, they are shown to be internalized by cells and have no intrinsic cytotoxicity in cell assays done with blank nanoparticles. (45) (48) (49) CPNs can also be designed for targeted drug delivery and specific imaging by conjugation of specific active targeting molecules such as a peptide sequence, sugar, protein or antibody. (46) For example it was reported that multiple types of CPNs co-encapsulated with poly (DL-lactide-co-glycolide) (PLGA) showed low cytotoxicity and decent cell internalization. Upon covalent attachment of

folic acid molecules to these CPNs, internalization by MCF-7 breast cancer cells was enhanced due to high affinity of folic acid towards over-expressed receptors in these cells. (50)

It was also shown that CPNs that emit light in the NIR region can be synthesized and enable tracking of drug loaded nanoparticles in vivo. A pH sensitive system was developed for this purpose. (51) Red emitting anti-cancer agent doxorubicin was loaded into m-dextran pH sensitive carriers along with an NIR emitting conjugated polymer BTTPF. Förster resonance energy transfer occurs between doxorubicin and conjugated polymer within the carrier as seen in Figure 13 since they are in close proximity of each other inside the carrier. Once the carrier starts disintegrating, energy transfer stops due to increased distance between doxorubicin and conjugated polymer chains. This allows tracking of intact nanoparticles only by monitoring the energy transfer throughout the body and drug release is also monitored by tracking conjugated polymer channel only.

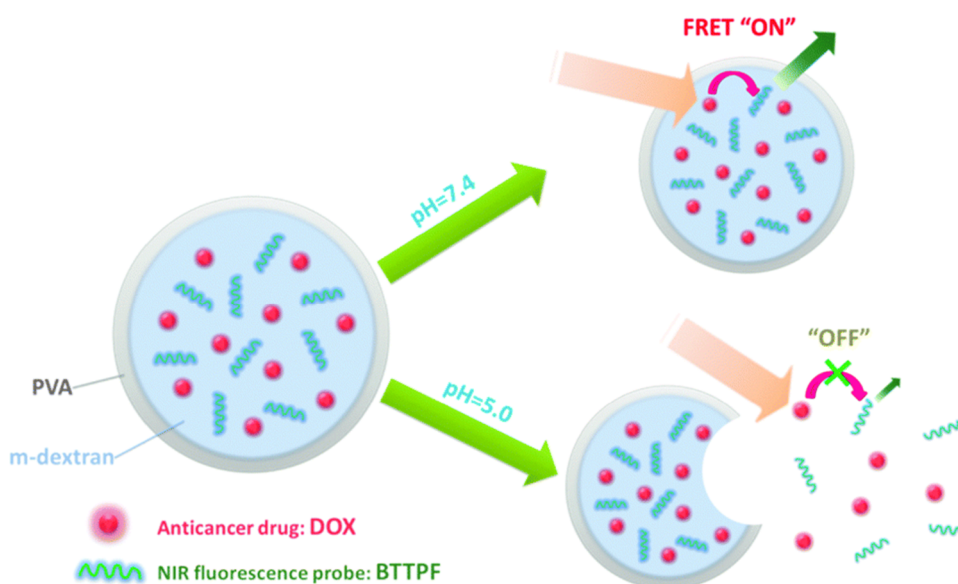


Figure 13: Schematic representation of pH sensitive tracking of CPNs by using FRET between doxorubicin and conjugated polymer BTTPF. Reproduced with permission from (51) Copyright 2014, Royal Society of Chemistry.

Some CPNs were also shown to have anti-bacterial properties. It was found that a cationic CPN can coat negatively charged surfaces of some microbial pathogens and visible light irradiation causes singlet oxygen generation leading to membrane damage and ultimately death of pathogens. (52)

1.6 Aim of the thesis

This study targets to synthesize different biocompatible, water-dispersible, stimuli-sensitive conjugated polymer nanoparticles that can efficiently deliver anticancer agent camptothecin to tumor sites while reducing systemic effects of camptothecin with the help of EPR effect and tumor specific stimuli sensitivity. It was hypothesized that nanoparticles will stay rather intact in the extracellular environment due to the lack of pH or reduction stimuli needed for faster drug release but will rapidly release camptothecin molecules upon internalization inside the cells where appropriate stimuli is present as seen in Figure 14 while simultaneously acting as fluorescent markers for different modes of bioimaging applications. Three different types of stimuli responsive conjugated polymer nanoparticles are synthesized for this purpose.

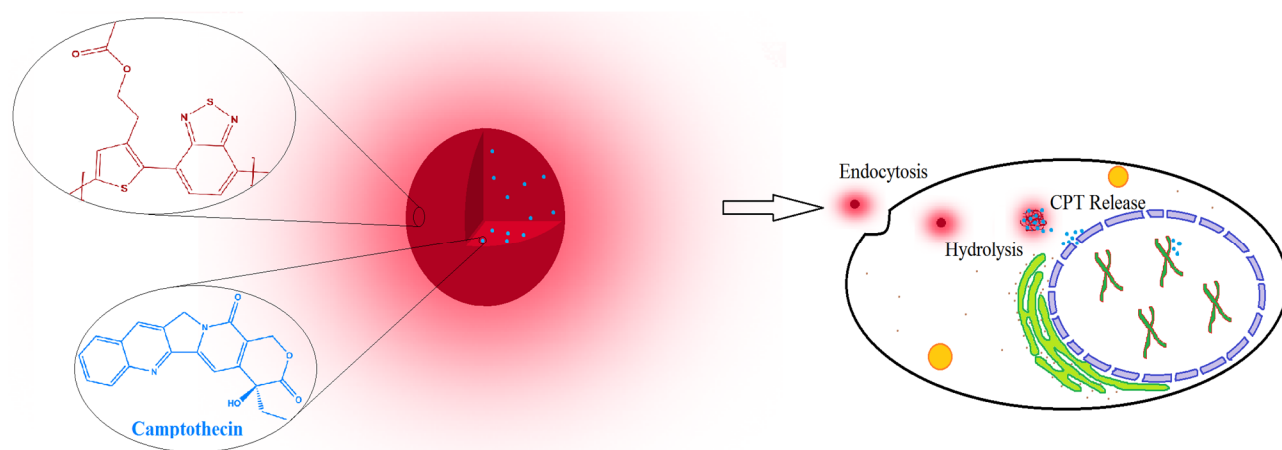


Figure 14: Schematic illustration of a stimuli-sensitive theranostic platform designed in this work.

Firstly, pH sensitive, red emitting conjugated polymer 2-(2-(benzo[c][1,2,5]thiadiazol-4-yl)thiophen-3-yl)ethyl acetate (PBT-(Ac)) was synthesized and characterized. This polymer has acetyl protected hydroxyl groups on its pendants which makes it hydrophobic enough to form

nanoparticles at neutral pH levels. Acetyl groups are hydrolyzed at acidic pH to expose hydroxyl groups to make the polymer more hydrophilic and disrupt the nanoparticles. This concept was used to release CPT molecules more rapidly in acidic tumor microenvironments. Prepared blank and CPT loaded nanoparticles were characterized by different microscopic and spectroscopic methods and their drug loading performances and drug release profiles at different pH values were determined. Their biological activity was evaluated with cell viability assays and their interactions with Huh7 cells were visualized by using a fluorescence microscope.

Another pH sensitive polymer poly{3-[9-(3-tert-Butoxycarbonylamino-propyl)-3-methyl-6-(7-methyl-4,7-dihydro-benzo[1,2,5]thiadiazol-4-yl)-9H-fluoren-9-yl]-propyl}-carbamic acid tert-butyl ester (PBF) was synthesized and characterized which emits in the green region. This polymer has pendant groups containing t-Boc protected amines which are also hydrophobic at neutral pH values. Amines are deprotected at slightly acidic pH and exposes positively charged amine groups. Hydrophilicity of these groups and strong repulsion between them disrupts nanoparticles of this polymer causing faster drug release in acidic environments. Nanoparticles of this polymer were prepared and their CPT loading characteristics and release profiles at different pH values were studied. Their cytotoxicity was evaluated with cell viability assays and fluorescence microscopy images were used to visualize them inside Huh7 cells.

Finally, a redox sensitive, red emitting polymer (R)-2-(2-(benzo[c][1,2,5]thiadiazol-4-yl)thiophen-3-yl)ethyl 5-(1,2-dithiolan-3-yl)pentanoate (PBT-LA) was synthesized and characterized. This polymer has lipoic acid groups attached on side chains. After formation of nanoparticles from this polymer, a certain percentage of lipoic acid groups are reduced with a strong reducing agent dithiothreitol (DTT) to expose free thiols. These free thiols cause a chain of thiol-disulfide exchange reactions within the nanoparticles that completely cross-links them with disulfide bridges. These bridges will be cleaved by the excess GSH in tumor cells to disrupt the nanoparticle and cause faster drug release. After nanoparticles were prepared, they were characterized and their cross-linking was confirmed with several different methods. Their drug loading performances and drug release profiles in presence and absence of GSH were determined. The biological activity of blank and CPT loaded CPNs was evaluated with cell viability assays and their interactions with Huh7 cells were visualized by using a fluorescence microscope.

CHAPTER 2

RESULTS AND DISCUSSION

2.1 Introduction

This chapter consists of two main sections. First section involves the results and discussion on the synthesis, characterization of two different pH-responsive green and red emitting polymers as well as their nanoparticle preparation, characterization and evaluation of these nanoparticles in vitro cancer cell assays.

Second section covers the studies on redox-responsive conjugated polymer nanoparticles. In this section, the synthesis and characterization of monomers and polymer as well as the nanoparticle preparation and in vitro cell assay will also be discussed.

2.2 pH-Responsive Conjugated Polymer Nanoparticles

Two different pH-responsive conjugated polymers were designed and synthesized. The polymers are designed to react and become more hydrophilic at low pH environments so that their nanoparticles swell with water at acidic environments of tumors and deliver the payload more rapidly. Green emitting polymer poly{3-[9-(3-tert-Butoxycarbonylamino-propyl)-3-methyl-6-(7-methyl-4,7-dihydro-benzo[1,2,5]thiadiazol-4-yl)-9H-fluoren-9-yl]-propyl}-carbamic acid tert-butyl ester (PBF) was designed to have two amine groups protected with t-boc groups as pendants. Protecting t-boc groups are hydrolyzed in acidic environment and expose charged amine groups. Red emitting polymer 2-(2-(benzo[c][1,2,5]thiadiazol-4-yl)thiophen-3-yl)ethyl acetate (PBT-(Ac)) has acetoxy groups on the side chains which are hydrolyzed to hydrophilic hydroxyl groups under acidic pH values.

These exposed hydrophilic moieties cause CPNs to swell in physiological aqueous environment and cause a faster drug release in acidic environment of tumor sites.

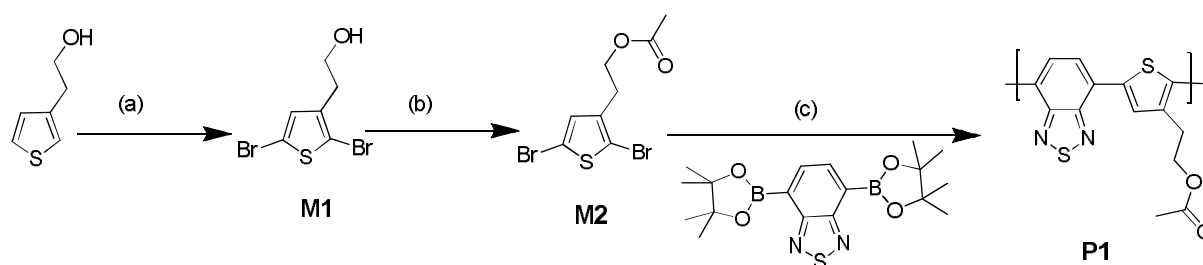
2.2.1 Synthesis and Characterization of Red Emitting pH-Sensitive Polymer Nanoparticles

Red emitting, pH sensitive polymer (PBT-(Ac)) was synthesized and characterized followed by preparation of nanoparticles from this polymer. Blank and drug loaded nanoparticles were characterized by different spectroscopic and microscopic techniques and in vitro cell assays

were performed to estimate their biological activity. Polymer synthesis and nanoparticle synthesis are given separately in following two subsections of this section.

2.2.1.1 PBT-(Ac) Synthesis and Characterization

PBT-(Ac) was synthesized according to Scheme 1. Firstly, commercially available 2-(thiophen-3-yl) ethanol molecule was brominated on 2 and 5 positions of the thiophene using the brominating agent, N-bromosuccinimide. The reaction was fairly simple and yielded the product in one spot on TLC. However after being kept in the fridge overnight, different minor spots started to appear indicating the decomposition of the product. Therefore as soon as the reaction was completed, the freshly prepared monomer was used for the next step.



Scheme 1: Reaction scheme for PBT-(Ac). (a) 2-(thiophen-3-yl)ethanol, NBS, EtOAc, 25° C, 12 h, 60% (b) acetic anhydride, pyridine, 25 ° C, 12 h, 90% (c) THF/toluene/H₂O (1:1:1, v/v), K₂CO₃ (aq.), tetrabutylammonium bromide (TBAB), Pd(Ph₃)₄, 80 ° C, 72 h, 46%.

Figure 15 shows the ¹H-NMR spectrum of the brominated product where there is a singlet at 6.8 ppm due to the single aromatic proton of thiophene. Two triplets are also visible at 2.8 and 3.8 ppm coming from the pendant's -CH₂ residues.

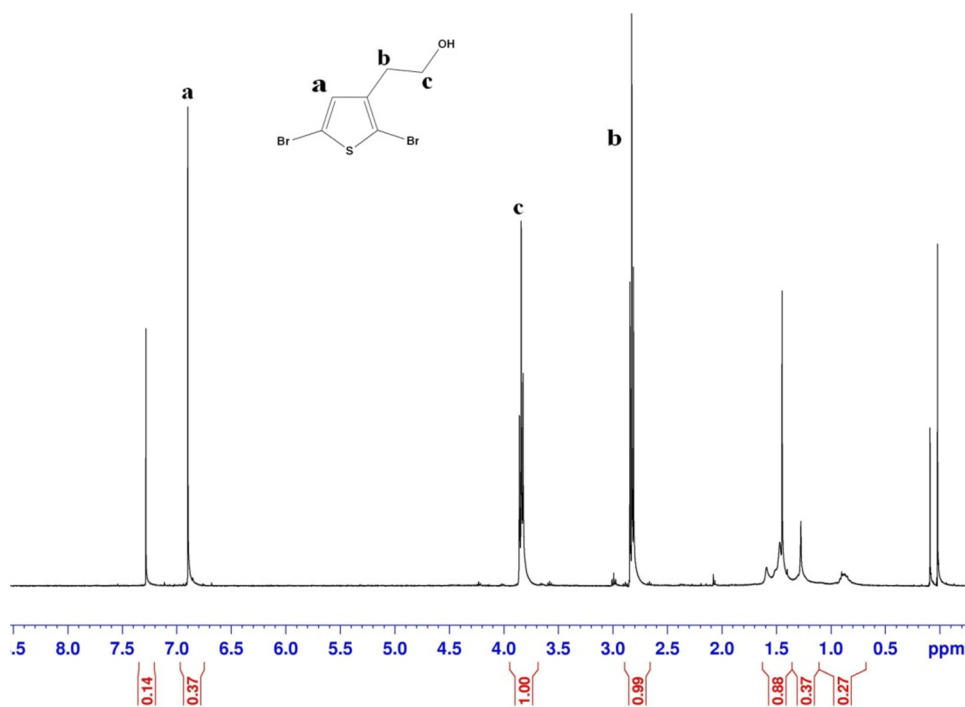


Figure 15: ¹H-NMR (400 MHz, 25 °C, CDCl₃) spectrum of M1.

Hydroxyl group of this molecule was protected with an acetoxy group prior to Suzuki coupling to prevent any complications that can reduce the yield of polymerization. A mild reaction set up with acetic anhydride yielded the protected product molecule with 90% yield. The most significant change was the appearance of a peak at about 2 ppm in the ¹H-NMR spectra, coming from the CH₃ at the end of the acetoxy group which is labeled as *a* in the spectrum in Figure 16. The protons from the body of the pendant labeled as *b* and *c* are still visible and they have 2/3 of the integration of *a*, which confirms the attachment of acetoxy group.

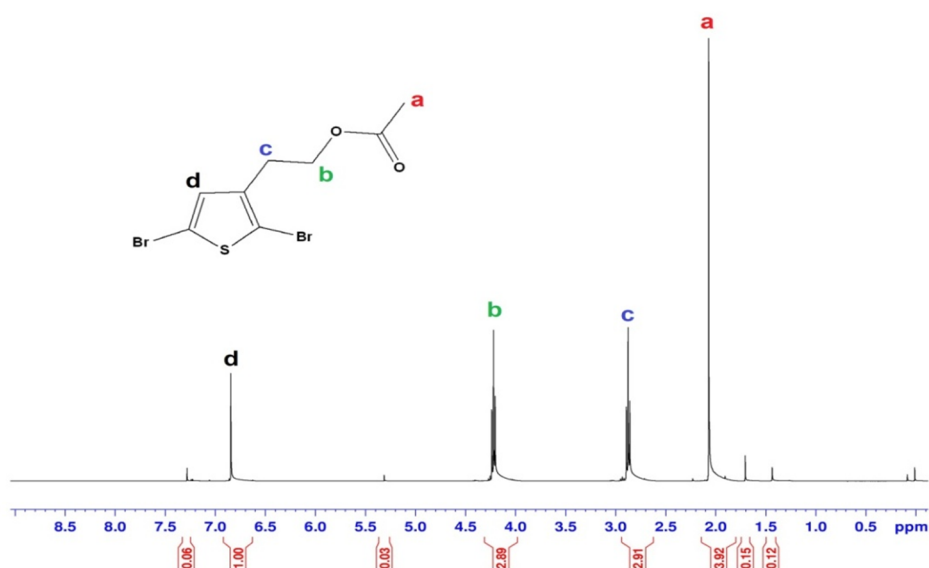


Figure 16: $^1\text{H-NMR}$ (400 MHz, 25 °C, CDCl_3) spectrum of M2.

This molecule was then reacted with benzothiadiazole di-functionalized with boronic ester in a Suzuki coupling reaction to form C-C bonds between aromatic rings of thiophene and benzothiadiazole. This reaction yielded the conjugated polymer PBT-(Ac) which was then purified by washing with methanol and water; then the residue was dissolved in a minimum volume of THF and precipitating into excess amount of cold methanol. Polymer was highly soluble in THF, chloroform, DMF, acetonitrile and DMSO and partially soluble in acetone.

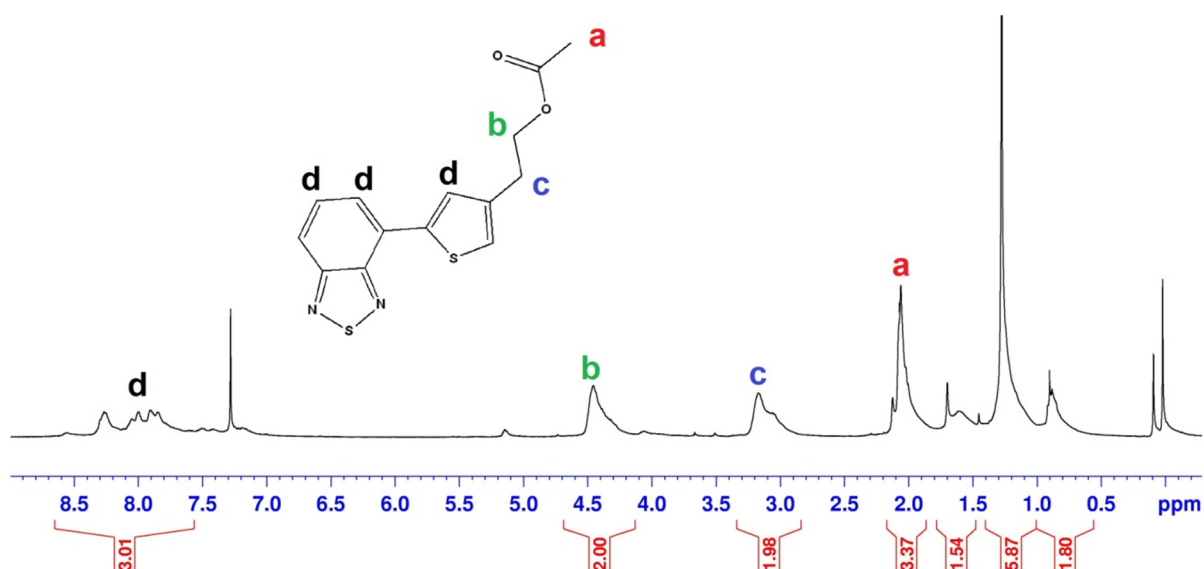


Figure 17: ¹H-NMR (400 MHz, 25 °C, CDCl₃) spectrum of PBT-(Ac).

Resulting polymer PBT-(Ac) was characterized by ¹H-NMR spectroscopy as seen in Figure 17. The chemical shifts labeled as a,b,c and d confirm the suggested structure of the polymer. They are almost at the same position with the monomer and their integrations are exactly what they are expected to be. The three aromatic protons give an integration value of approximately 3 while CH₂ protons of the side chains give integration values around 2. The shift labeled b which comes from the CH₃ of the acetyl group gives an integration value of approximately 3 which corresponds to three protons. The peaks below 2 ppm did not disappear with any purification techniques and are attributed to boronic ester residues at the end groups.

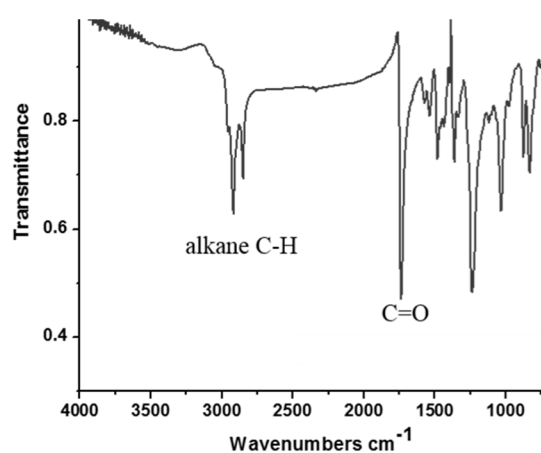


Figure 18: FTIR (KBr pellet) spectrum of PBT-(Ac).

The FTIR spectrum of PBT-(Ac) Figure 18 clearly shows a strong absorbance band at around 1750 cm^{-1} which comes from the carbonyl stretching of acetoxy protecting group. This absorbance becomes important at other stages where acetoxy group is hydrolyzed to yield a hydroxyl group in which case carbonyl stretching is expected to disappear.

The polymer was further characterized with elemental analysis. The experimental results obtained are compared with theoretical values of a single repeating unit. The comparisons are within the acceptable ranges for comparing the polymer with its repeating unit by taking into consideration the end groups.

Thermal properties of PBT-(Ac) were also characterized by differential scanning calorimetry (DSC) and thermal gravimetric analysis (TGA) methods. Figure 19 shows DSC graph of PBT-(Ac). The first endothermic linear drop was attributed to glass transition temperature and was calculated to be around $80\text{ }^{\circ}\text{C}$. The large endothermic dip is not very sharp but can be attributed to melting of the polymer which gave a melting point of $143\text{ }^{\circ}\text{C}$. The exothermic processes that occur above $200\text{ }^{\circ}\text{C}$ are attributed to polymer decomposition which is also confirmed by the TGA measurement.

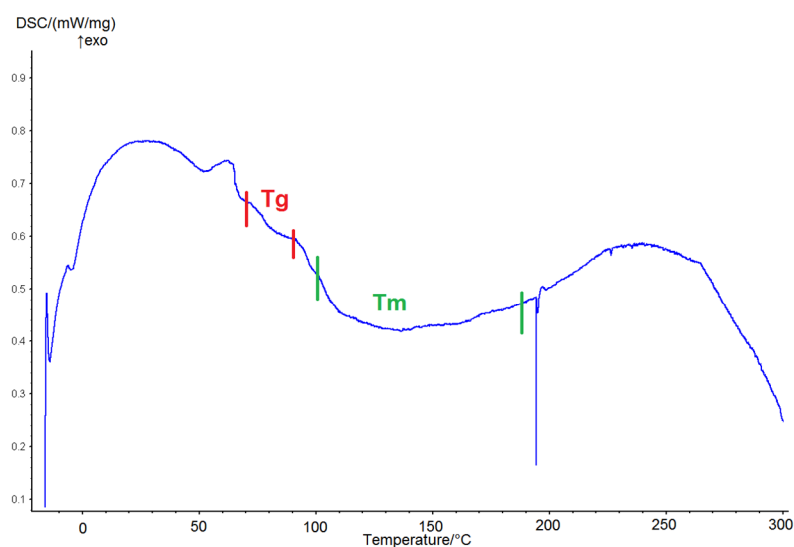


Figure 19: DSC graph of PBT-(Ac).

Figure 20 shows the TGA graph of PBT-(Ac) where the polymer slowly starts to lose weight at $200\text{ }^{\circ}\text{C}$. The breaking of the weight loss line at about $450\text{ }^{\circ}\text{C}$ where 28.6% of the total weight lost was attributed to total decomposition of pendant groups since pendants make up the 28.6%

of the polymer's weight. Above this temperature, the backbone continues decomposing slowly and steadily until 1000 °C where the experiment was ended.

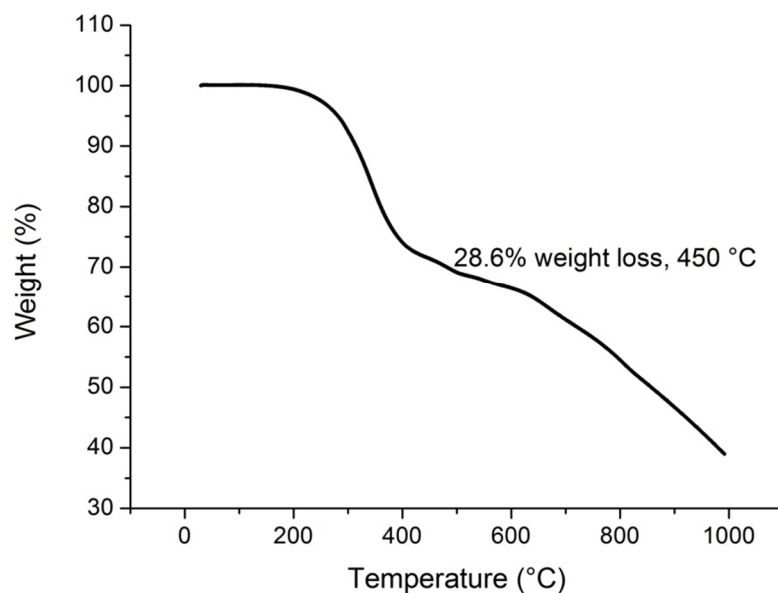


Figure 20: TGA graph of PBT-(Ac).

Optical properties of PBT-(Ac) were investigated by taking its UV-Vis absorbance and fluorescence emission spectra in different solvents. Figure 21 shows absorbance and emission spectra of PBT-(Ac) in THF. The UV-Vis absorption and emission spectra taken in the other solvents are also shown in Figure 24.

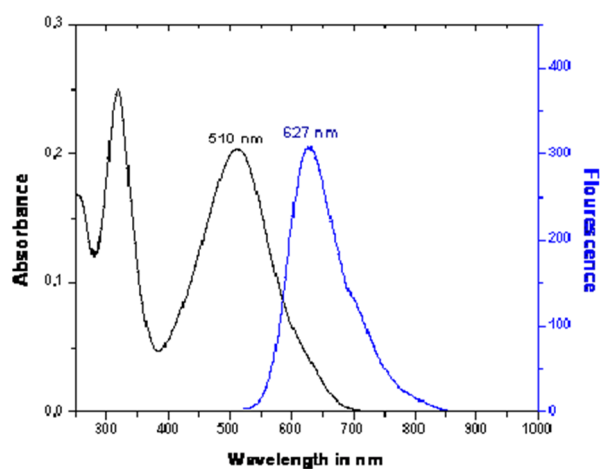


Figure 21: UV-Vis absorbance and PL emission spectra of PBT-(Ac) solution in THF.

2.2.1.2 Nanoparticle Preparation, Characterization and In Vitro Tests

Nanoprecipitation method was used straightforwardly to form CPNs from PBT-(Ac) polymer, in which polymer was dissolved in THF and injected into an excess amount of water while sonicating. Since hydroxyl groups of polymer were protected by acetoxy groups, polymer chains were entirely hydrophobic and formed CPNs with an average diameter of 56 nm. DLS measurements showed a single sharp peak and a polydispersity index of 0.05 which indicated a high quality size distribution without the need for any filtering. After characterizing them by DLS measurements, SEM images of blank and CPT loaded CPNs were taken. Figure 22 shows spherical shapes and narrow size distribution of PBT-(Ac) CPNs.

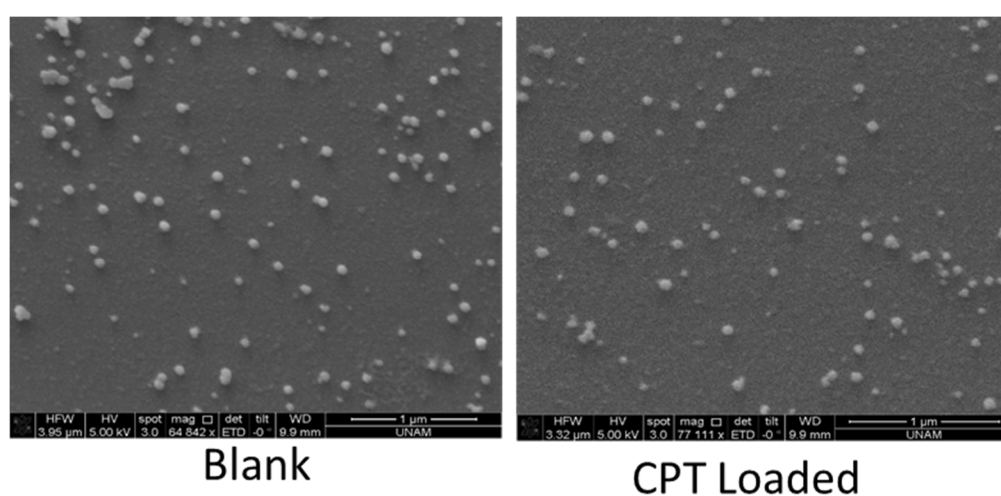


Figure 22: SEM Micrographs of Blank and CPT Loaded PBT-(Ac) Nanoparticles.

The nanoparticles were also checked for their stability in water to confirm a long enough shelf life. They were kept in ambient conditions for ten days and their sizes were monitored with DLS measurements which are shown in Figure 23. The size differences compared to their original diameters were quite insignificant and there were no observable aggregations in the dispersions which indicate a long shelf life.

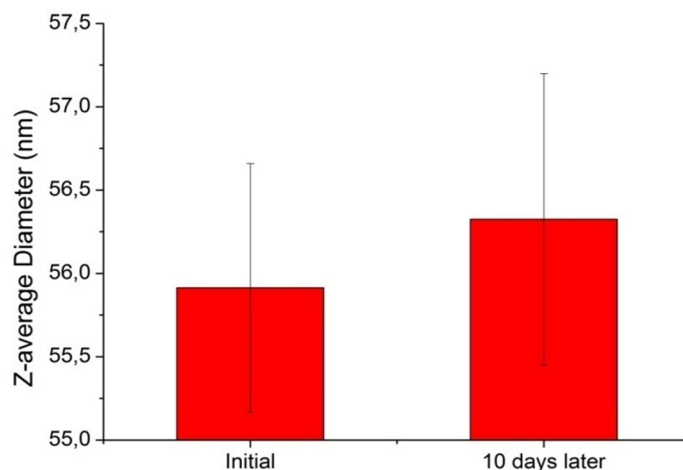


Figure 23: Stability of PBT-(Ac) nanoparticles in water over time.

The most striking change after forming the CPNs was the large red shift in the emission spectrum. The emission maximum jumped from 627 nm to 717 nm after forming CPNs as seen in Figure 24. Some bathochromic shifts were also observed in the emission wavelengths of the polymer as the solvent polarity increases but the large shift caused by water cannot only be explained by solvent effect. The large red shift can also mean that strong intermolecular interactions are created between polymer chains after they collapse into the tight matrix form they take in CPNs.

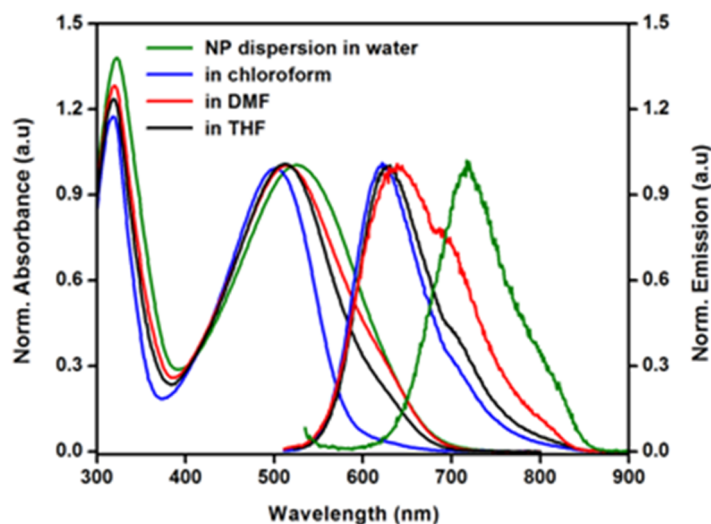


Figure 24: UV-Vis absorbance and PL emission of PBT-(Ac) solutions and aqueous nanoparticles.

pH Responsiveness of PBT-(Ac) nanoparticles was investigated through a method which combines a titration system with constant DLS and zeta-potential measurements. pH Value of a

CPN dispersion was decreased in a controlled manner by an automatic system and measurements were taken at certain pH levels. In this experiment it is expected to observe a diameter increase as the acetoxy groups are hydrolyzed to hydroxyl groups that interact with water molecules and cause CPNs to swell at low pH levels. This observation can be confirmed in Figure 25 where Z-average diameter increases from 56nm to 200 nm before reaching pH 5 and reaches to a value of 1000 nm just under pH 5.

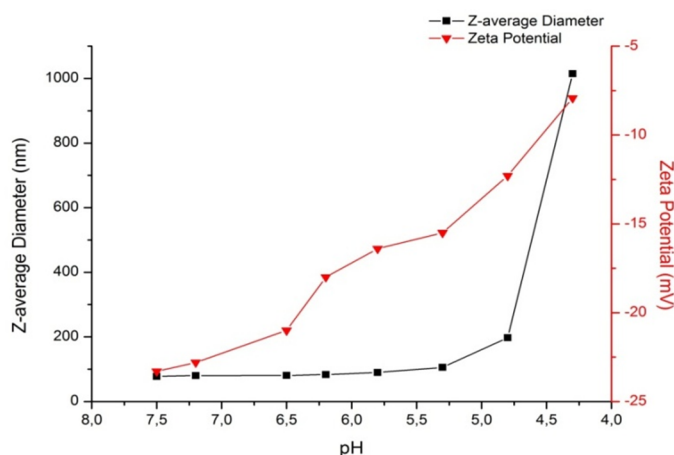


Figure 25: DLS and zeta-potential measurements of CPNs at different pH values.

Loading of anticancer drug CPT into CPNs was carried out by co-dissolving CPT with the polymer in THF prior to nanoprecipitation. Hydrophobic CPT molecules end up inside hydrophobic matrices of CPNs while they are forming inside the aqueous environment. The amount of CPT that ends up being encapsulated by the CPNs determines the drug entrapment efficiency and drug loading efficiency of the CPNs. Entrapment efficiency is the percentage of the total drug encapsulated by nanoparticles and loading efficiency is how many percent weight of the whole nanoparticles consists of drugs as in the formulae below.

$$\text{Entrapment efficiency} = \frac{(A_{\text{total drug}} - A_{\text{free drug}})}{A_{\text{total drug}}} \times 100\%$$

$$\text{Drug loading efficiency} = \frac{(\text{encapsulated drug})}{\text{maximum encapsulation}} \times 100\%$$

In order to calculate these values, drug loading experiments were carried out. Different PBT-(Ac) : CPT ratios were used while preparing CPT loaded CPNs and drug loading efficiency and drug entrapment efficiency values were calculated for each of these ratios to determine the

optimum ratio for preparing CPT loaded CPNs. After each batch is prepared, CPT loaded CPNs were loaded into dialysis tubes and immersed into a certain volume of 0.2% (vol/vol) tween 20 solutions. Tween 20 solubilizes unencapsulated CPT molecules, causing them to diffuse through the dialysis membrane into the dialysate. This dialysate solution is then analyzed by UV-Vis spectroscopy method to determine the amount of free CPT molecules in it. Subtracting this amount from the amount of total CPT used in that batch gives the amount of CPT that is loaded inside the CPNs. The amount of CPT loaded in the CPNs is used to calculate drug loading efficiency and drug entrapment efficiency from the formulae. Drug loading and drug entrapment efficiencies obtained from different PBT-(Ac) : CPT ratios were shown in the Figure 26. This experiment demonstrated that 1:6,25 CPT : polymer (w/w) ratio results in the maximum amount of drug being loaded inside the CPNs. Above this ratio, almost the same amount of drug is encapsulated and entrapment efficiency drops drastically due to excess amount of CPT that remains free.

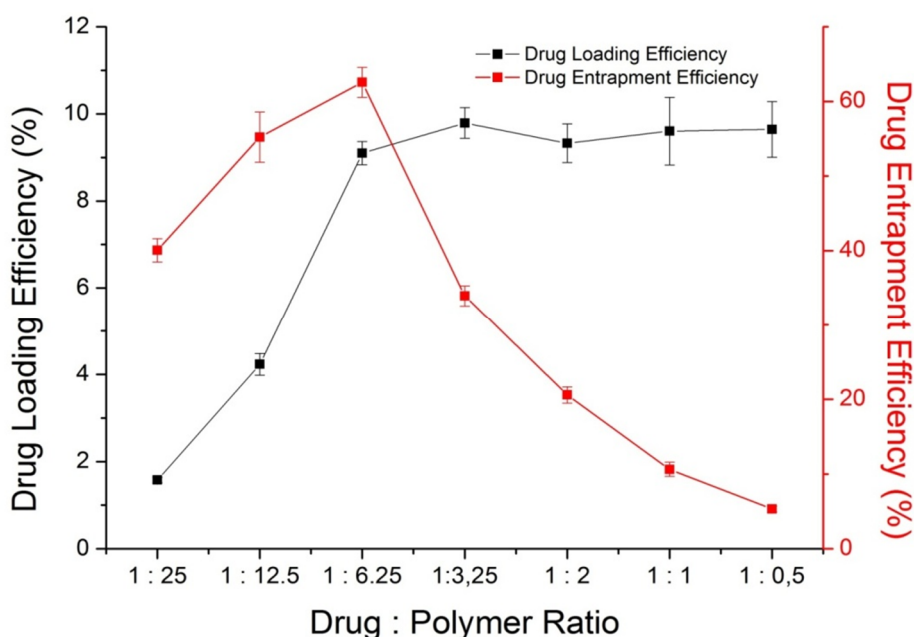


Figure 26: Drug loading and entrapment efficiency values determined for different drug:polymer ratios.

pH dependent drug release profile is studied by loading CPT loaded CPNs into dialysis tubes and adding either PBS (pH 7.4) or acetate (pH 5) buffer onto them. These tubes were then

immersed into 100ml of buffer solutions added onto them. 0,2% (vol/vol) tween20 was added into release mediums to solubilize released CPT molecules. Samples were taken from these buffers at different time intervals and concentration of free CPT was calculated from UV-Vis measurements of these samples and the calibration curve built from UV-Vis measurements of CPT solutions with known concentrations. Release medium was changed with fresh buffer at certain time intervals. As seen in Figure 27, acidic environment caused a faster CPT release by exposing hydroxyl groups and disrupting the nanoparticles.

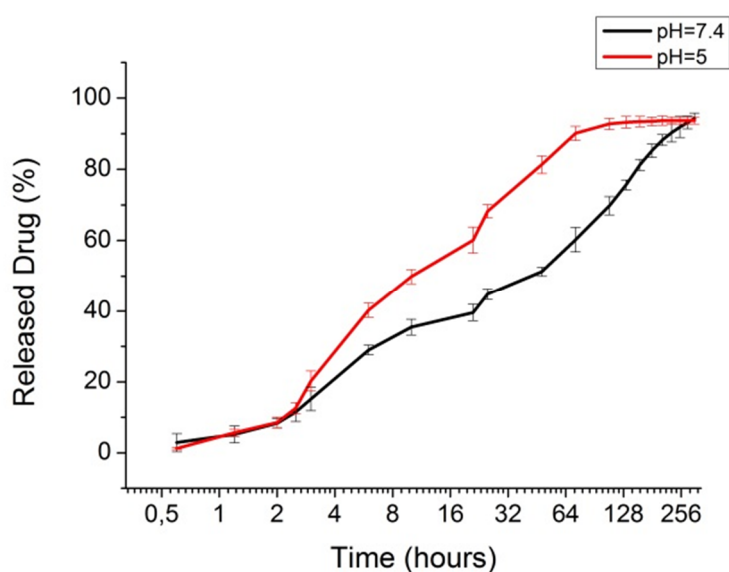


Figure 27: Time- dependent release profile of PBT-(Ac).

Next we investigated cytotoxicity of blank and CPT loaded CPNs by using a human hepatocarcinoma cell line huh7. A real time electronic cell sensing (RT-CES) assay was used to monitor their cytotoxic activity over time. This method involves seeding cells on gold plates and constantly measuring the impedance values of the gold plates. Impedance value of a plate increases when there are cells attached on its surface. Therefore, it is possible to measure cell viability of a culture just by measuring impedance value of a plate. This technique has many advantages over conventional cell viability assays since it doesn't use any fluorescent labels and it's possible to do real-time dynamic measurements. (53)

Huh7 cells were seeded onto plated for this technique and after they multiply and come to an equilibrium they are treated with blank and loaded CPNs and their viabilities are followed for 144 hours via monitoring gold plate impedances. Two different CPT loading rates were used

for both blank and loaded CPNs. CPNs denoted with the letter (A) carry one weight unit of CPT for every 62 weight units of polymer whereas CPNs denoted with the letter (B) carry the higher CPT : polymer ratio of 1: 10.4. It was decided to test two different loading rates in order to see the effect of drug loading on the efficiency of the drug. CPNs denoted with (A) were the lowest CPT concentration tried in the loading experiments while (B) were the ones which gave the maximum drug loading rate. The results are demonstrated in Figure 28.

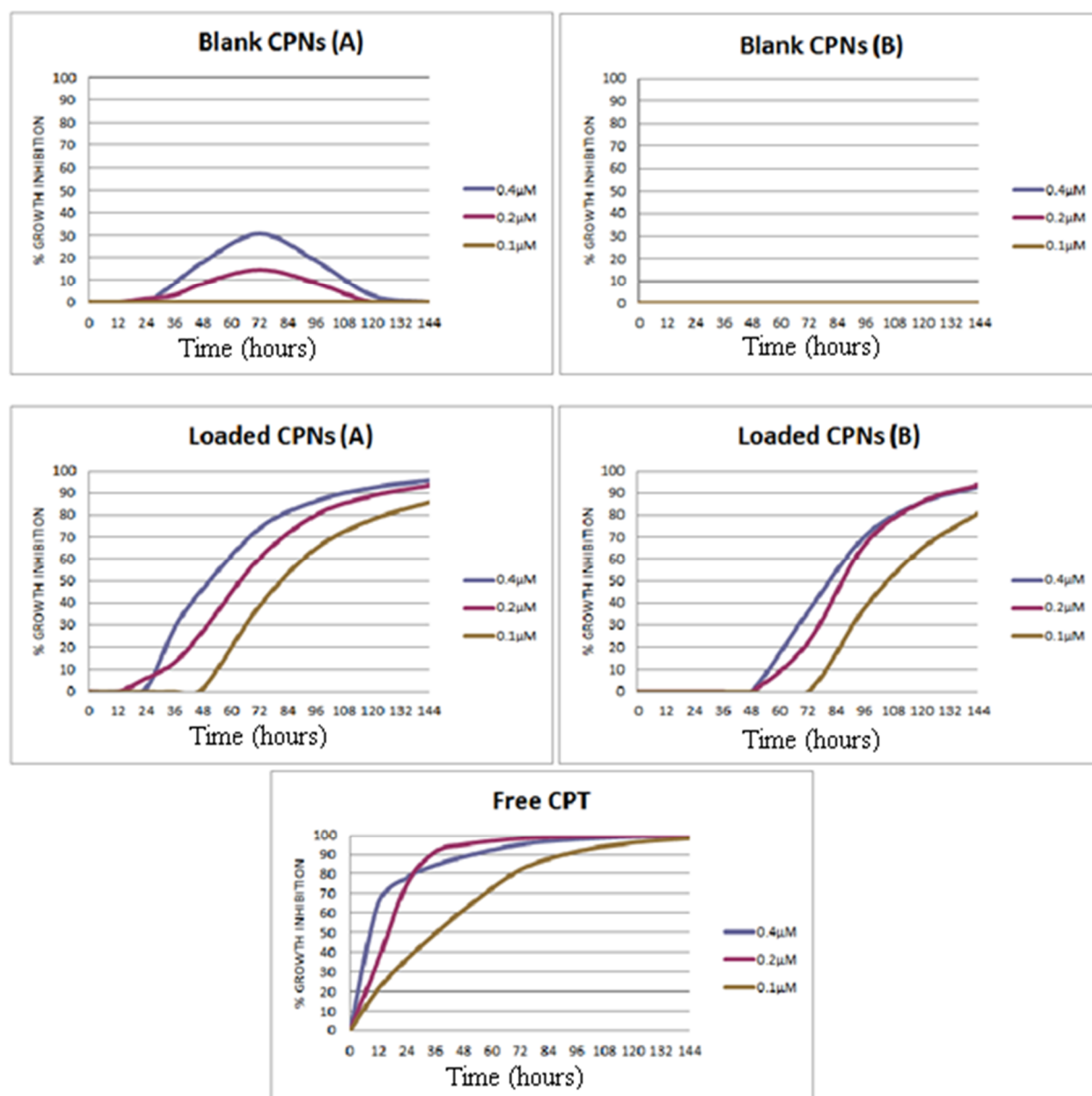


Figure 28: RT-CES results of blank and CPT loaded CPNs with different drug loading rates.

Blank nanoparticles of (A) at high concentrations appear to cause some changes in the cell behavior after 24 h incubation, growth inhibition reach to plateau values of 38 and 20%, for the nanoparticle concentrations of 0.2 and 0.4 μM, respectively, at 72 hrs and then the inhibition

rate decreases rapidly and the cells start to be responsive again and proliferate. This behavior may suggest the complex, dynamic nature of the interaction between the cells and nanoparticles. This could also be explained by an incidental enzyme interaction in which the NPs could randomly bind on some proteins to inhibit their activities, however, the cell signaling pathways get involved at this stage by increasing the expression of proteins to compensate the initial inhibition. As a result, this will cause no serious harm to the cells to go to apoptosis but only a temporary inhibition in the cell growth process. This effect is not observed in the loading rate (B) since it needs very little amount of CPNs to apply the needed dose of CPT thus there are much fewer nanoparticles that can interfere with cellular processes.

In both loading rates, the growth inhibition is slower than free CPT confirming the slow release feature of the nanoparticles supported by in vitro drug release studies in different pH values. The release is even slower in the case of the nanoparticles having high drug loading contents. This result can be attributed to strong interactions between CPT molecules and polymer chains because CPT molecules can interact with each other more freely due to presence of fewer polymer chains to interfere with this process. In lower loading rates, CPT molecules can be evenly distributed in the polymer matrix; not unlike dissolution. Upon cell internalization, these matrices interact with hydrophobic membrane structures and CPT molecules can easily diffuse into these membranes to show activity in the cell. However, higher CPT content can bring out the intrinsic solubility problem of hydrophobic drugs. CPT molecules can easily form highly stable aggregates via π - π stacking inside the sparsely packed matrix and their likelihood of interacting with cellular hydrophobic compartments drops drastically. Therefore they show little to no cellular activity for a long time after cell internalization. This result also indicates that in delivery of hydrophobic drugs, drug loading rates can affect the retention time of drugs inside the carriers so dosage and delay time of release can be tailored and optimized according to patient's needs.

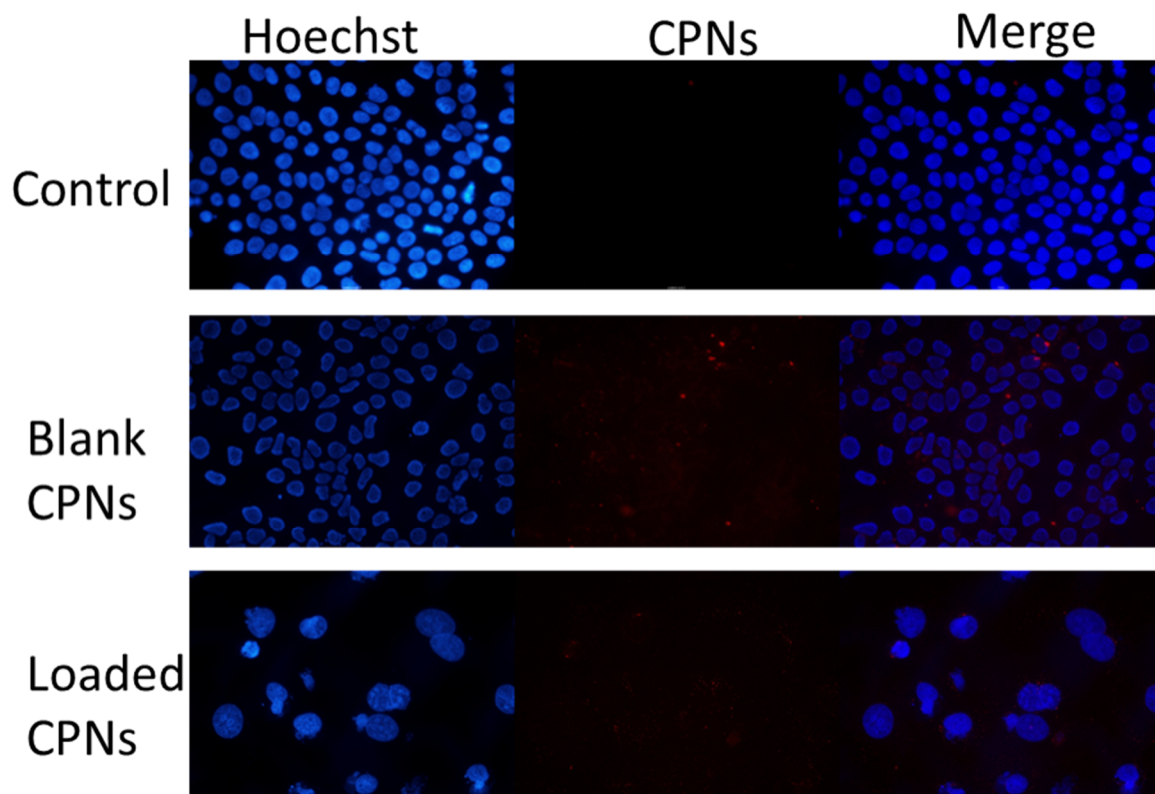


Figure 29: Fluorescent microscopy images of Huh7 cells incubated with blank and CPT loaded PBT-(Ac) nanoparticles.

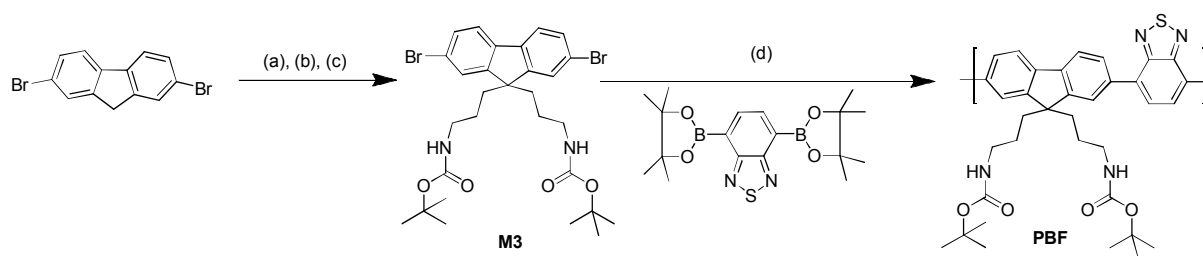
In order to visualize CPNs interaction with human cells, huh7 cells were incubated with blank and CPT loaded CPNs and their nuclei were stained with blue Hoechst dye after being fixed with methanol. Their fluorescence microscopy images can be seen in Figure 29 where PBT-(Ac) nanoparticles are easily visible with the red filter of the microscope which is denoted as CPNs channel. No signal is detected from this channel with control cells which were not treated with CPNs. This confirms that the signals obtained from this channel in the other images are coming from the nanoparticles. Blank nanoparticles are observed to be localized around cell nuclei and cells appear to be in good condition. CPT loaded CPNs are also observed around cell nuclei but the cell population was much scarcer in this case and the nuclei shapes are distorted which is a sign of intracellular CPT activity.

2.2.2 Synthesis and Characterization of Green Emitting pH Sensitive Polymer Nanoparticles

Green emitting, pH sensitive polymer poly{3-[9-(3-tert-Butoxycarbonylamino-propyl)-3-methyl-6-(7-methyl-4,7-dihydro-benzo[1,2,5]thiadiazol-4-yl)-9H-fluoren-9-yl]-propyl}-carbamic acid tert-butyl ester (PBF) was synthesized and characterized followed by preparation of nanoparticles from this polymer. Blank and drug loaded nanoparticles are characterized by different spectroscopy and microscopy techniques and some in vitro tests were performed to estimate their biological activity. Polymer synthesis and nanoparticle synthesis are given separately in following two subsections of this section.

2.2.2.1 PBF Synthesis and Characterization

PBF was synthesized according to reaction Scheme 2. First 9th position of 2,7-dibromofluorene was functionalized with bromopropyl groups and through a substitution reaction bromide groups were converted into azide groups. To synthesize monomer 3, first azide groups were reduced to amine through Staudinger reaction and subsequently amine groups were protected with tert-butoxycarbonate (t-boc). PBF was synthesized in 78% yield by Suzuki Coupling of Monomer 3 and 1,2,3-benzothiadiazole-4,7-bis (boronic acid pinacol ester).



Scheme 2: Synthetic scheme for PBF. (a) 1,3-dibromopropane, DMSO, NaOH (50%, w/w), 25° C, 2h, 75%; (b) NaN₃, DMSO, 12h, 94%; (c) (i) PPh₃, THF/H₂O (6:1, v/v), 12h, (ii) di-tert-butylbicarbonate, THF, 4h, 88%; (d) Pd(PPh₃)₄, DMF, 80 ° C, 20 h, 78%.

Brownish yellow reaction mixture turned to bright green after 24 hours indicating the formation of green emitting polymer. After the reaction is completed, the product was washed with water and methanol to get rid of catalyst and unreacted monomer residues. Washing with methanol also purifies the product from boronic ester side product residues of coupling reaction. After

these purification steps PBF was obtained as a bright yellow powder with a yield of 78%. Resulting polymer structure was characterized by $^1\text{H-NMR}$ as seen in Figure 30 where there is a great deal of overlapping between peaks especially between 1 and 2ppm. This due to very close chemical shifts of protons denoted as *b*, *c* and *d*. On the other hand a very intense peak is expected to come from the proton *b* since there is 18 of them for every repeating unit. This intense peak can be distinguished among other peaks in 1-2ppm region for having exactly the expected integration value which is 9 times the integration of proton *a*. Aromatic protons are also visible around 8ppm in the aromatic region.

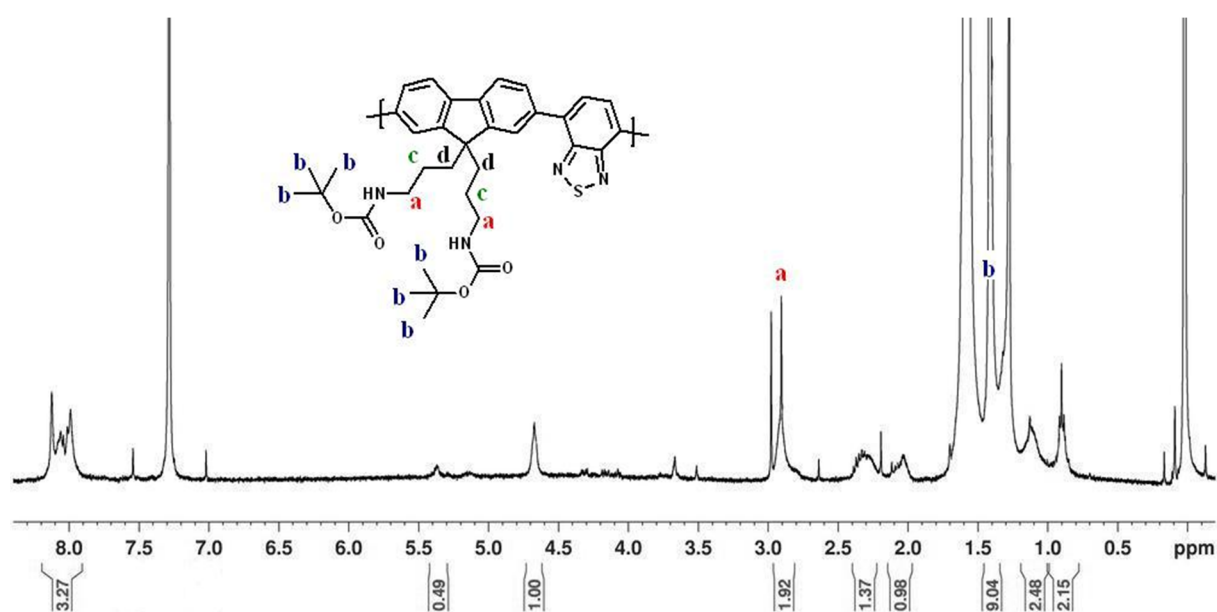


Figure 30: $^1\text{H-NMR}$ (400 MHz, 25 °C, CDCl_3) spectrum of PBF.

Elemental analysis is used to further confirm the suggested structure. The results are exceptionally close to theoretical values, especially for a polymer, confirming the suggested structure of PBF.

Thermal properties were characterized by DSC and TGA measurements. TGA graph of PBF is shown in Figure 31 where weight loss starts just above 100 °C and continues rapidly until it comes to a breaking point at 279 °C. The weight loss percentage at this point is equal to the weight percentage of protecting t-BOC groups which are shown in red in the structure. After the first breaking point another breaking point is reached at 423 °C. At this point 51.4% of the weight is lost which is exactly equal to the weight percentage of pendant groups

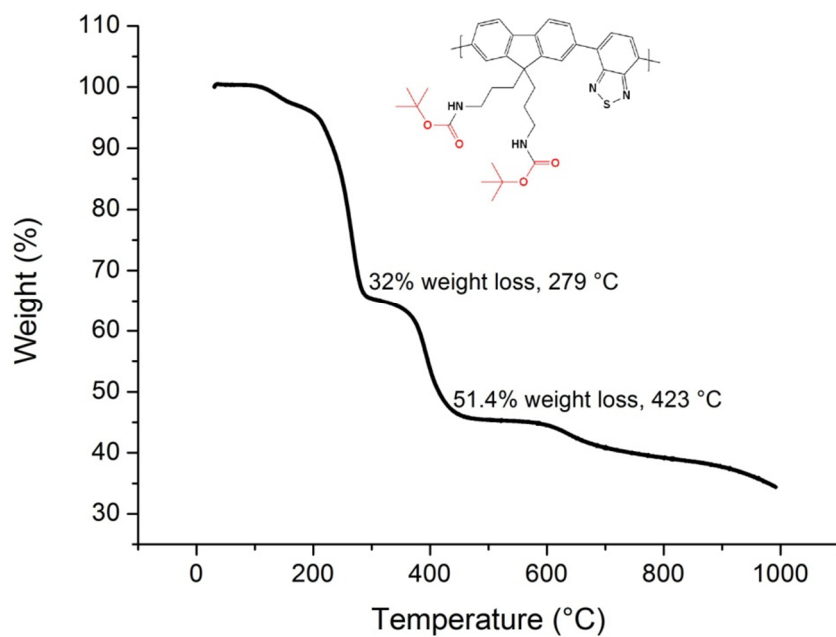


Figure 31: TGA graph of PBF.

DSC graph of PBF can be seen in Figure 32. No melting event was observed for this polymer since there are no endothermic dips in the graph but there is a rather linear endothermic slope which is attributed to glass transition. Tg value was calculated to be 92.5 °C from this slope. The endothermic dip above 250 °C cannot be attributed to melting since TGA results show that decomposition starts just above 100°C.

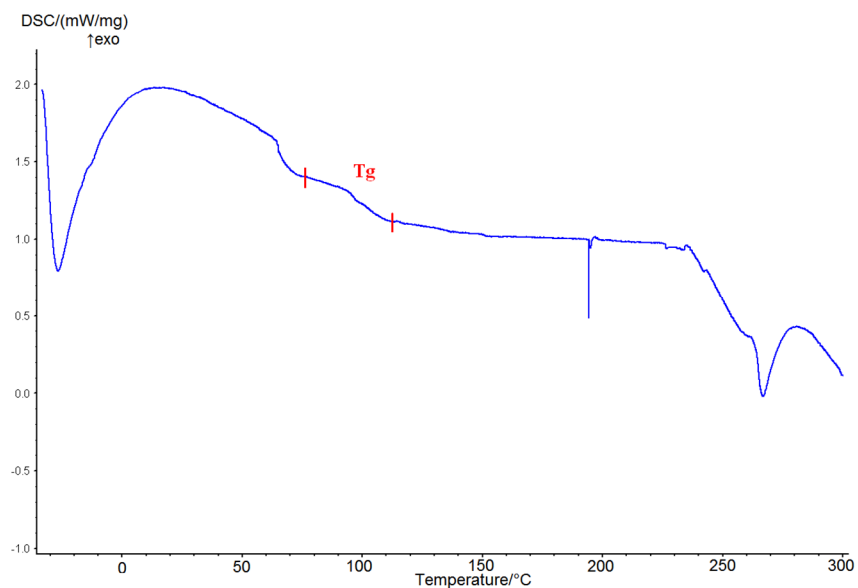


Figure 32: DSC graph of PBF.

FTIR spectrum of this polymer before and after acid treatment was also successfully taken to confirm deprotection of amine groups at low pH levels. Anhydrous trifluoroacetic acid was added to the polymer solution in chloroform to deprotect the polymer and carbonyl stretching at 1700 cm^{-1} disappeared from the FTIR spectrum as seen in Figure 33 confirming leaving of protecting groups.

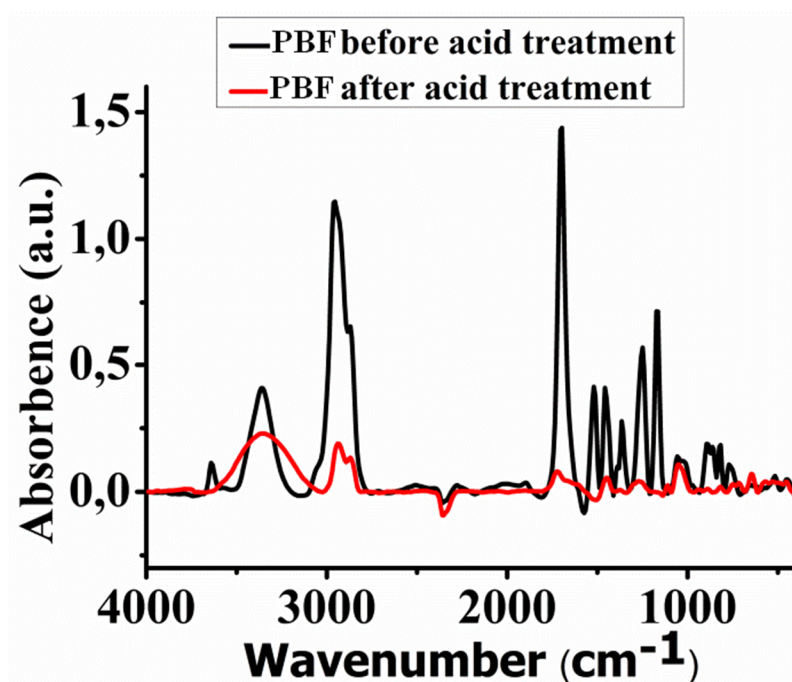


Figure 33: FTIR spectra of PBF before and after acid treatment.

Optical properties of PBF were investigated by UV-Vis and fluorescence emission spectroscopy. Figure 34 shows absorbance and PL emission of PBF solutions in different solvents where PBF is observed to have an emission maximum of 538 nm in THF. A slight bathochromic shift is observed as the solvent polarity increases.

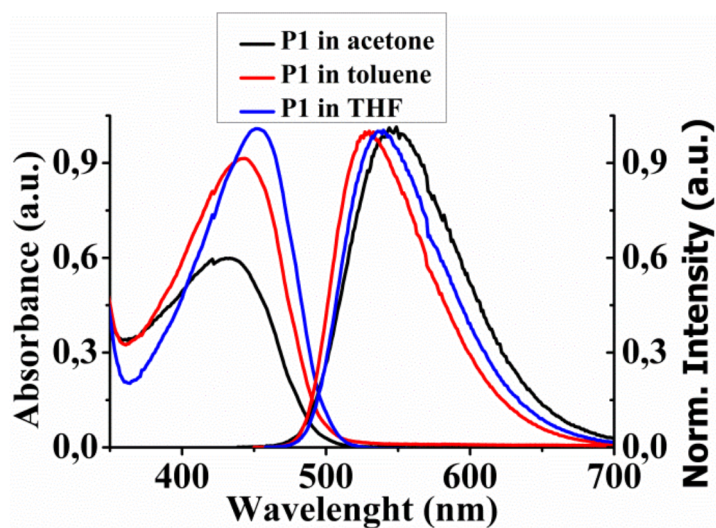


Figure 34: UV-Vis absorption and PL emission spectra of PBF in different solvents.

2.2.2.2 Nanoparticle Synthesis, Characterization and In Vitro Tests

Nanoparticles of PBF were prepared by nanoprecipitation technique as mentioned in the experimental section. Namely, different amounts of PBF were dissolved in 1 ml THF and this solution was injected into 20 ml water while the water is being sonicated. This resulted in clear green emitting aqueous nanoparticle dispersions with several nm red shifted emission compared to polymer solutions as seen in the absorbance-emission spectrum in Figure 35. This is attributed to strong π - π interactions between polymer chains and high polarity of aqueous environment.

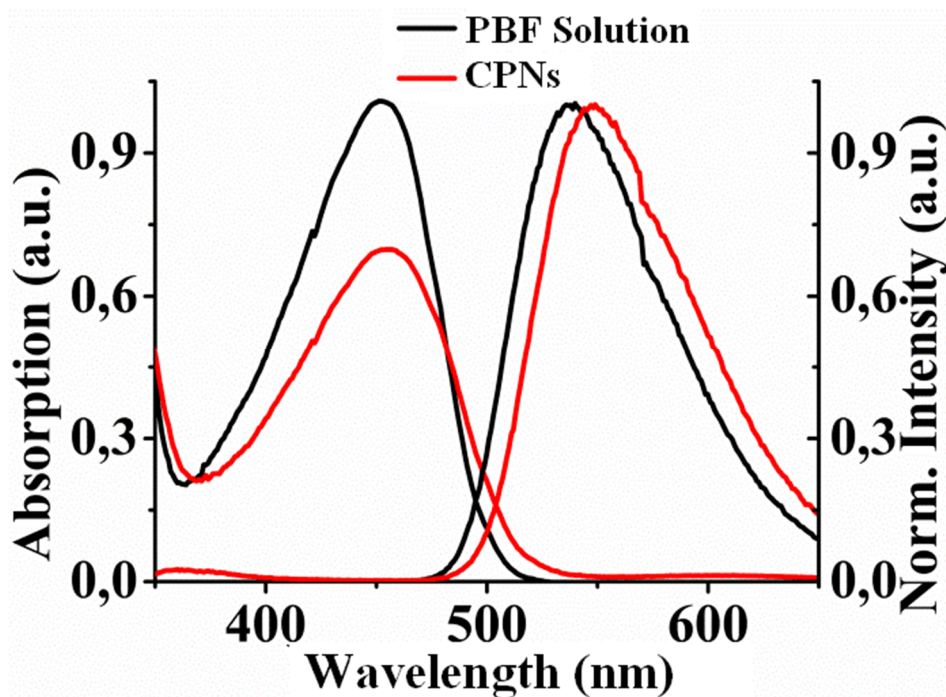


Figure 35: UV-Vis absorption and PL emission spectra of PBF in solution and as aqueous CPNs.

Nanoparticle sizes were measured by DLS method and confirmed by SEM images. Nanoparticle diameter was tunable by changing the polymer concentration in the solution. Polymer solutions with higher concentrations resulted in larger nanoparticles as seen in Figure 36 showing that versatile nature of nanoprecipitation process allows tuning of particle size and distribution. When 1 mg/ml solution of PBF was used, Z-average diameter of particles exceeded 90 nm while using half of this concentration decreased the diameter to around 87nm. All batches resulted in a zeta potential value between -30 and -40 mV regardless of average diameter which shows relatively polar carbonyl groups of pendants are facing out of the surface of CPNs.

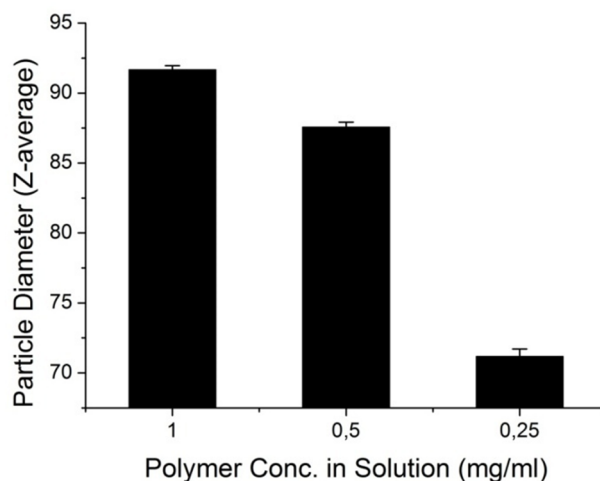


Figure 36: Different Z-average sizes obtained with different PBF concentrations.

Diameter of nanoparticles used for further experiments were tuned to be between 70 and 75 nanometer by using a PBF concentration of 0.25 mg/ml to be able to utilize EPR effect according to literature. (6) Scanning electron microscopy was used to visualize the CNP shapes and confirm their sizes. They revealed spherical particles with a narrow size distribution free of large aggregates as seen in Figure 37. Measured CPN sizes also comply with DLS measurement results.

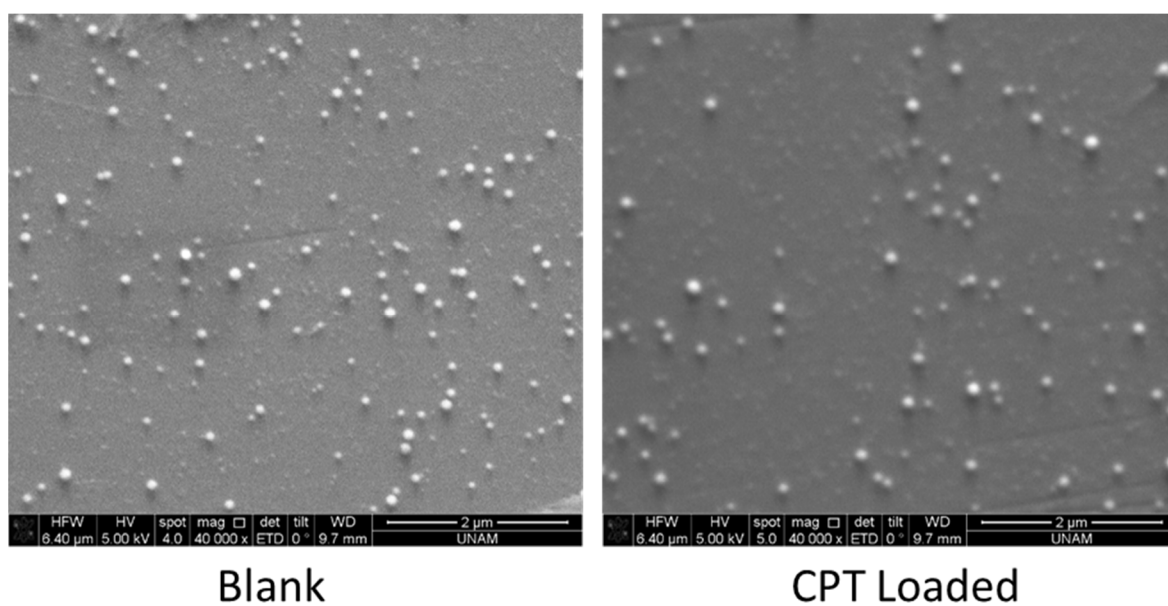


Figure 37: SEM micrographs of PBF nanoparticles.

Dispersions that were kept at room temperature remained clear and free of aggregates for a very long time and their sizes measured with DLS did not vary significantly ten days after their preparation which indicates a good aqueous stability and a long shelving life. The results of this experiment are displayed in Figure 38.

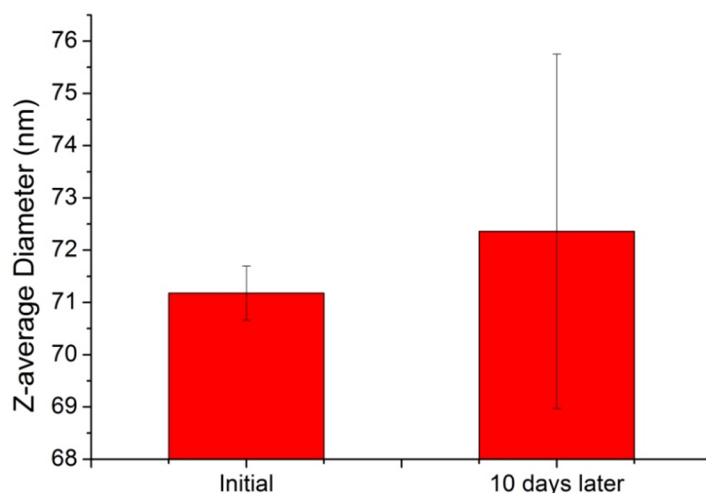


Figure 38: Stability of PBF nanoparticles in water over time.

Next experiment investigated pH responsiveness of PBF CPNs by using DLS and zeta potential measurements during a pH titration. According to our hypothesis, a low level of pH should cause hydrolysis of t-BOC groups exposing highly hydrophilic charged amine groups leading to swelling and ultimately complete disintegration of CPNs. When titration was started, zeta potential of CPNs immediately started to increase as seen in Figure 39, indicating hydrolysis starts right away when pH drops. When the pH value reaches 6, a significant increase in average diameter is observed and zeta potential reading reaches half of its original value. The increase in size and zeta potential continues until pH reading drops just below 5 where CPNs reach a size of 750nm and surface potential becomes completely neutral. There are enough charged amines on CPN surfaces to neutralize the net surface charge at this point where they reach their maximum size. Below this pH value CPNs start to disintegrate as polymer chains begin leaving CPN surfaces and get dissolved in water as shown by the decrease in their size. This is a positive indicator for our hypothesis since CPT molecules trapped inside CPNs will be able to leave easily under these conditions.

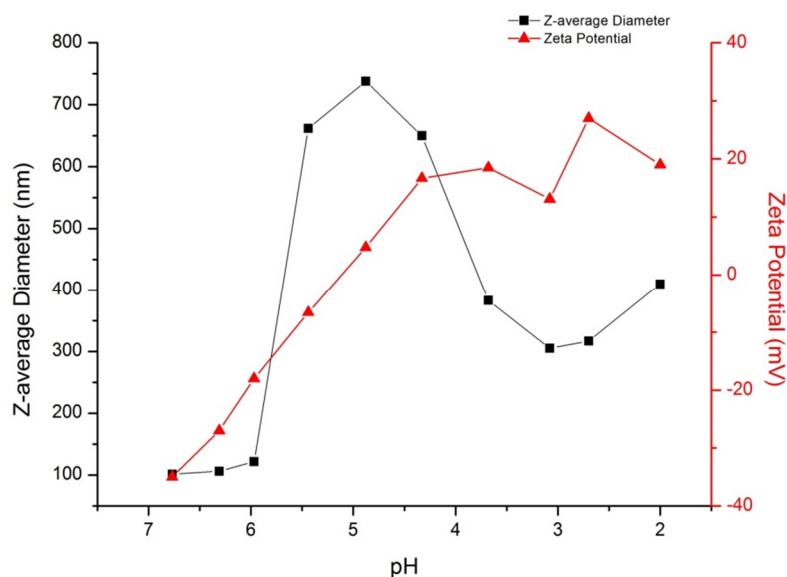


Figure 39: Zeta potentials and sizes of PBF nanoparticles at different pH values.

After confirming that obtained CPNs have a decent size and shape quality, high stability and are responsive to stimuli, we next studied their drug loading capacities. Their loading efficiency and entrapment rate was studied in the same way PBT-(Ac) CPNs were studied and results are displayed in Figure 40. The most striking difference observed between PBF and PBT-(Ac) is that PBF is able to carry much higher amounts of CPT. This is attributed to higher number of π bonds in each repeating unit of PBF which mediates much stronger π - π interactions between highly conjugated CPT molecules and polymer backbone. Interestingly, when a small amount of CPT is used, like 1/25 of the weight of PBF, 100% of CPT molecules are trapped inside CPNs. This gives a 100% drug entrapment efficiency at 1/25 drug/polymer ratio and eliminates the need to purify CPNs from excess free drug molecules. More CPT can be loaded into CPNs to increase loading efficiency by increasing the amount of drug added to the solution forcing more drug molecules into CPNs. Drug loading efficiency could be increased up to 50% by using CPT twice the weight of PBF. Using higher amounts of CPT caused cloudy CPN dispersions due to aggregation of excess CPT molecules. 1/25 CPT/PBF ratio was used for the experiments with CPT loaded CPNs.

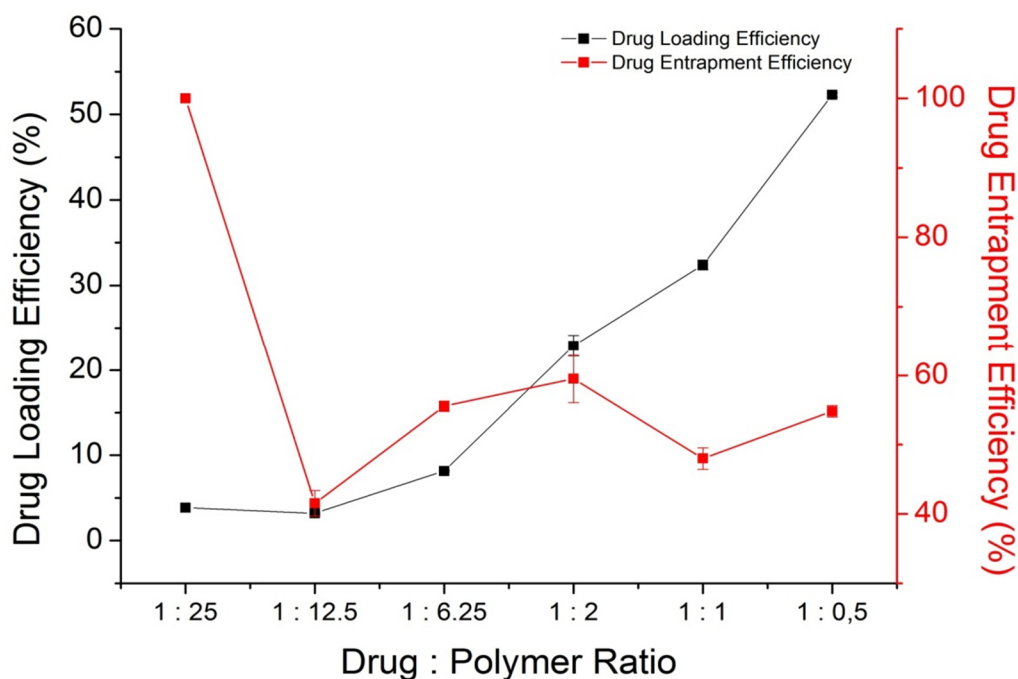


Figure 40: Drug loading and entrapment efficiency values of PBF nanoparticles for different drug:polymer ratios.

pH dependent drug release profile is studied by loading CPT loaded CPNs into dialysis tubes and adding either PBS (pH 7.4) or acetate (pH 5) buffer onto them. These tubes were then immersed into 100 ml of buffers added onto them. 0.2 % (vol/vol) tween 20 was added into release mediums to solubilize released CPT molecules. Samples were taken from these buffers at different time intervals and concentration of free CPT was calculated from UV-Vis measurements of these samples and the calibration curve built from UV-Vis measurements of CPT solutions with known concentrations. Release medium was changed with fresh buffer at certain time intervals. As seen in Figure 41, less than 40% of loaded CPT was released in around 10 hours at physiological pH level of 7,4. No more drug release was observed after this point at physiological pH levels. This is probably due to diffusion of CPT molecules that are close to CPN surfaces along concentration gradient into aqueous medium while CPT molecules that are buried deep inside CPN matrices are unable to diffuse out. Release profile at acidic pH of tumor microenvironments and endosomes is much quicker where more than 80% of the loaded CPT is released within the first 24 hours. Drug release continues slowly after this point for 40 more hours until almost all of the loaded CPT is released. This result confirms our

hypothesis of stimuli-triggered rapid drug release since drug release is shown to be much faster at low pH under near-physiological conditions.

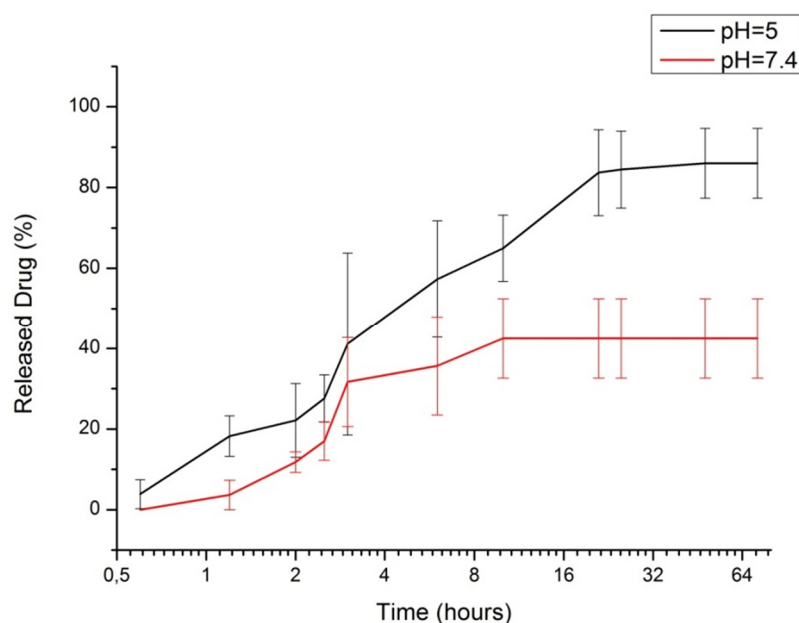


Figure 41: Release profile of PBF nanoparticles at two different pH values.

Next cytotoxicity of blank and CPT loaded CPNs was tested by using a human hepatocarcinoma cell line huh7 to investigate intrinsic cytotoxicity of blank CPNs and observe the activity of CPT loaded into CPNs. A real time electronic cell sensing (RT-CES) assay was used to monitor their cytotoxic activity over time as mentioned in previous sections. Two different CPT loading rates were used for both blank and loaded CPNs. CPNs denoted with the letter (A) carry one weight unit of CPT for every 25 weight units of polymer whereas CPNs denoted with the letter (B) carry the higher CPT : polymer ratio of 1: 12.3. It was decided to test two different loading rates in order to see the effect of drug loading on the efficiency of the drug. CPNs denoted with (A) were the lowest CPT concentration tried in the loading experiments where there is no need for purification while (B) were the ones which gave the maximum drug encapsulation efficiency with high drug amounts. The results are demonstrated in Figure 42.

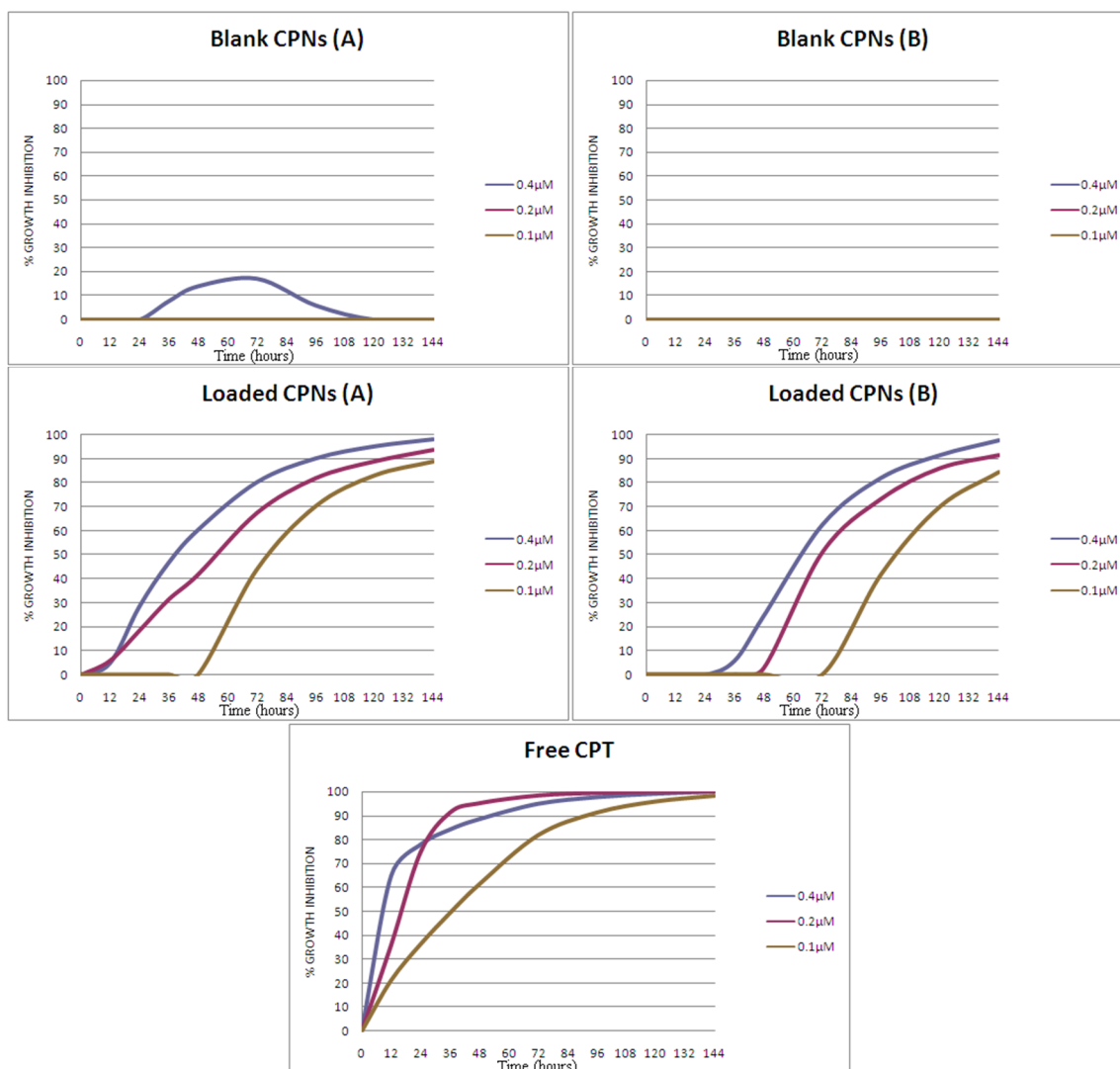


Figure 42: RT-Ces results of CPT loaded and blank PBF nanoparticles.

The results are highly similar to cytotoxic profiles of PBT-(Ac) nanoparticles. Blank nanoparticles of (A) at the highest concentration appear to cause some changes in the cell behavior after 24 h incubation, growth inhibition reach to a plateau value of 18%, for the nanoparticle concentration of 0.4 μM at 74 hrs and then the inhibition rate decreases rapidly and the cells starts to be responsive again and proliferate. This behavior may suggest the complex, dynamic nature of the interaction between the cells and nanoparticles. This could also be explained by an incidental enzyme interaction in which the NPs could randomly bind on some proteins to inhibit their activities, however, the cell signaling pathways get involved at this stage by increasing the expression of proteins to compensate the initial inhibition. As a result, this will cause no serious harm to the cells to go to apoptosis but only a temporary

inhibition in the cell growth process. This effect is not observed in the loading rate (B) since it needs very little amount of CPNs to apply the needed dose of CPT thus there are much fewer nanoparticles that can interfere with cellular processes.

In both loading rates, the growth inhibition is slower than free CPT confirming the slow release feature of the nanoparticles supported by in vitro drug release studies in different pH values. The release is even slower in the case of the nanoparticles having high drug loading contents. This result can be attributed to strong interactions between CPT molecules and polymer chains because CPT molecules can interact with each other more freely due to presence of fewer polymer chains to interfere with this process. In lower loading rates, CPT molecules can be evenly distributed in the polymer matrix; not unlike dissolution. Upon cell internalization, these matrices interact with hydrophobic membrane structures and CPT molecules can easily diffuse into these membranes to show activity in the cell. However, higher CPT content can bring out the intrinsic solubility problem of hydrophobic drugs. CPT molecules can easily form highly stable aggregates via π - π stacking inside the sparsely packed matrix and their likelihood of interacting with cellular hydrophobic compartments drops drastically. Therefore they show little to no cellular activity for a long time after cell internalization. These results show that PBF nanoparticles carry the desirable biological activities that are shown in PBT-(Ac) nanoparticles.

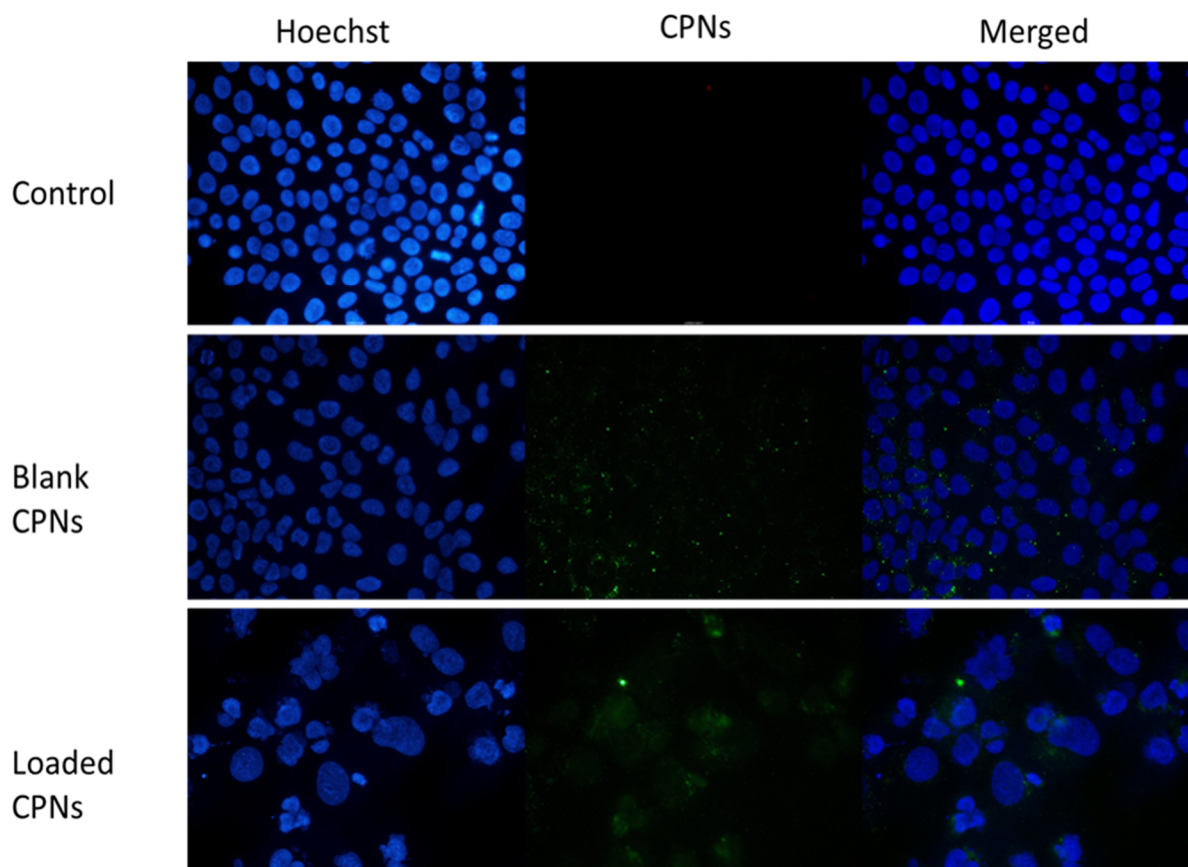


Figure 43: Fluorescence microscopy images of Huh7 cells incubated with blank and CPT loaded PBF nanoparticles.

The interactions of PBF nanoparticles with Huh7 cells were visualized with fluorescent microscopy in the same way PBT-(Ac) nanoparticles were visualized. The results were also quite similar to previous study where PBF nanoparticles are located around cell nuclei in blank and CPT loaded CPNs as demonstrated in Figure 43. The cells incubated with loaded CPNs showed a scarce population due to growth inhibition of released CPT.

2.3 Synthesis and Characterization of Red Emitting Redox Sensitive Polymer Nanoparticles

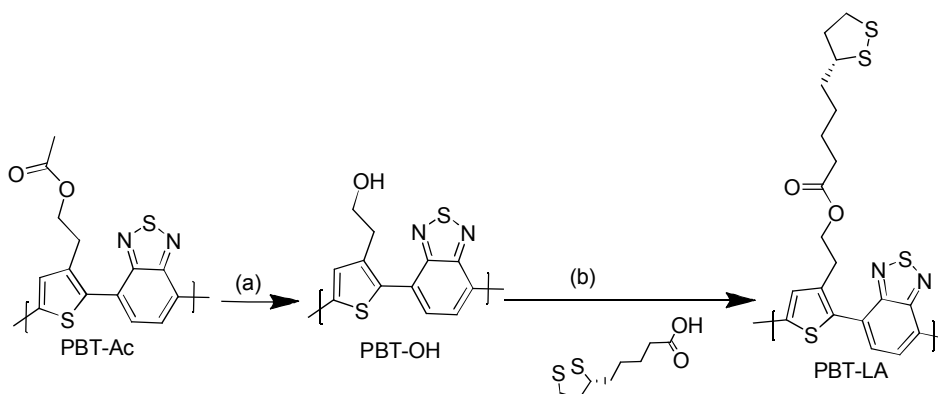
A well-known property of tumor cells that differentiate them from healthy cells is that they have an elevated redox potential. This property comes from excessive synthesis of glutathione (GSH) in cancer cells and gives some cancers resistance against certain chemotherapy drugs. GSH molecules have a thiol group that can cleave any disulfide bonds through thiol-disulfide exchange reactions. Abundance of GSH in tumors can be exploited to passively target cancer

cells. (54) We designed redox sensitive CPNs by attaching lipoic acid groups to side chains of a conjugated polymer. After preparation of nanoparticles, disulfide groups of some of the lipoic acid groups are cleaved to thiols by using a limited amount of a strong reducing agent. This starts a chain of disulfide-thiol exchange reactions between lipoic acids within the nanoparticles, resulting in disulfide cross-linked nanoparticles. These disulfide bonds are expected to be broken by GSH in tumor cells leading to disruption of CPNs and faster drug release at tumor sites.

Red emitting, redox sensitive (R)-2-(2-(benzo[c][1,2,5]thiadiazol-4-yl)thiophen-3-yl)ethyl 5-(1,2-dithiolan-3-yl)pentanoate (PBT-LA) was synthesized and characterized followed by preparation of nanoparticles from this polymer. Blank and drug loaded nanoparticles are characterized by different spectroscopy and microscopy techniques and some in vitro tests were performed to estimate their biological activity. Polymer synthesis and nanoparticle synthesis are given separately in following two subsections of this section.

2.3.1 PBT-LA Synthesis and Characterization

Polymer for redox sensitive CPNs was synthesized according to Scheme 3 starting from the acetoxy protected PBT-(Ac) polymer.



Scheme 3: Synthetic scheme for PBT-LA. (a) NaOH, DMF/H₂O (10:1, v/v), 25 °C, 18h, 98%;
(b) EDC, DMAP, DMF, 25 °C, 48h, 99%

Hydroxyl groups were deprotected in a basic environment. Simply, the polymer was dissolved in DMF and a molar excess amount of NaOH was dissolved in water and added. The mixture was stirred overnight and resulting polymer was washed with excess amount of water after evaporating all the solvent. Deprotection immediately changed the solubility of the polymer,

making it insoluble in chloroform and THF indicating a change in the chemical composition of the polymer. Also the carbonyl peak at 1750 cm^{-1} in the FTIR spectrum disappeared as seen in the Figure 44, confirming the leaving of acetyl groups.

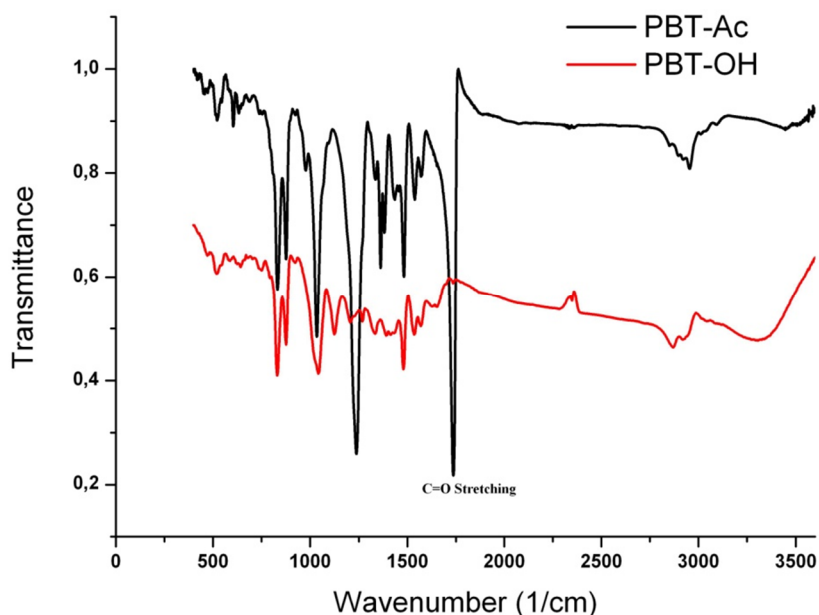


Figure 44: FTIR Spectra of PBT-(Ac) and PBT-OH.

Exposed hydroxyl groups were then used for EDC coupling with lipoic acid. The procedure involved dissolving PBT-OH in DMF and adding DMAP, EDC and lipoic acid respectively. Mixture was stirred at room temperature for 48 hours and the resulting polymer was washed vigorously with water. Attaching lipoic acid groups on the chains rendered the polymer hydrophobic enough to efficiently obtain high quality nanoparticles as amphiphilic polymers tend to result in larger nanoparticles with poor polydispersities. It also changed the solubility back to its original state where it's highly soluble in solvents like chloroform and THF.

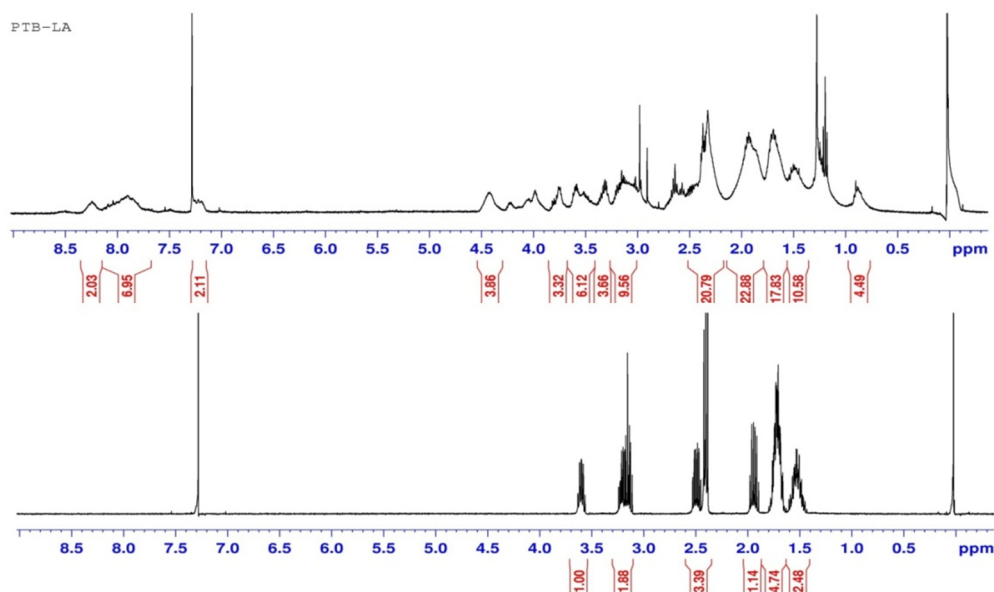


Figure 45: ¹H-NMR (400 MHz, 25 °C, CDCl₃) spectra of PBT-LA (top) and Lipoic Acid (bottom).

Resulting polymer was firstly characterized by ¹H-NMR spectroscopy. ¹H-NMR spectrum of PBT-LA was compared with the ¹H-NMR spectrum of lipoic acid and PBT-(Ac). Broad peaks that belong to the polymer are still observable. The Figure 45 shows ¹H-NMR spectra of PBT-LA and lipoic acid together and it is clearly visible that there are additional peaks that are perfectly aligned with lipoic acid peaks showing the presence of lipoic acid molecules. Since lipoic acid is highly water soluble and the polymer is washed vigorously with water during the purification process, these chemical shifts can only be from lipoic acid molecules that are covalently attached to polymer chains.

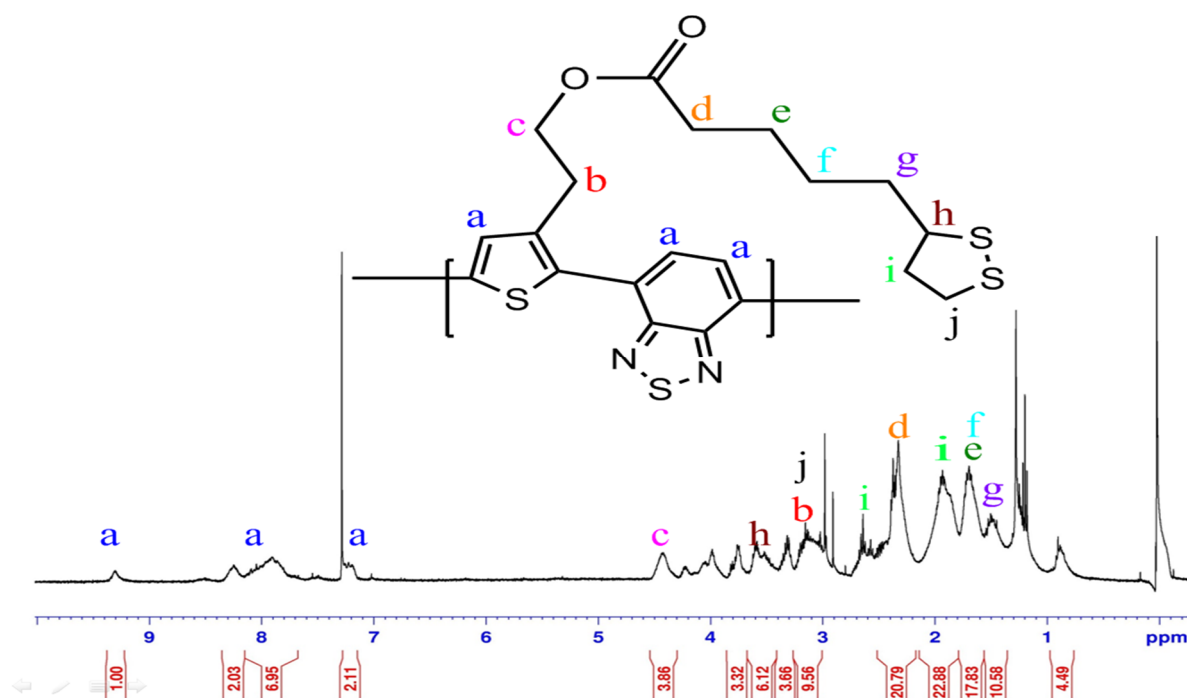


Figure 46: $^1\text{H-NMR}$ (400 MHz, 25 °C, CDCl_3) spectrum of PBT-LA.

The chemical shifts are assigned to corresponding protons in the Figure 46 according to theoretical shifts but it was impossible to differentiate between the integrations of different peaks due to heavy overlapping. Moreover there are extra peaks that can't be assigned to anything. Moreover, the spectrum is too crowded with chemical shifts that are too close together which makes it difficult to assign protons from the structure to distinct peaks. This can be attributed to atacticity of the polymer, where pendant groups are facing random directions, creating differently shielded protons thus giving multiple peaks for one type of proton. This is why additional techniques were used to confirm the suggested structure of the polymer. Elemental analysis results of PBT-LA gave values extraordinarily close to theoretical values for nitrogen, carbon and hydrogen. The deviation from the theoretical value of sulfur is rather large but the elemental analysis device we used is known to give unreliable results for sulfur in other experiments as well so this deviation can be disregarded. This experiment is another sign of polymer having the suggested structure.

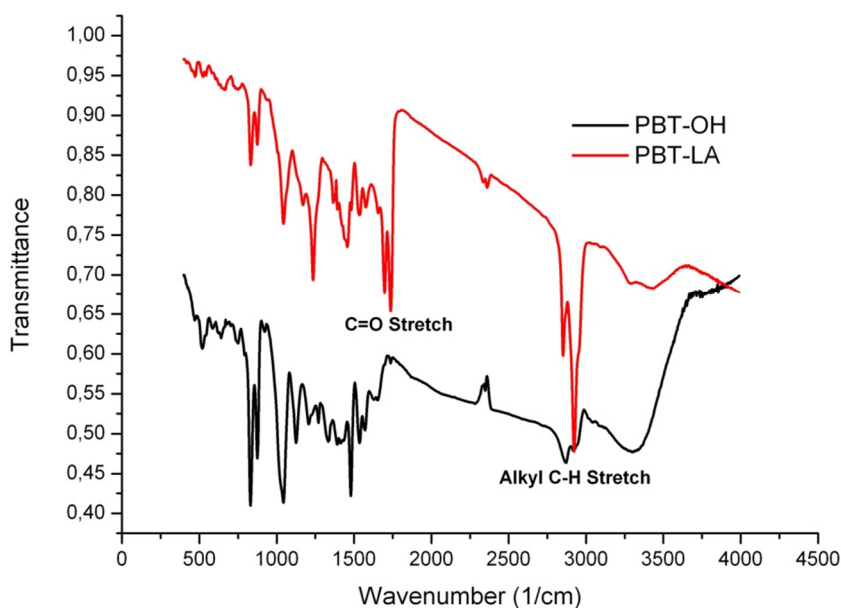


Figure 47: FTIR spectra of PBT-LA and PBT-OH.

FTIR spectrum of PBT-LA was compared with the FTIR spectrum of PBT-OH in order to observe the changes in the IR absorbance after DCC coupling of lipoic acid. The most striking difference is the absorbance of carbonyl groups at 1750 cm^{-1} in PBT-LA spectrum which is absent in PBT-OH spectrum. This is the primary proof that esterification occurred between the -OH groups of PBT-OH and carboxylic acid groups of lipoic acid since C=O stretch at 1750 cm^{-1} is the strongest fingerprint absorption in the FTIR spectrum of lipoic acid. The second strongest absorption of lipoic acid is the alkyl C-H stretch just under 3000 cm^{-1} . It can be seen that alkyl C-H stretching due to the two carbons in the pendant of PBT-OH is rather weak but after the coupling of lipoic acid absorbance of this stretching becomes much stronger. This is attributed to addition of seven more alkyl carbons to the structure. Moreover, samples for both spectra are very well dried but it can be seen that O-H stretching above 3000 cm^{-1} is extremely strong in PBT-OH due to -OH groups but this absorbance dwindles after esterification of the -OH group. Remaining weak absorbance in this region is likely from the humidity remaining in the sample and air.

Optical properties of PBT-LA in solution was characterized by UV-Vis and fluorescence emission spectroscopy and found to be identical to PBT-(Ac).

Next method was injecting the polymer solution into aqueous poloxamer solution which gave a decent PDI value of 0.12 and a single sharp peak in DLS measurements as seen in Figure 50. This method was used in the final form of nanoprecipitation process. When zeta potentials of CPNs were measured, there was a significant difference between bare and poloxamer coated CPNs. Bare CPNs showed a positive surface potential of $10,26 \pm 0,41$ while poloxamer coated CPNs showed an almost neutral surface potential of $3,4 \text{ mV} \pm 0,54$ which indicates the presence of shielding PEG chains on the surface of CPNs.

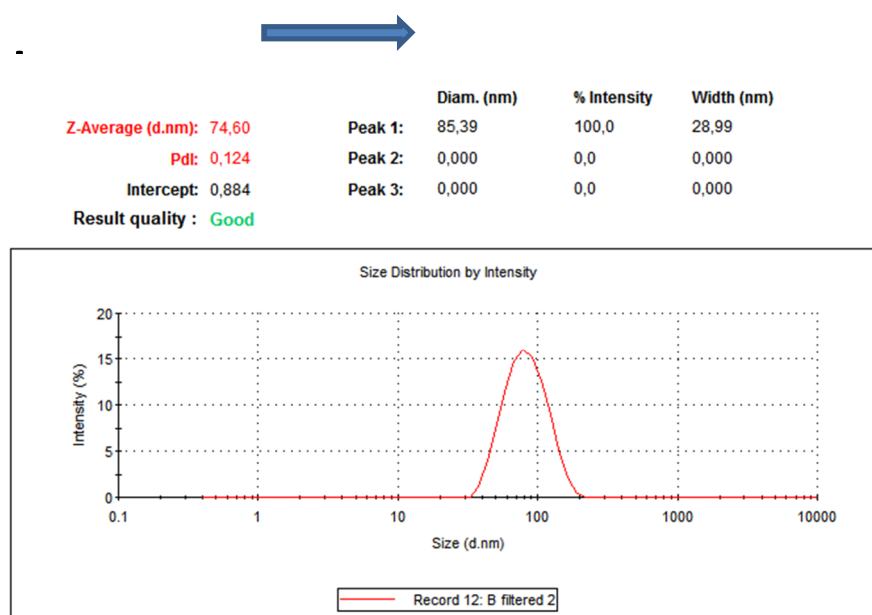


Figure 50: DLS measurement of PBT-LA nanoparticles formed by dissolving surfactant in water.

To optimize CPN diameter, pluronic F-127 was dissolved in distilled water to obtain a concentration high enough for adsorption onto CPNs as determined in the literature. [] Then PBT-LA solutions in THF with different concentrations were injected into these poloxamer solutions. After evaporating THF under nitrogen environment to harden the CPNs, dithiothreitol (DTT) was added into CPN dispersions. The amount of DTT was adjusted to be just enough for reducing 10% of lipoic acid moieties in the CPN structures. After disulfide bond exchange reactions between reduced and oxidized forms of lipoic acid groups throughout

each nanoparticle, cross-linked CPNs were obtained. Cross-linking affected CPN size distributions. DLS size measurement results before and after cross-linking can be seen in the Figure 51.

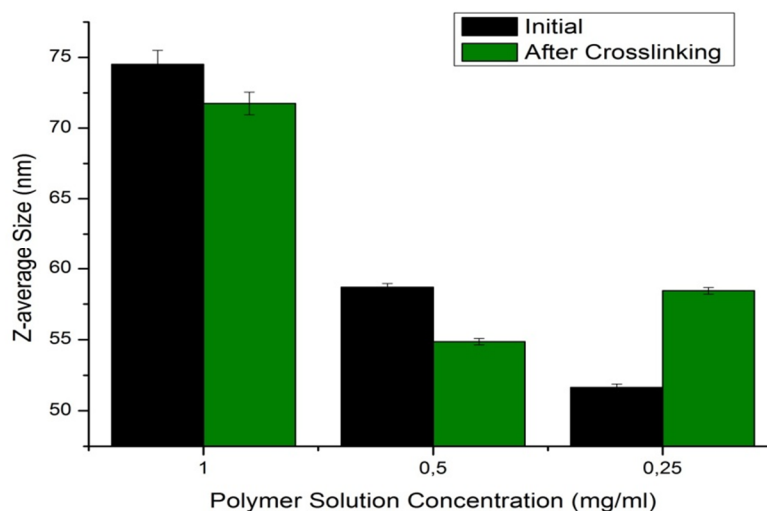


Figure 51: Initial and cross-linked sizes of PBT-LA nanoparticles prepared with different polymer concentrations.

It can be clearly observed that CPN sizes increase with the concentration of PBT-LA in the initial solution. After cross-linking, average sizes of the larger CPN batches shrink due to covalent disulfide bonds formed between the chains within the nanoparticles bringing them closer to each other. In the batch with the smallest size distribution, due to increased surface area of the small nanoparticles, enhanced surface interactions between CPNs cause covalent bonding between nanoparticles leading to an increase in the average size. The batch prepared with 0.5 mg/ml PTB-LA concentration in the initial solution was selected which gave 57 nm average diameter that decreases to about 55 nm after cross-linking. This was the smallest average diameter obtainable without causing CPNs to cross-link onto each other.

The drop in Z-average diameter is a good sign towards confirming cross-linking of the CPNs. To further prove cross-linking and visualize the CPNs, SEM images were taken. It was seen that CPNs are spherical in aqueous environment and their diameters are consistent with DLS measurements. To use SEM images to prove cross-linking, we also evaporated water out of aqueous CPN dispersions and re-dispersed them in THF. Since polymer chains are soluble in

THF, non-cross-linked CPNs are expected to disintegrate and cross-linked ones are expected to stay intact. We could easily see intact nanoparticles in SEM images of cross-linked CPNs dispersed in THF while we could only see films of polymer in non-cross-linked ones. Furthermore SEM images showed the effect of poloxamer coating on the stability of CPNs. As can be seen in the Figure 52, poloxamer coated CPNs show individual spherical nanoparticles while bare CPNs show heavy aggregation induced during the drying process of the sample.

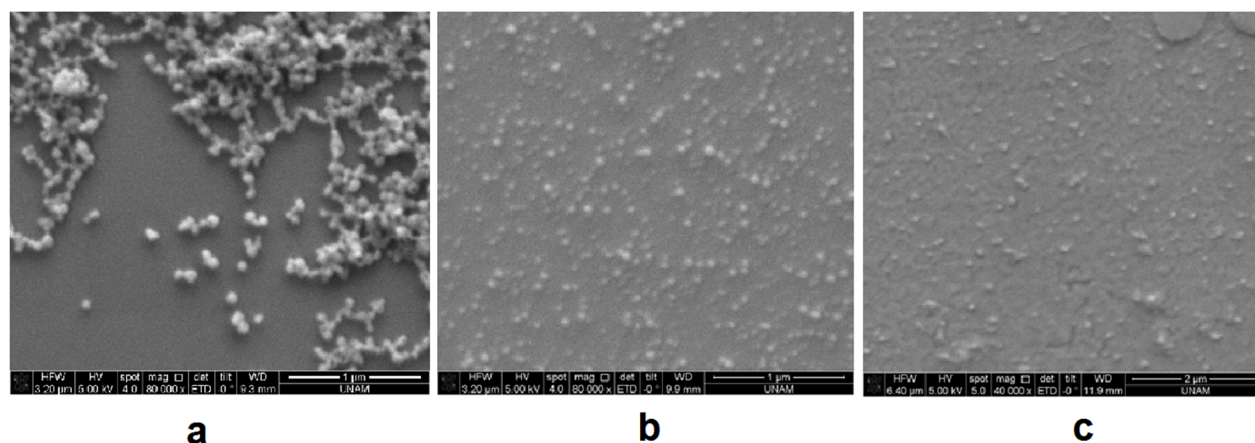


Figure 52: SEM micrographs of aqueous (a) bare and (b) poloxamer coated PBT-LA nanoparticles. Cross-linked nanoparticles dispersed in THF (c).

Another sign of cross-linking was the change in solubility of CPNs. When chloroform was added on aqueous dispersions of CPNs, non-crosslinked CPNs changed the color of chloroform indicating that some nanoparticles disintegrated by getting dissolved in chloroform layer. Crosslinked CPNs on the other hand stayed in the aqueous layer and did not give any color to chloroform as seen in Figure 53.

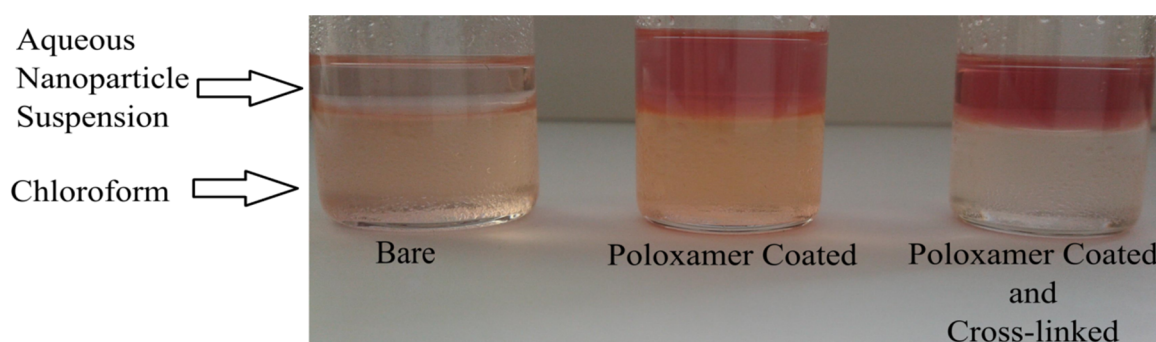


Figure 53: Bare, poloxamer coated and cross-linked PBT-LA dispersions with added chloroform layers.

The poloxamer coating formed by pluronic F127 adsorption onto CPN surfaces is confirmed by FTIR spectra. Poloxamer coated and cross-linked CPNs are prepared and loaded into dialysis tubes. These membranes are then immersed into an excess amount of distilled water and dialysis was allowed to continue for one week, refreshing the medium everyday. At the end of this process, water was evaporated from CPNs and obtained solid was analyzed with FTIR. This spectrum was then compared with FTIR spectra of bare CPNs and pluronic F-127. Poloxamer coated CPNs gave almost the same spectrum as the pluronic F-127 as seen in the Figure 54, indicating that a large amount of poloxamer chains are firmly attached to CPN surfaces because of hydrophobic effect.

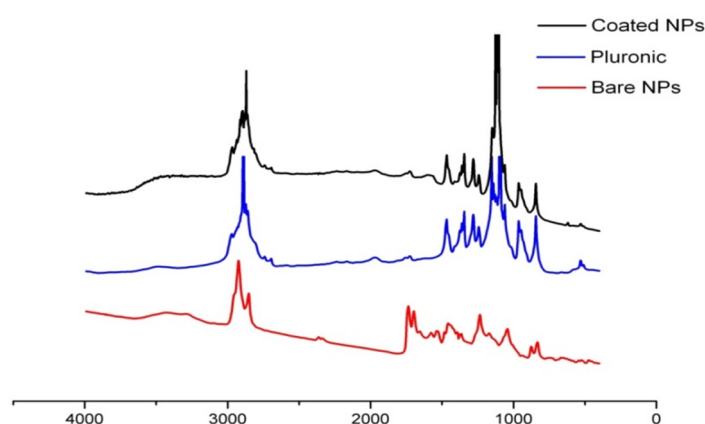


Figure 54: FTIR spectra of poloxamer, bare CPNs and poloxamer coated CPNs.

CPNs were also exceptionally stable at room temperature in different environments. Samples from cross-linked and coated CPNs were kept at room temperature in PBS buffer (pH 7.4) acetate buffer (pH 5) and water for a whole month and the size changes were monitored with DLS measurements. As seen in the Figure 55 there was no significant difference between initial size and the size after a month. Also there were no observable changes in the dispersions like aggregations or a color change despite they were not protected from ambient light.

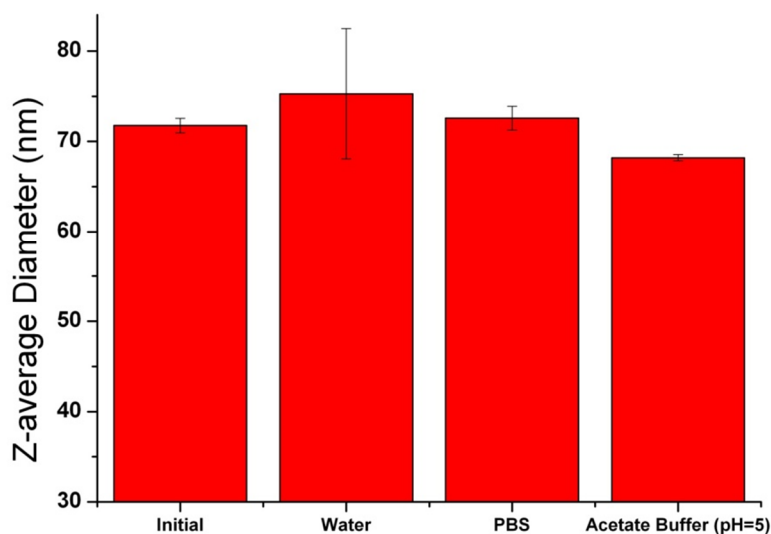


Figure 55: PBT-LA nanoparticle size differences after being kept 1 month in different media.

Optical properties of PBT-LA nanoparticles were very close to PBT-(Ac) nanoparticles but they showed miniscule differences in between bare and poloxamer coated CPNs. As seen in Figure 56, forming CPNs carried the emission of polymer well beyond 700 nm which is accepted as the beginning of NIR window. Poloxamer coated CPNs show a slight blue shift in the emission spectrum which can be disregarded.

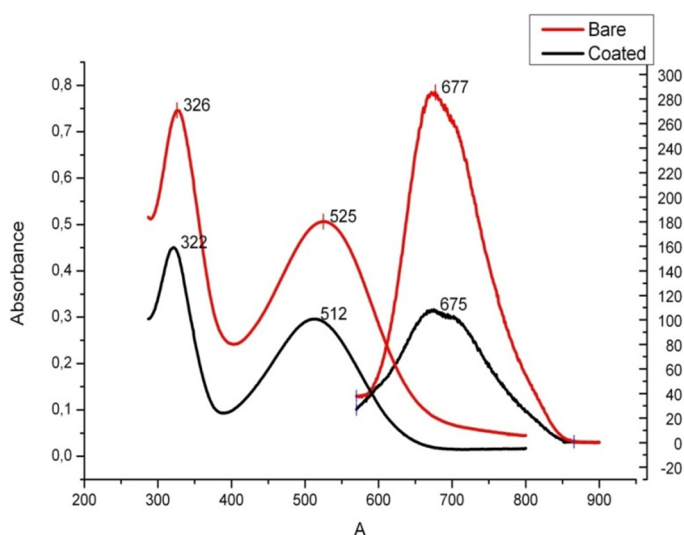


Figure 56: UV-Vis absorbance and PL emission spectra of bare and poloxamer coated PBT-LA nanoparticles.

Loading of anticancer drug CPT into CPNs was carried out by co-dissolving CPT with the polymer in THF prior to nanoprecipitation. Hydrophobic CPT molecules end up inside hydrophobic matrices of CPNs while they are forming inside the aqueous environment. The amount of CPT that ends up being encapsulated by the CPNs determines the drug entrapment efficiency and drug loading efficiency of the CPNs. In order to calculate these values, drug loading experiments were carried out. Different PBT-LA : CPT ratios were used while preparing CPT loaded CPNs and drug loading efficiency and drug entrapment efficiency values were calculated for each of these ratios to determine the optimum ratio for preparing CPT loaded CPNs. After each batch is prepared, CPT loaded CPNs were loaded into dialysis tubes and immersed into a certain volume of 0.2% (vol/vol) tween 20 solutions. Tween 20 solubilizes unencapsulated CPT molecules, causing them to diffuse through the dialysis membrane into the dialysate. This dialysate solution is then analyzed by UV-Vis spectroscopy method to determine the amount of free CPT molecules in it. Subtracting this amount from the amount of total CPT used in that batch gives the amount of CPT that is loaded inside the CPNs. The amount of CPT loaded in the CPNs is used to calculate drug loading efficiency and drug entrapment efficiency from the formula given in the previous sections. Drug loading and drug entrapment efficiencies obtained from different PBT-LA : CPT ratios were shown in the Figure 57. This experiment demonstrated that 2:1 PBT-LA : CPT (w/w) ratio results in the maximum amount of drug being loaded inside the CPNs.

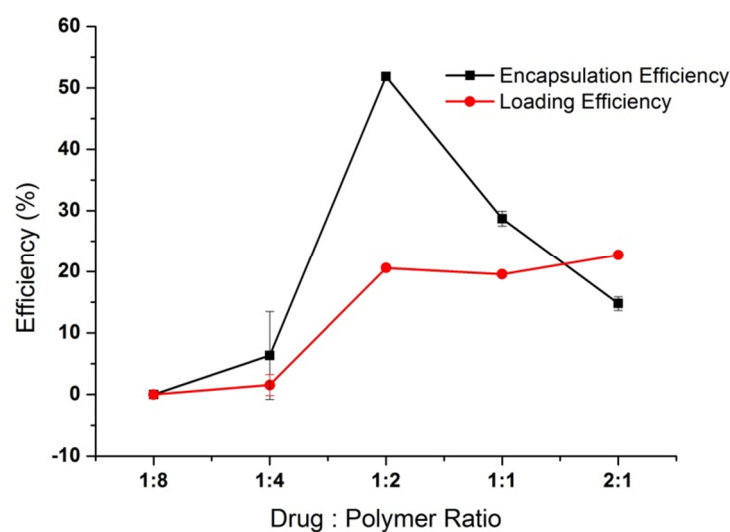


Figure 57: Drug loading and entrapment efficiency values of PBT-LA nanoparticles for different drug:polymer ratios.

After preparing the CPT loaded PBT-LA CPNs, the behavior they may demonstrate inside a living organism was studied with some in vitro experiments. These experiments do not give an exact behavior profile but the results can be evaluated to estimate what they can cause after they are injected into the bloodstream of a living organism.

Firstly their sizes were monitored with DLS measurements in presence and absence of GSH which is expected to cleave the covalent bonds between lipoic acid moieties leading to nanoparticle swelling and faster release. DLS measurements performed before and right after addition of GSH showed that CPN size increases immediately and dramatically after GSH addition. The initial Z-average diameter of 57nm immediately jumped to 170nm and increased the polydispersity value out of the range where reliable measurements can be made. This finding indicates that crosslinks within CPN matrices are cleaved by thiol groups of GSH molecules, exposing free thiols on the pendant groups. These thiols are able to form weak hydrogen bonds with water molecules causing water to leak into the CPN matrices, disrupt their structure and cause them to swell to sizes larger than their original sizes.

A drug release experiment was designed to predict the rate of CPT release from the CPNs under physiological conditions. CPT loaded CPNs were prepared and loaded into dialysis tubes. These tubes were then immersed into PBS solutions buffered to the physiological pH

value of 7.4. One group was left to be dialyzed in PBS and GSH was added to the release medium of another group. GSH concentration was adjusted to be 10 mM in the whole medium since this is the physiological concentration of GSH in a lot of types of tumor cells. The release mediums were sampled at determined time intervals and the samples were analyzed by UV-Vis spectroscopy to determine the amount of CPT that is released. Samples were returned to the medium after measurements. The CNPs were expected to demonstrate a faster CPT release in the presence of GSH but shortly after addition of GSH into the mediums, CPN precipitates were observed inside the dialysis tubes and they showed a slightly slower release than PBS control groups as seen in the Figure 58. This can be attributed to swollen CPNs clumping together to form large aggregates trapping CPT molecules inside them.

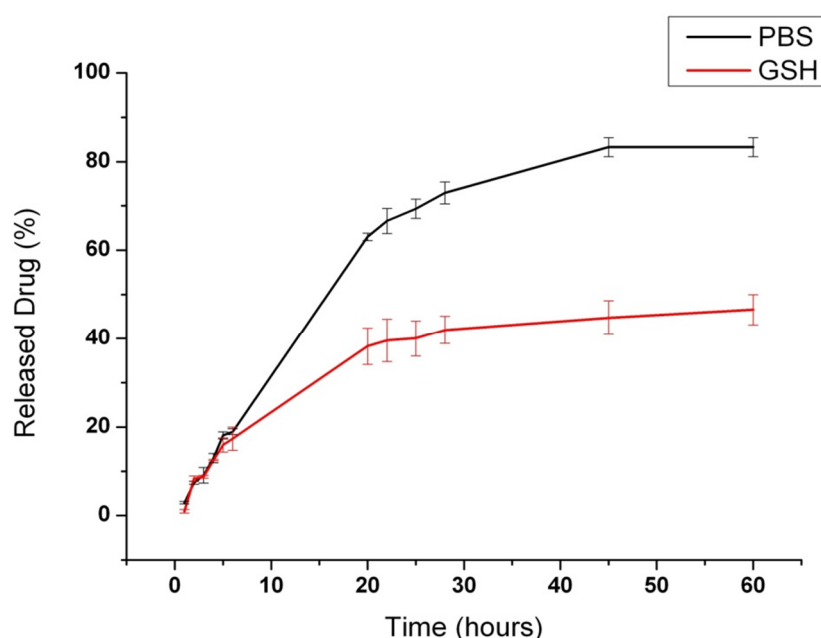


Figure 58: CPT release profile of PBT-LA nanoparticles in the absence and presence of GSH.

In order to see how CPNs interact with human cells, huh7 cells were incubated with blank and CPT loaded CPNs and investigated under fluorescence microscope. Cells were fixed with methanol and their nuclei were stained blue with Hoechst staining. Fluorescence microscopy studies showed that red emitting CPNs are visible under red filter of the equipment while no red signal is collected with the control cells as seen in Figure 59. As seen in the images, cells that are incubated with blank CPNs show blue stained intact nuclei with well-defined circular borders and red CPNs localized in the vicinity of nuclei. Cells incubated with CPT loaded

CPNs show deviation from natural appearance of huh7 cells and disrupted cell nuclei with no clear edges indicating disintegration of the nuclei as a result of apoptosis processes.

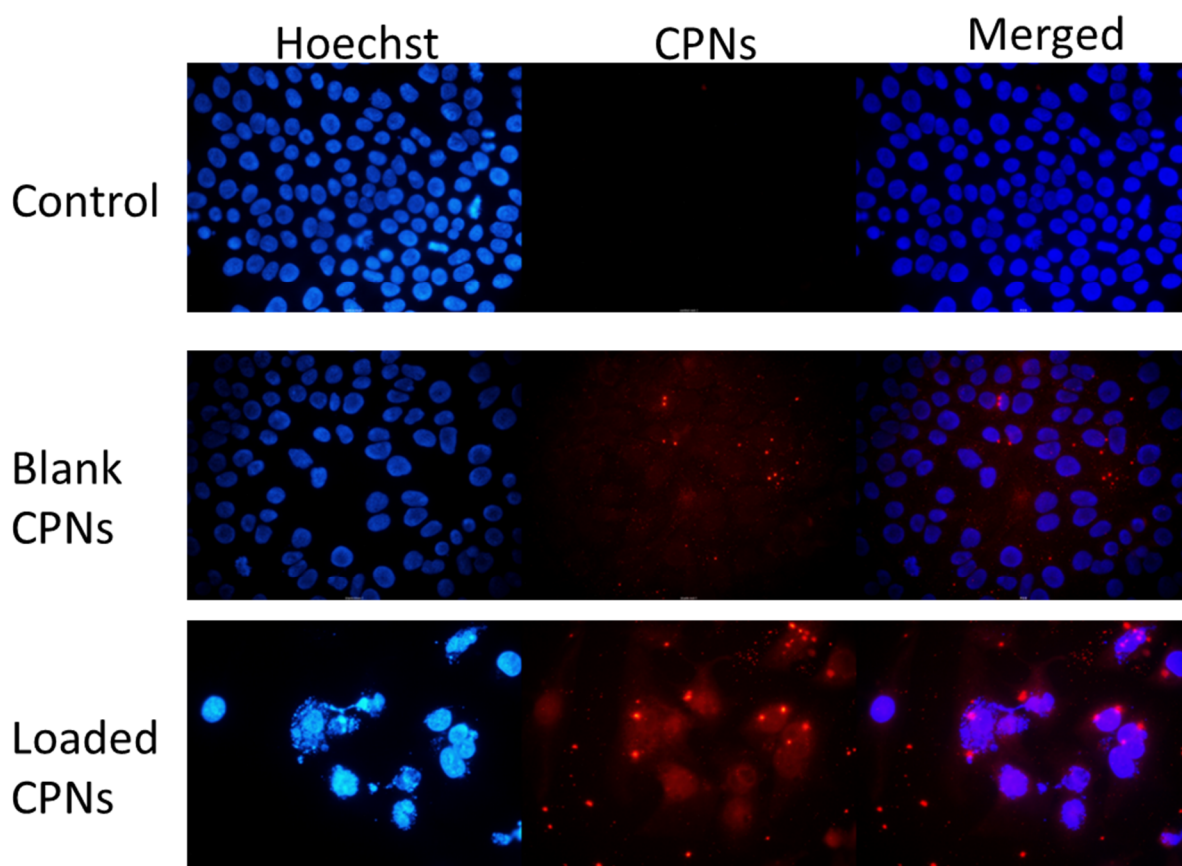


Figure 59: Fluorescence microscopy images of Huh7 cells incubated with blank and CPT loaded PBT-LA nanoparticles.

A real time electronic cell sensing assay was performed to monitor cytotoxicity of blank and CPT loaded CPNs.

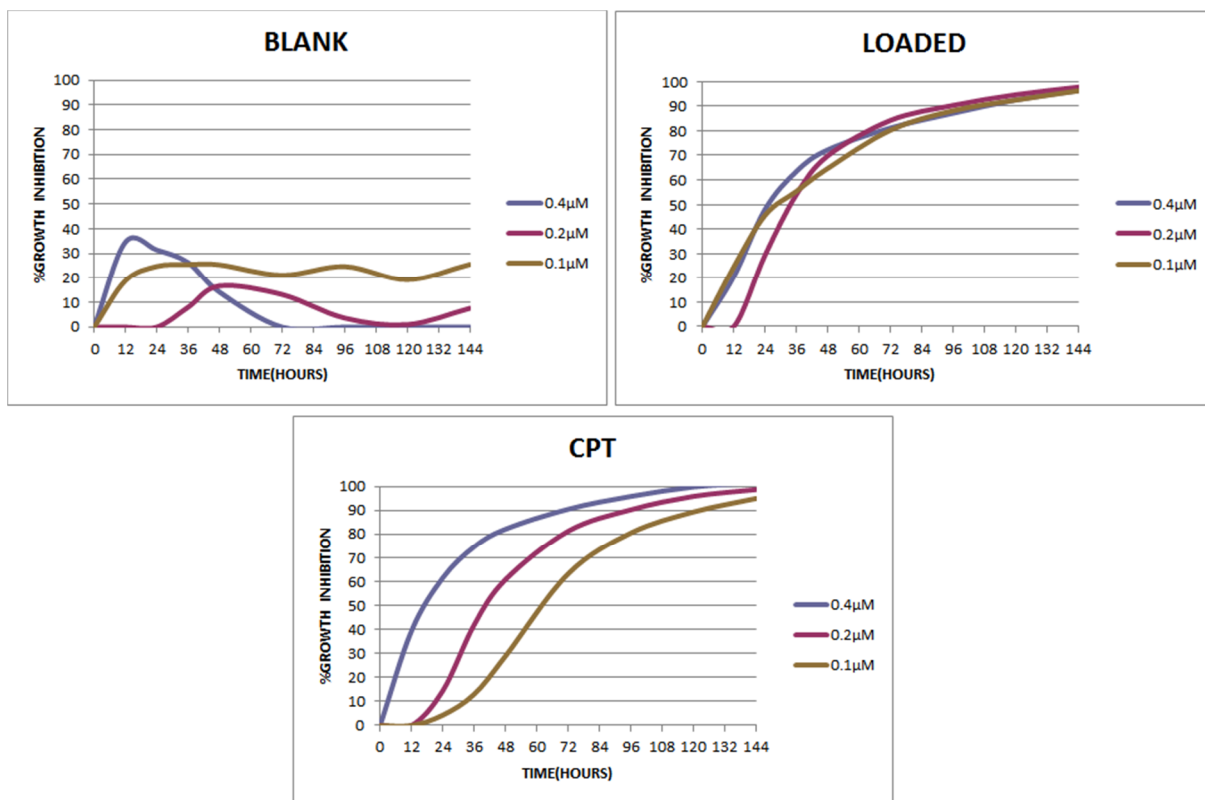


Figure 60: RT-Ces results of CPT loaded and blank PBF nanoparticles.

As can be seen in the Figure 60, blank CPNs show very limited and temporary cytotoxicity. This can be attributed to interaction of CPNs with random proteins inside the cells, disrupting their activity and inhibiting their growth. But cells can react to this situation and rapidly synthesize these proteins, gaining their original growth trend. Loaded CPNs on the other hand show a growth inhibition pattern that is very similar to free CPT but they show enhanced cytotoxicity at lower concentrations since CPT molecules carried by CPNs are internalized more efficiently by the cells compared to free CPT because of the poor solubility and aggregation of free CPT.

CHAPTER 3

CONCLUSION

In this thesis, three different stimuli responsive conjugated polymer nanoparticles were synthesized and characterized. Their suitability for being utilized as simple theranostic platforms was investigated through different experiments and in-vitro tests. Red and green emitting pH sensitive nanoparticles and red emitting redox sensitive nanoparticles were prepared and characterized. It was shown that spherical CPNs with tunable sizes and low polydispersities can be prepared. CPT loaded nanoparticles are prepared to assess their drug loading abilities and it was shown that conjugated polymers have high drug loading performances in terms of drug encapsulation efficiency and drug loading efficiency due to favorable weak interactions with CPT molecules. Release behavior of CPT from these nanoparticles was studied in the presence and absence of stimuli. It was shown that both pH sensitive CPNs show faster drug release in-vitro in acidic environment as expected. Redox sensitive CPNs on the other hand show heavy aggregation in presence of GSH molecules in vitro which causes them to release CPT slower since they sit in a stationary membrane. This effect is thought to be eliminated in an in vivo context due to heavy dilution after injection into blood stream.

All CPNs showed very mild cytotoxicity when they are not loaded with CPT as expected. Temporary cell growth inhibition they cause is attributed to their random interference with cytosol proteins. CPT loaded CPNs showed cytotoxicity according to their drug loading rates in pH sensitive CPNs. CPT loaded CPNs started their bioactivity later than free CPT as expected due to delayed release but higher loading rates caused a longer delay due to aggregation of drug molecules. Redox sensitive CPNs on the other hand showed a cytotoxicity profile similar to free CPT probably due to fast diffusion in low drug loading rates. All CPNs are internalized into Huh7 cells and are visible with a fluorescence microscope.

These findings suggest that CPNs can be used as stimuli-responsive theranostic platforms without using an extra imaging agent added to the system as the drug carrier matrix also acts as a photostable fluorescent probe. They can also passively target tumor sites due to their sensitivity to acidity of tumor microenvironments or elevated redox potential of cancer cells.

CHAPTER 4

EXPERIMENTAL DETAILS

All reagents were purchased from Sigma Aldrich Chemical Co. and were used as received. Column chromatography with silica gel (Kieselgel 60, 0.063-0.200 mm) was used for the purification of monomers. Thin layer chromatography (TLC) was performed by using silica gel plates (Kieselgel 60 F254, 1mm) to identify the products and impurities and determine the purity of the desired products. For structural characterization, nuclear magnetic resonance (NMR, Bruker Avance III 400 MHz spectrometer) and fourier transform infrared spectroscopy (FT-IR, Bruker Tensor 27) were performed. CDCl₃-d₆ solvent was used for NMR measurements. For the FT-IR measurements, KBr pellets were prepared. The data were recorded at 25°C, in the spectral range of 4000-400 cm⁻¹, by accumulating 25 scans with a resolution of 4 cm⁻¹. For the optical characterization, a UV-Vis spectrophotometer (Cary Uv-Vis) and a fluorescence spectrophotometer (Cary Eclipse) equipped with a xenon lamp as the excitation source were used. Autoclaved ddH₂O was used to prepare the nanoparticles. The sizes of nanoparticles were measured by dynamic light scattering (DLS, Zetasizer Nano-ZS). Measurements were carried out at 633 nm and the laser, as a light source, was used at room temperature. The average particle diameters were calculated by the Marquardt method. The DLS measurements were usually repeated at least three times and the average values were reported. Morphological characterization was done by scanning electron microscopy (SEM, Quanta 200 FEG).

To quantify the amount of adsorbed proteins on the nanoparticles in the human blood serum environment Bradford reagent (Coomassie blue G-250) was used and the absorbance values of the samples were obtained through a spectrometry at 595 nm (Beckman-DU 640).

For Hoechst stained Huh7 cells for fluorescence microscopy images, Autoclaved cover slips were placed into 24-well plates and Huh7 human cancer cell lines were plated into these plates (9000cell/well). 24h later, growth medium of the cells were changed with fresh growth medium containing the corresponding compound. After 72h incubation period the cells were washed once with ice-cold 1xPBS. Then 100% ice-cold methanol was applied on the cells for 10min for fixation. Then ice-cold 1xPBS was used to remove the excess methanol. Finally, 1µg/ml Hoechst stain (dissolved in PBS) was applied to the cells and left for dark incubation 5min and de-stained with ddH₂O for 10 min. Cover slips were then mounted onto slides using glycerol and cells were observed under fluorescent microscope.

For RT-CES analysis, background noise was first eliminated by placing 50 μ l growth medium into 96X e-plate to get a steady impedance value. Then human liver cancer (Huh7) cells were grown (2000cells/well) for 24h. Cells were then treated with increasing concentrations (0.1-0.4 μ M) of the compounds. DMSO was used as negative control. Each experiment was performed in triplicate. The electronic readout (cell-sensor impedance) was displayed as an arbitrary unit called the cell index (CI). The CI value was obtained first every 10 min (fast-drug response) and then every 30 min (long-term drug response). The cell inhibition rate was calculated as (%) = (1 – CI treated cells/CIDMSO) *100.

4.1 Synthesis of 2-(2,5-dibromothiophen-3-yl)ethanol (M1)

To a two neck round- bottom flask was added 100 mL degassed ethyl acetate (EtOAc). To this flask NBS (10.41 g, 49.14 mmol) was subsequently be added and stirred for 20 minutes while the flask was opened to N₂ inlet. The flask was then covered with aluminum foil and added 2-(thiophen-3-yl)ethanol (3.00 g, 2.62 mL, 23.4 mmol). After addition of 3-thiophene-ethanol the reaction mixture was sonicated for 10 minutes and allowed it to be stirred at room temperature for overnight. The reaction mixture was first extracted with EtOAc/water, brine and then again with water and dried over Na₂SO₄. After running TLC (3:7; EtOAc:Cyclohexane), two spots were observed under UV-light. The solvent was evaporated under reduced pressure from the reaction mixture which provided yellow liquid. Product was purified by Si-gel column chromatography using cyclohexane as an eluent. Acetylated 2,5-dibromo thiophene monomer was isolated first and then 2,5-dibromo thiopheneethanol. (Yield: 60%)

¹H-NMR (400 MHz, CDCl₃, δ): 6.8 (s, 1 H), 3.8 (t, 2 H), 2.7 (t, 2 H) ; ¹³C-NMR (100MHz, CDCl₃, 25°C): δ 28.9, 62.9, 109.7, 110.9, 131.0, 138.3.

4.2 Synthesis of 2-(2,5-dibromothiophen-3-yl)ethyl acetate (M2):

A stirred solution of **M1** (1.00 g, 3.50 mmol) in 10 mL acetic anhydride was added pyridine (400 μ L, 5.24 mmol,) and the reaction mixture was allowed to stir at room temperature for overnight. After the reaction was over, the mixture was diluted with DCM; water was added and the extraction was carried out. Organic phase was collected and washed with water several times. The solvent was evaporated under reduced pressure which provided pale yellow liquid. This was further stirred with 20 mL MeOH for 20 minutes to convert the remaining acid-anhydride into methylester which was easily evaporated under reduced pressure. Product was purified by Si-gel column chromatography using cyclohexane as an eluent (1.04 g, 90%).

$^1\text{H-NMR}$ (400MHz, CDCl_3 , 25°C): δ 6.85 (s, 1H, c), 4.25 (t, $^3\text{J} = 6.4$ Hz, 2H, a), 2.82 (t, $^3\text{J} = 6.4$ Hz, 2H, b), 2.05 (s, 3H, d).; $^{13}\text{C-NMR}$ (100MHz, CDCl_3 , 25°C): δ 20.9, 28.9, 62.9, 109.7, 110.9, 131.0, 138.3, 170.7.

4.3 Synthesis of Poly [2-(2,5-dibromo-thiophen-3-yl)-ethyl acetate]-*co*-4,7-(2,1,3-Benzothiadiazole)] (PBT-(Ac))

2-(2,5-dibromo-thiophen-3-yl)-ethyl acetate (515.4 mg, 1.581 mmol) and 2,1,3-Benzothiadiazole-4,7-bis(boronic acid pinacol ester) (613.9 mg, 1.581 mmol) were placed into a 2 neck-RBF. The mixture was left under vacuum for 20 min. Degassed THF (20 ml) was added and stirred for 10 min. Then the aq. solution of K_2CO_3 (1500 mg, 7.905 mmol, 1.5 g) in 10 ml degassed water was added, catalytic amount of TBAB was added and the reaction was stirred for 10 minutes. Then the mixture was degassed via two cycles of freeze-pump-thaw and the flask was filled with N_2 gas. $\text{Pd}(\text{PPh}_3)_4$ (with a touch of spatula) was dissolved in 1 ml degassed water and added quickly. The mixture was heated to 80°C under N_2 gas 16 h. 20 mL degassed THF and 10 mL degassed toluene were added. The mixture was further stirred under argon. A purple colour solution was obtained. After about 66 h bromobenzene (100 μl) added and the reaction was further heated 4 h more. After the completion of the reaction, the solvents were evaporated under vacuum and extracted with DCM by washing with water several times. Organic solvent was removed and residue was suspended in cold methanol. The suspension was left overnight to settle down further. Precipitate was separated by decanting and re-dissolved in DCM to remove the undissolved particles. DCM was removed and the residue was washed with cold methanol, the flask was sonicated for 5-10 minutes to free the particles adhered on the flask wall. Then the Precipitate was filtered, washed with MeOH. The crude product was re-dissolved in THF and precipitated into cold MeOH for further purification. Purple coloured powder was collected and dried under vacuum for a few hours (525 mg, 46%).

$^1\text{H-NMR}$ (400MHz, CDCl_3 , 25°C): δ : 2.05 (m, 3H), 3.15 (m, 2H), 4.4 (m, 2H), 7.1 (m, 1H), 7.9-8.2 (m, 2H); $^{13}\text{C-NMR}$ (100MHz, CDCl_3 , 25°C): δ 21.0, 29.1, 29.9, 64.2, 125.2, 125.6, 130.1, 130.4, 152.3, 152.6, 170.9.

GPC: $M_n = 2.5 \times 10^4$ g mol $^{-1}$, $M_w = 5.2 \times 10^4$ g mol $^{-1}$ (THF as a solvent and polystyrene as standard).

4.4 Synthesis of poly{3-[9-(3-tert-Butoxycarbonylamino-propyl)-3-methyl-6-(7-methyl-4,7-dihydro-benzo[1,2,5]thiadiazol-4-yl)-9H-fluoren-9-yl]-propyl}-carbamic acid tert-butyl ester (PBF)

The compound M3 (800 mg, 1.25 mmol) and 2,1,3-Benzothiadiazole-4,7-bis(boronic acid pinocol ester) (490 mg, 1.25 mmol) were dried under vacuum then dissolved in DMF (20 ml). Then, the catalyst, tetrakis(triphenylphosphine) palladium [Pd(PPh₃)₄] was added quickly. The reaction mixture was stirred for 20 h at 80°C. For the work up, reaction mixture was poured to methanol. The solid residue was dissolved in THF and again poured to methanol for three times. In the last cycle, methanol was removed under reduced pressure to remove boronic ester residues. Yield: 760 mg, 78 %.

¹H-NMR (400 MHz, CDCl₃):δ 8.04 (m, 8 H, Ar H), 4.67 (t, 2 H, NH), 2.91 (m, 4 H, -CH₂), 2.34 (m, 4 H, -CH₂), 1.42 (s, 18 H, CH₃), 1.13 (t, 4 H, CH₂).

GPC: M_n= 19 977 g mol⁻¹, M_w= 21 676 g mol⁻¹ (THF as a solvent and polystyrene as standard).

4.5 Synthesis of (R)-2-(2-(benzo[c][1,2,5]thiadiazol-4-yl)thiophen-3-yl)ethyl 5-(1,2-dithiolan-3-yl)pentanoate (PBT-LA)

PBT-(Ac) (36 mg, 0.10 mmol) was dissolved in 20 ml DMF. NaOH (80 mg, 0.20 mmol) was dissolved in 5 ml water and this solution was added into the polymer solution. The mixture was stirred at room temperature overnight and the solvent was evaporated under reduced pressure. Resulting solid was washed with water several times dissolved in 20 ml DMF. mmol 1-Ethyl-3-(3-dimethylaminopropyl)carbodiimide (EDC) (39.4 mg, 0.20 mmol) was added to the solution and the mixture was stirred for 30 minutes. 4-Dimethylaminopyridine (DMAP) (8.4 mg, 6.0 x10⁻³ mmol) was added and stirred for 10 minutes. Finally, lipoic acid (34 mg, 0.16 mmol) was added and the mixture was left to be stirred at room temperature for 48 hours. After all the solvent was evaporated, resulting solid was washed with water twice and dried under vacuum. (Yield: 99 %)

¹H-NMR (400 MHz, CDCl₃):δ 8.0 (m, 3 H), 4.5 (t, 2 H), 3.5 (m, 1 H), 3.2 (m, 4 H), 2.7 (m, 2 H).

4.6 Preparation of Nanoparticles

In a typical procedure, 1 mg polymer was dissolved in dry THF (1 ml). The solution was sonicated for ~15 min and then injected rapidly to 20 ml of DD water. The sonication was continued for a further 30 min. THF was removed from the solution under reduced pressure. In preparation procedure of PBT-LA nanoparticles, 3 mg pluronic f-127 was dissolved in water prior to injection. 34.2 ug DTT from a stock solution was added onto nanoparticles after the sonication and stirred for 10 minutes. For the preparation of CPT loaded nanoparticles, the CPT amount in the correct ratio to polymer amount was taken from a concentrated stock solution in THF and added onto polymer solutions. Resulting CPN dispersions were loaded into dialysis tubes with 12000 mwco values and immersed into 0.02vol% tween20 solutions. Tween20 solutions were stirred overnight and 2ml samples were analyzed with UV-Vis absorbance measurements to measure the absorbance of free CPT at 368 nm. CPT dispersions in tween20 solutions with known concentrations are used to create an absorbance-concentration calibration curve. This curve was used to calculate the exact amount of free CPT inside tween20 solutions and calculate drug loading and encapsulation efficiencies.

4.7 Drug Release Studies

PBS containing 0.2 % Tween 20 was used as a release medium to improve the drug solubility. For drug release study in acidic environment acetate buffer (pH=5) was used. For drug release study in concentrated GSH environment 10mM GSH solution in PBS was used as release medium. After the dialysis to remove the unloded CPT from the dispersion of drug loaded CPNs was concentrated to 5mL. Then it was mixed with 5 mL of release medium and transferred in to a cellulose tubular membrane with molecular weight cut-off 12 kDa. The dialysis tube was placed into a beaker containing 100 ml of release medium and 0.2 wt% Tween 20 and shaken at 60 RPM, 37 °C in an incubator. 2ml of aliquot was withdrawn from the dialysate at different time intervals during the experiment and at each time equal amount of fresh PBS was added to the dialysate beaker to prevent the sink condition. The concentration of CPT in the release medium was measured by using UV-Vis measurements.

REFERENCES

1. Ki Young Choi, Gang Liu, Seulki Lee and Xiaoyuan Chen; RSC Nanoscale, **2012**,4,330
2. Reineke, Sneha S. Kelkar and Theresa M; Bioconjugated Chemistry, **2011**, pp. 1879–1903.
3. Jin Xie, Seulki Lee, and Xiaoyuan Chen; **2010**, Adv Drug Deliv Rev, pp. 1064–1079.
4. M. Ferrari; **2005**, Nat Rev Cancer, pp. 161-171.
5. Greish Khaled; Cancer Nanotechnology, **2010**, pp. 253-267
6. Stark Wendelin; Angew. Chem. **2011**, 6, 1242
7. Juliana M. Chan, Pedro M. Valencia, Liangfang Zhang, Robert Langer, Omid C. Farokhzad; **2010**, Cancer Nanotechnology Methods in Molecular Biology, pp. 163-175.
8. Xu Peisheng, et al., Angewandte Chemie, International Edition, **2007**, pp. 4999-5002.
9. Shi Meng, et al.; dvanced Functional Materials. **2009**, pp. 1689-1696.
10. Furgeson Darin Y., Dreher Matthew R. and Chilkoti Ashutosh; Journal of Controlled Release, **2006**, pp. 362-369 .
11. John Frangioni; Current Opinion in Chemical Biology, **2003**, pp. 626–634.
12. Ballou B, Ernst LA, Waggoner AS.; Current Medicinal Chemistry, **2005**, pp. 795–805.
13. Cai WB, Shin DW, Chen K, Gheysens O, Cao QZ, Wang SX, et al.; Nano Letters, **2006**, pp 669–676
14. Nuria Sanvicens, M. Pilar Marco. **2008**, pp 425-433
15. Jesse Jokerst, Tatsiana Lobovkina, Richard Zare, Sanjiv Gambhir. **2011**, Nanomedicine, pp. 715–728.
16. Dana Maria Copolovici, Kent Langel, Elo Eriste, Ülo Langel.; **2014**, ACS Nano, pp. 1972–1994.
17. Cheng Z, Al Zaki , Hui JZ, Muzykantov VR, Tsourkas A.; **2012**, Science, pp. 903-910.
18. Golam Kibriaa, Hiroto Hatakeyama, Noritaka Ohga, Kyoko Hida, Hideyoshi Harashima.; **2013**, Biomaterials, pp. 5617–5627
19. Nicolas Bertrand, Jun Wu, Xiaoyang Xu, Nazila Kamaly, Omid C. Farokhzad.; Advanced Drug Delivery Reviews. **2013**, pp. 2-25
20. G. Martin, K. Jain R.. Cancer Research, **1994**, 54, 1570

21. E. Lee, K. Na, Y. Bae.; J Control Release. **2003**, pp. 103–113.
22. Y. Bae, W. Jang, N. Nishiyama, S. Fukushima, K. Kataoka.; Mol Biosyst. **2005**, pp. 242-250
23. Y. Bae, S. Fukushima, A. Harada, K. Kataoka. Angew Chem Int Ed Engl. **2003**, pp. 4640–4643
24. Y. Bae, N. Nishiyama, S. Fukushima, H. Koyama, Y. Matsumura, K. Kataoka.; Bioconjugate Chem. **2005**, pp 122–130.
25. E. Lee, H. Shin, K. Na, Y. Bae; J Control Release. **2003**, pp. 363-374.
26. E. Lee, H. Shin, K. Na, Y. Bae; J Control Release. **2003**, pp. 363-374.
27. S. Solomatin, T. Bronich, A. Eisenberg, V. Kabanov, A. Kabanov; Langmuir. **2003**, pp. 8069–8076.
28. AS Hoffman, PS Stayton, O Press, N Murthy, et al. ;**2002**, pp. 992-999.
29. SI Kang, YH Bae.; Macromolecules. **2001**, pp. 8173-8178.
30. T Traitel, R Goldbart, J Kost. ; Journal of Biomaterial Sciences, Polymer Edition. **2008**, pp. 755-767.
31. El-Sayed, Stephanie J. Grainger and Mohamed E. H. Biologically Responsive Hybrid Biomaterials.,**2007**, pp. 171-190.
32. Estrela JM, Ortega A, Obrador E. Crit Rev Clin Lab Sci. **2006.**, pp. 143-181.
33. Angel L. Ortega, Salvador Mena and Jose M. Estrela. cancers. **2011**, pp. 1285-1310.
34. Ahn Na Koo, Hong Jae Lee, Sung Eun Kim, Jeong Ho Chang, Chiyong Park, Chulhee Kim, Jae Hyung Park and Sang Cheon Lee. ; Chem. Commun. **2008**, pp. 6570-6572.
35. Neil Grant, Hong Wu, and Haifei Zhang. ;Ind. Eng. Chem. Res. **2014**, pp 246–252
36. Remant Bahadur K.C., Varun Chandrashekar, Bei Cheng, Hexin Chen, Maria Marjorette O. Pena, Jiajia Zhang, Janis Montgomery and Peisheng Xu. Molecular Pharmaceutics. **2014**, pp 1897–1905
37. Rongran Wei, Liang Cheng , Meng Zheng , Ru Cheng , Fenghua Meng , Chao Deng , and Zhiyuan Zhong. Biomacromolecules. **2012**, pp 2429–2438
38. Shothem, T. A., et al., et al. Handbook of Conducting Polymers'. New York ,**1998**.
39. Sallaneck, W.R., Friend, R.H. and Bredas, J.L. **1999**, Physics Reports, pp. 231-251.
40. Bredas, J. L. and Silbey, R. Conjugated Polymers: The Novel Science and Technology of Highly Conducting and Nonlinear Optically Active Materials. Dordrecht : Kluwer Academic Publishers, **1991**.

41. Donus Tuncel and Hilmi V. Demir.; **2010**, *Nanoscale*, pp. 484–494.
42. Stephanie Schubert, Joseph T. Delaney, Jr and Ulrich S. Schubert. **2011**, *Soft Matter*, pp. 1581-1588.
43. Audrey Minost, Jean Delaveau, Marie-Alexandrine Bolzinger, Hatem Fessi and Abdelhamid Elaissari. **2012**, *Recent Patents on Drug Delivery & Formulation*, pp. 250-258.
44. K., Landfester. **2009**, *Angew Chem Int Ed Engl.*, pp. 4488–4507.
45. Ö. Gezici, a İ. Durmaz, Bilget Güven, Ö.Ünal, . Özgün, R. Cetin-Atalay and D. Tuncel. **2014**, *RSC Advances*, pp. 1302-1309.
46. Liheng Feng, Chunlei Zhu, Huanxiang Yuan, Libing Liu, Fengting Lv and Shu Wang. **2003**, *Chem. Soc. Rev.*, pp. 6620-6633.
47. Marites P. Melancon, R. Jason Stafford and Chun Li. **2012**, *J Control Release*, pp. 177–182.
48. M. Green, P. Howes, C. Berry, O. Argyros, M. Thanou. **2009**, *Proc. R.Soc.*, pp. 2751-2759.
49. Mechanism of Cellular Uptake of Highly Fluorescent Conjugated Polymer Nanoparticles. Lawrence P. Fernando, Prakash K. Kandel, Jiangbo Yu, Jason McNeill, P. Christine Ackroyd, and Kenneth A. Christensen. **2010**, *Biomacromolecules*, pp. 2675–2682.
50. Kai Li, Jie Pan, Si-Shen Feng, Arthur Wenqing Wu, Kan-Yi Pu, Yutao Liu and Bin Liu. **2009**, *Advanced Functional Materials*, pp. 3535–3542.
51. Ji-Cheng Yu, Yu-Lei Chen, Yu-Qi Zhang, Xi-Kuang Yao, Cheng-Gen Qian, Jun Huang, Sha Zhu, Xi-Qun Jiang, Qun-Dong Shen and Zhen Gu. **2014**, *Chem. Commun*, pp. 4699-4702.
52. Thomas S. Corbitt, Liping Ding, Eunkyung Ji, Linnea K. Ista, Katsu Ogawa, Gabriel P. Lopez,. **2009**, *Photochemical & Photobiological Sciences*, pp. 998-1005.
53. Solly K, Wang X, Xu X, Strulovici B, Zheng W. **2004**, *Assay Drug Dev Technol.* , pp. 363-372.
54. Estrela JM, Ortega A, Obrador E.; *Crit Rev Clin Lab Sci.* **2006**, , pp. 143-181.